UNIVERSITY OF BIRMINGHAM

Plastic deformation of Ti-6Al-4V micro-pillars at room temperature

By

Zhaoran Liu

A thesis submitted to the University of Birmingham

for the degree of

Doctor of philosophy

School of Metallurgy and Materials

University of Birmingham

March 2017

Abstract

In this work, the deformation behaviour of Ti-6Al-4V micro-pillars was studied systematically via compression tests at room temperature and detailed dislocation analyses using transmission electron microscopes (TEM). Micro-pillars with the diameters ranging from 0.5 μm to 5 μm were prepared using the focused ion beam (FIB). These pillars contain either the single α phase or both α and β phases. The pillars were prepared such that the compression loading directions are along either $[1\bar{1}00]$ or [0001] in order to activate either <***a***> or <***c+a***> slips.

The sample size effect on the yield strength has been observed in all groups of micro-pillars. When compressed along $[1\bar{1}00]$, the critical resolved shear stress (CRSS) of ***a*** prismatic slip measured from the single α phase micro-pillars increases from 336 MPa to 487 MPa as the pillar diameter decreases from 5 μm to 0.5 μm. The result can be fitted using the power law relationship with the exponent n = 0.61. When compressed along [0001], the CRSS of the <***c+a***> slip measured from the single α phase micro-pillars increases from 1036 MPa to 1147 MPa as the pillar diameter decreases from 5 μm to 0.5 μm. The exponent $n = 0.12$ for the power law relationship could be identified. The stress-strain curves recorded from the single α phase pillars tend to have more obvious serrations than the two-phase pillars.

The micro-pillars containing both α and β phases have lower yield stresses than their counterparts containing α single phase. Furthermore, the larger the volume fraction of the β phase in the pillar, the lower the yield stress. The two-phase micro-pillars show a stronger sample size effect on the yield strength with the power law exponent 0.50 when compressed along [0001] and 0.11 when compressed along

[$1\bar{1}00$]. The serration on the stress-strain curves observed in the α single phase pillars seems suppressed in the two-phase micro-pillars.

TEM analysis shows that in all micro-pillars compressed along [$1\bar{1}00$], regardless of the existence of the α/β interface, the $\boldsymbol{a}_1$ prismatic slip is the dominant slip system. In micro-pillars compressed along [0001], both 1st order and 2nd order pyramidal <***c+a***> slip systems can be observed after 2% strain. However only 2nd order pyramidal <***c+a***> slip can be identified at the edge of the heavily deformed area when compressed to 7% strain. The dislocation densities were measured at different strain level and dislocation interaction the α/β interface were investigated vis-a-vis the observation obtained from the micro-mechanical tests in the SEM.

Combining the micro-mechanical tests results and STEM analysis, the influence of β phase and the α/β interfaces on the strength of micro-scale samples are demonstrated. The β phase is proved weaker than the α phase and the α/β interfaces behaviour as both the barriers and sources of dislocations. The magnitude of influence depending on the volume fraction, orientation and morphology of the β phase and the α/β interfaces. The work-hardening rate is related to the orientation of micro-pillars and the α/β interfaces in the micro-pillars. The strain bursts can be suppressed by the α/β interface and smaller sample size. The sample with smaller size expressed the larger strain burst in the stress-strain curves. The orientation influences the number and magnitude of strain bursts.

Keywords: Titanium alloy; Micro-pillar compression; Interface; Size effect; Critical resolved shear stress

Preface

The work described in this thesis was carried out by the author in the School of Metallurgy and Materials, at The University of Birmingham, from September 2012 to March 2017, under the supervision of Dr Y.L. Chiu and Prof I.P. Jones.

The material presented here is original and no part of this work has been submitted for a degree at this or any other university. Where the work of others has been drawn upon, it is acknowledged in the text.

Papers based on part of the present work are in preparation for publication.

Acknowledgement

I would like to express my deepest gratitude and appreciation to Dr Y.L. Chiu and Prof I.P. Jones for their patient supervision, guidance, encouragement, and help. Dr Y.L. Chiu is not only a responsible supervisor on my academic research and a reliable friend in the daily life but also a mentor teaching me how to be a better man. Prof. I.P. Jones gave me many useful suggestions especially at my beginning of my project.

Many thanks to Dr S. Yan for allowing me using the FIB and TEM at The University of Loughborough. Her help is vital to finishing my experiments.

Thanks for all technical staff in the EM center at The University of Birmingham. Thanks to Dr R. Ding for his advice and help with the FIB/TEM work.

I am appreciative of my nice colleagues in the School of Metallurgy and Materials.

Finally, I would like to thank my family, my parents Xisheng Liu and Li Li, my wife Zhiying Shao. They did whatever they could with their deepest love to support me to finish my PhD study abroad.

To whoever supported me during my PhD study.

Table of Contents

Chapter 1 Introduction

From a certain perspective, the human is pushing the boundaries of science in two opposite directions, extremely huge or extremely tiny. In the theories of classical mechanics, the mechanical properties of materials are independent of sample dimensions. However, experimental and simulation results in the past decades indicate that the mechanical properties of crystal perform differently when sample dimensions reduce to the micron scale, which is known as the sample size effect [1, 2]. In the aspect of strength, the sample size effect observed is aligned with "smaller is stronger" [3].

Generally, in-situ electron microscopy has become a popular method for the sample size effect investigation as it offers the opportunity to study the response of the material to stimuli in real time. It is essential to understand the mechanical behaviour of materials for small-scale applications such as micro-electro-mechanical-system (MEMS) or nano-electro-mechanical-system (NEMS) which are widely used as sensors or actuators (e.g. shown in Figure 1-1) [4]. Aerospace applications are another field which requires the knowledge of micro-scale deformation [5].

Titanium alloys are not only used in aero-engines, they also have the potential to be used at micro-scale [6]. Although titanium alloys have some disadvantages in industrial production compared with the silicon which is mostly used in the MEMS,

their high mechanical performance and good biocompatibility make them a good choice in some circumstances, such as medical applications.

There are many methods of investigating the sample size effect on strength such as uniaxial micro-tensile test, micro-cantilevers bending test or uniaxial micro-pillars compression test, as shown in Figure 1-2 [7]. Uchic and Dimiduk [8] developed the widely used methodology of investigating the crystal plasticity of Ni micro-pillar samples via micro-compression test. Micro-pillars of different diameters can be fabricated using a focused ion beam (FIB) and deformed using a nano-indenter or other similar sensitive mechanical test machines with a flat-ended probe.

Ti-6Al-4V, the most widely used titanium alloys, has been extensively studied at the macroscopic scale. However, there is not enough research at the micro-scale.

The thesis will focus on the study of Ti-6Al-4V micro-pillars and mainly answer the questions in the following questions:

1) What is the relation between the yield strength and the diameter of Ti-6Al-4V micro-pillar?
2) How does the Ti-6Al-4V crystal orientation affect the yield strength at the micro-scale?
3) How does the α/β interface affect the sample size effect on the strength in Ti-6Al-4V micro-pillars?
4) What are the reasons for the observed sample size effect in Ti-6Al-4V micro-pillars?

The thesis lays out in the following chapters:

Chapter 2 gives a brief introduction on Ti-6Al-4V and Chapter 3 is the literature review on the sample size effect on strength of crystalline materials during plastic deformation. Chapter 4 contains the material preparation, experiment process, and techniques used in the study. Chapter 5 contains the sample size effect on strength obtained and SEM images of the micro-pillars before and after the compression tests. Chapter 6 contains the detailed dislocation analysis obtained from these deformed micro-pillars using STEM. Chapter 7 is the discussion of the mechanical test results and TEM analysis. Conclusions and future work are in Chapter 8.

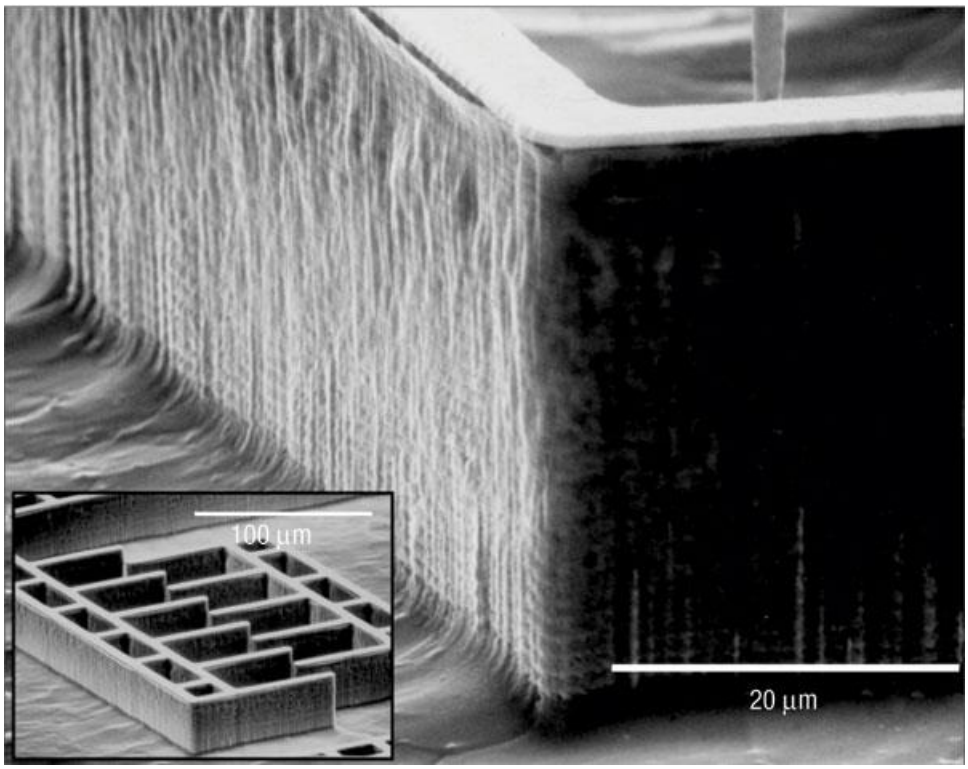

Figure 1-1 Titanium comb drive actuator in SEM [9]

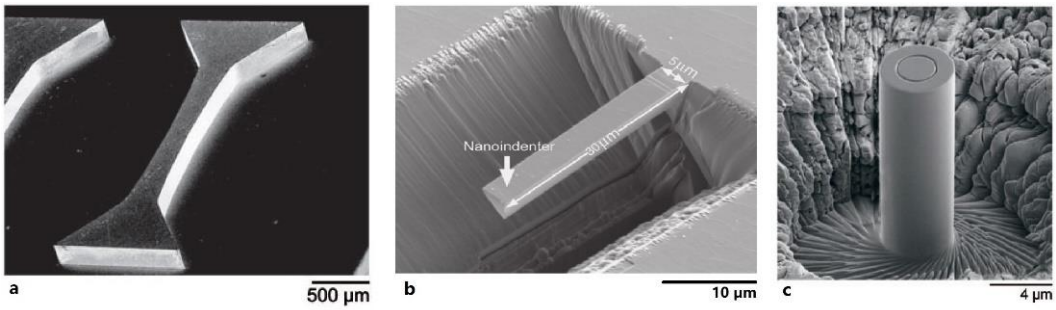

Figure 1-2 SEM images of (a) a micro-tensile sample, (b) a micro-cantilever and (c) a micro-pillar [7, 10, 11]

Chapter 2 Titanium alloy

In chapter 2, the crystal structures, microstructure and slip systems of titanium and α+β titanium alloys are introduced. For a better understanding of the role of interface in the following chapters, the structure of the α/β interface in titanium alloy is explained.

2.1 Introduction to titanium and its alloy

Ti-6Al-4V (wt. %), significantly stronger than commercially pure titanium, is the most commonly used titanium alloy [12]. It has a good combination of specific strength (strength/density ratio), toughness, ductility, fatigue strength and stability at temperatures up to 400°C. It not only has outstanding mechanical properties but also has excellent biocompatibility, which makes this alloy widely used in both aero-industrial and biomedical applications [13]. Micro-electro-mechanical-systems (MEMS) represent a broad class of devices whose defining characteristics are their micrometre-scale size and electro-mechanical functionality. They are used in many micro-sensors or actuators. Their utility arises largely due to their small dimensions, which enable exceptional sensitivity for sensing and high precision movement for actuation [4]. Recent developments have allowed for the realization of bulk titanium MEMS for devices that require higher fracture toughness and/or resistance to harsh environments [14]. Titanium alloys are attractive as the structural materials in MEMS, which will usually experience plastic deformation. The experimented data for macro-scale materials are not appropriate for the design

of micro-scale components because there is the sample size effect. Therefore, it is necessary to study the performance of titanium alloys at the micro-scales.

2.2 Crystal structure and microstructure of Ti-6Al-4V

Titanium has two allotropic structures: α, which has a hexagonal close-packed (h.c.p.) structure and β with a body-centered cubic (b.c.c.) structure [15]. The crystal structures of α phase and β phase are shown in Figure 2-1. The h.c.p. crystal structured α phase, at the room temperature, has the lattice parameters of a = 0.295 nm and c = 0.468 nm, the three most densely packed planes are the (0002) plane (the basal plane); the three $\{10\bar{1}0\}$ planes (the prismatic planes) and the six $\{10\bar{1}1\}$ planes (the pyramidal planes). The three $<11\bar{2}0>$ direction (the $\boldsymbol{a}_1$, $\boldsymbol{a}_2$, and $\boldsymbol{a}_3$ axes) are the close-packed directions. The β phase with b.c.c. crystal structure has six most densely packed {110} planes and the lattice parameter a = 0.332 nm at 900 °C. The most closely packed directions are <111> directions [16].

Elements that when dissolved in titanium increase its α-β transformation temperature (the β-transus temperature) with increasing solute content are known as α stabilizers. α stabilizers are often simple metals (e.g. Al) or interstitial elements (e.g. O, N, and C). Alloying elements that decrease the β-transus temperature are referred to as β stabilizers and they are generally the transition metals (e.g. V and Mo) and noble metals [17]. Based on the relative amounts of the α and β phases, titanium alloys are generally classified as α alloy, β alloy and α+β alloy [18], as shown schematically in the phase diagram in Figure 2-2.

Ti-6Al-4V is classified as an α+β titanium alloy. The mechanical properties of titanium alloys usually depend on their microstructures developed during the thermo-mechanical processing. Generally speaking, three types of microstructures can be commonly obtained in α+β alloys: fully lamellar, bi-modal (duplex) and fully equiaxed, as illustrated in Figure 2-3. These microstructures can be achieved via the control of four different steps of thermo-mechanical processing: homogenization in the β phase field (I), deformation in the α+β phase field (II), recrystallization (III), and the final ageing and/or stress relieving treatment (IV). The difference in the processing route for these microstructures is mainly produced in step III. The fully lamellar microstructure consists of fine α and β phase lamellae and is often obtained by in step III an annealing treatment in the β phase field, which is usually kept within 30-50 °C above the β-transus temperature (1000 ± 20 °C for Ti-6Al-4V) to control the β grain size. The bi-modal microstructure contains equiaxed primary α (α_p) in a lamellar α+β matrix and it is formed in recrystallization in the α+β phase field. If the cooling rate from the bi-modal recrystallization annealing temperature is sufficiently low, only equiaxed α_p grains will grow during the cooling process and no α lamellae are formed within the β grains. This is one possible way to obtain the equiaxed microstructure [16, 19].

The microstructural features in an α+β titanium alloy depend on the cooling rate, because of the characteristic features of the lamellar microstructure, such as the size of the α lamellae (α plates), the α colony size, and the thickness of α layers at β grain boundaries all decrease with increasing cooling rate [16]. As shown in Figure 2-2, when a titanium alloy is cooled down across the β-transus temperature [20], a β to α phase transformation will occur. When the titanium alloy is heat-treated to

above the transus temperature and then cooled in air, a fine lamellar structure can be obtained in Figure 2-4 (a) shows. When the cooling rate is slower, such as cooling in furnace or vermiculite, the α and β lamellas will grow coarser as shown in Figure 2-4 (b). When a titanium alloy is rapidly cooled from the β region, the α' phase can be obtained from the β phase region by a martensitic reaction. For Ti-6Al-4V, the change from a colony type of microstructure to a martensitic structure needs the cooling rate higher than 1000 °C/min. Figure 2-4 (c) shows the α' phase: an acicular martensite [16, 21].

2.3 Slip systems and critical resolved shear stress in Ti-6Al-4V

At room temperature, the macroscopic plastic deformation of α+β titanium alloys often results from the dislocation slip in two phases [16]. Although twinning is another important deformation mode of CP titanium and some α titanium alloys, it is significantly suppressed in two-phase α+β titanium alloys by small phase dimensions, high solute content and the presence of precipitates [16].

The various slip directions and slip planes in α titanium are indicated in its hexagonal unit cell in Figure 2-5. There are <***a***> type slip systems, including three basal slip systems, three prismatic slip systems ($\{10\bar{1}0\}$ slip planes), and six 1st order pyramidal slip systems ($\{10\bar{1}1\}$ slip planes), and with Burgers vectors ⅓$<11\bar{2}0>$. In addition, <***c+a***> type slip systems with Burgers vectors ⅓$<11\bar{2}3>$ on $\{10\bar{1}1\}$ 1st order pyramidal and $\{11\bar{2}2\}$ 2nd order pyramidal slip planes have also been reported [22]. The typical slip planes in the b.c.c. structured β phase are {110}, {112}, and {123}, all with ½<111> type of Burgers vector [16, 23].

In response to an applied stress, the most favourably oriented slip system in a crystal will be activated when its critical resolved shear stress (CRSS) τ_{CRSS} is reached. CRSS represents the minimum shear stress required to initiate the dislocation slip, and is generally regarded as a material property [19]. $\tau_{CRSS} = \sigma m$, in which σ is the applied stress and *m* is termed Schmid factor. Schmid factor writes

$$m = cos\varphi cos\lambda \qquad \textit{(Equation 2-1)},$$

where φ is the angle between the loading direction and the slip direction, and λ is the angle between the loading direction and the normal direction of slip plane. It is apparent that the primary slip system activated will often be the system with the greatest Schmid factor for the same CRSS. However, Schmid factors are not always restrictive to predict activation of slip systems because of some factors such as local size or morphology of microstructure or neighbouring crystallographic texture et al. affect the activation of slip systems [22]. Jones and Hutchinson [24] systematically activated all the possible slip systems in the highly textured bulk Ti-6Al-4V sample. The values of CRSS are strongly dependent on the alloy content and on the test temperature. At room temperature, there are small differences in CRSS between <***a***> type slip systems, in a ranking sequence from low to high: $(10\bar{1}0)$ < $(10\bar{1}1)$ < (0001). The CRSS for <***c***+***a***> slip systems are much higher than that for the <***a***> type slip systems in single crystals Ti-6.6Al [16] and in polycrystalline Ti-6Al-4V as well [10, 25]. In the compression test [26], the <***a***> type prismatic slips can be activated most easily with the lowest CRSS of 392 MPa when compression along $[10\bar{1}0]$. Basal and pyramidal <***a***> slips were activated with higher CRSS as 444 MPa and 404MPa when compressed along $[10\bar{1}1]$. Pyramidal <***c***+***a***> slip systems

were difficult to activate with CRSS as high as 631 MPa for 1st order pyramidal planes $\{10\ \bar{1}1\}$ when compressed along [0001]. They have explained experimentally using TEM analysis and theoretically using finite element analysis (FEA) modelling that compression along [0001] direction tend to slip on $\{1\bar{1}01\}$ the 1st order pyramidal planes rather than $\{11\bar{2}2\}$ the 2nd order pyramidal planes in titanium and its alloys [26]. Later researches confirmed that <***c+a***> dislocation on the 1st order pyramidal planes were the main <***c+a***> slip systems in titanium alloys [10, 27, 28]. However, there were reports [29, 30] on the observation of $\{11\bar{2}2\}$ the 2nd order pyramidal planes in titanium and its alloys. This diversity will be analysed later in Chapter 6.

2.4 α/β interface in Ti-6Al-4V

In titanium alloys, the α/β interfaces observed at room temperature are formed after the β (b.c.c.) → α (h.c.p.) phase transformation. A schematic drawing of the structure and orientation of α/β interface is shown in Figure 2-6. Taking the α/β lamella microstructure as an example, the β phase filled the gaps between α lamellae. Crystallographically, the β matrix and the α lamellae assume the Burgers orientation relationship, i.e. $(0001)_\alpha // (101)_\beta$, $[2\bar{1}\bar{1}0]_\alpha // [11\bar{1}]_\beta$ [31]). In the literature, Burgers vectors in both phases that following this orientation relationship were defined customarily as $\boldsymbol{a}_1 = 1/3[2\bar{1}\bar{1}0]$, $\boldsymbol{a}_2 = 1/3[\bar{1}2\bar{1}0]$, $\boldsymbol{a}_3 = 1/3[\bar{1}\bar{1}20]$, $\boldsymbol{b}_1 = 1/2[11\bar{1}]$, $\boldsymbol{b}_2 = 1/2[\bar{1}11]$ [32]. The interfaces between α lamellae and β matrix consist of two sets of faces, namely the side face and the broad face [33]. These faces grow along two specific orientations: The side face usually lies parallel to the close-packed planes i.e. $(0001)_\alpha$ and $(110)_\beta$. The broad face is close to $(\bar{4}\ 15\ \bar{1}\bar{1}\ 0)_\alpha$ and $(\bar{1}\bar{1}\ 13\ 11)_\beta$,

which is an irrational habit plane containing structural ledges aligned along a preferential direction which is known as the lattice "invariant line" [34] close to $[\bar{7}250]_\alpha$ and $[\bar{3}\bar{5}3]_\beta$ [33, 35-37].

The orientation of relationship can be explained using the "invariant line" theory proposed by Dahmen [34]. In the aspect of crystallography, the lattice correspondence at the interface, resulted from the b.c.c. → h.c.p. phase transformation, can be described by a b.c.c. unit cell of the β phase deformed by a transformation strain into an h.c.p. unit cell of the α phase, as shown in Figure 2-7. The transformation strain can be expressed mathematically by a transformation matrix $\boldsymbol{A}$. According to the Burgers orientation relationship, a unique vector $\boldsymbol{u}$ on the close-packed plane of b.c.c. (101) plane may be rotated by an angle θ around the [101] and transformed into the vector $\boldsymbol{u'}$ which preserved the length of $|\boldsymbol{u}|$ in the close-packed plane of h.c.p. (0001) plane after the transformation. Usually length and angles will be distorted after such a transformation. If there is a rigid body rotation through an angle θ of the transformed h.c.p. crystal structure (described as a matrix $\boldsymbol{R}$), which makes the vector $\boldsymbol{u'}$ in the transformed h.c.p. crystal structure unrotated and unstretched compared with $\boldsymbol{u}$ in the b.c.c. crystal structure, this vector $\boldsymbol{u}$ will become a lattice invariant line. In this case, the invariant line is contained in both the transformed h.c.p. crystal structure and the parent b.c.c. crystal structure. Therefore, the α/β interfaces always contain the invariant line [38]. In Ti-6Al-4V, the lattice invariant line can be defined as shown in the appendix as the lattice $[\bar{3}\bar{5}3]_\beta$ // $[\bar{7}250]_\alpha$ by a rotation of 5.74° around the axis of $[0001]_\alpha$ // $[110]_\beta$.

The structure of the interface can be explained using the theory of coherency of interface [39-41]. Generally, an interface between two phases can be coherent, semi-coherent or incoherent. A coherent interface is defined as a boundary between two crystal structures where the mismatch in-between is accommodated completely by the elastic strain [41]. This is typically the case when there is a slight difference between the lattice parameters of two structures and the mismatch can be accommodated by the elastic strain along the interface. An incoherent interface is where two crystals are contacted rigidly and have no periodical structures [41]. If the mismatch between the lattice parameters of two structures is sufficiently large, such as across the broad face of the α and β phases in Ti-6Al-4V [13], the structural ledges/periodically distributed misfit dislocations along the interface may be formed, in addition to the elastic strain. If the ledges/misfit dislocations are separated sufficiently wide, the interface can be considered as semi-coherent [42]. In terms of Ti-6Al-4V, the structural ledges on the broad face reshuffle (resulting in large interface areas on low-energy planes and small areas on the connecting high-energy planes as shown in Figure 2-6) to minimize the total interface energy along the broad face [33]. High-resolution TEM analyses have confirmed that the broad face is semi-coherent containing structural ledges [33, 42] rather than the planar interface which is $(\bar{4}\ 15\ \overline{11}\ 0)_{\alpha}$ // $(\overline{11}\ 13\ 11)_{\beta}$ in Ti alloys [37]. The structural ledge model is schematically shown in Figure 2-6 (b) with the view perpendicular to the side face showing the detailed orientation relationship between α, β and the structural ledge. This orientation relationship between α and β phases will be used to guide the sample preparation and analysing slip systems involved in the subsequent plastic deformation.

2.5 The role of α/β interfaces in plastic deformation

The mechanisms of slip transmission across the interface in polycrystalline materials have been studied [43-47]. The slip activation criteria were found to be different at the macro-scale and at the local interfaces [43]. At the macro-scale, the slip system activation in a sample is usually determined by the Schmid factor [44]. However, at a local interface, there are other factors may have an effect on the activation and then slip transference [45]. During the plastic deformation, interfaces usually act as barriers to dislocation motion and cause dislocation pile-up and stress concentration. In other words, the plastic deformation often initiates on one side of the interface and with the subsequent work-hardening, the plastic flow starts on the other side of the interface [46]. Microscopically, the slip transference across the interface can be accomplished by one of the several different mechanisms, such as nucleation of new dislocations, direct transmission of dislocations or the absorption and desorption of dislocations into and out of the interface [47]. Generally, two geometric criteria for slip transference [44] should be met for easy slip transference: 1) The angle between the incoming slip plane and the outgoing slip plane should be the minimum (angle θ in Figure 2-8). 2) The angles between the two Burgers vectors should also be at the minimum (angle φ in Figure 2-8) [47].

In titanium alloys, the angle between the Burgers vectors in two phases are not always perfectly aligned and this plays an important role in the slip transmission across the interface. Mills et al. [25, 32, 48-51] have reported the influence of the α/β interface on different slip systems in the plastic deformation of bulk titanium alloys. Suri et al. [51] performed creep tests at the room temperature on α/β titanium

alloy Ti-5Al-2.5Sn-0.5Fe bulk samples extracted from different colonies and observed distinct <***a***> prismatic slip transmission behaviours in different colonies. In the colonies where $\boldsymbol{a}_1$ = 1/3 $[2\bar{1}\bar{1}0]$ prismatic slip was activated, the slip easily transferred from α phase to β phase as the corresponding slip system 1/2 $[11\bar{1}](\bar{1}21)$. In the colony where $\boldsymbol{a}_2$ = 1/3$[\bar{1}2\bar{1}0]$ prismatic slip was activated, edge dislocations piled up at the α/β interface, indicating a higher resistance to the slip transfer across the α/β interface. This anisotropy is believed to be the result of the misalignment of Burgers vectors in α and β phases. Savage et al. [25] performed further compression tests of a α/β titanium alloy along different orientations (using different colonies). Dislocations of $\boldsymbol{a}_1$, $\boldsymbol{a}_2$, $\boldsymbol{a}_3$ Burgers vectors on the basal plane were studied. It was found that the CRSS and strain hardening rates were different when different slip systems were activated. It was suggested that since there is the only 0.7° misorientation between $\boldsymbol{a_1}$ and $\boldsymbol{b_1}$ [32], $\boldsymbol{a}_1$ dislocations can transmit across the interface easily and therefore the lowest CRSS and strain hardening rate. As the misorientation between $\boldsymbol{a}_2$ and $\boldsymbol{b}_2$ increased to 11.1° [32], they noticed the increased amount of $\boldsymbol{b}_2$ dislocations piles-up in the β phase when slip transferred from β into α phase. When $\boldsymbol{a}_3$ on the basal plane was activated in α phase, large numbers of dislocations piled up within the α phase close to the α/β interface for there is no closely aligned Burgers vectors in the β phase for any possible slip transmission across the interface in this case. Mills et al. [32] observed that in Ti-5Al-2.5Sn-0.5Fe the three <***a***> type Burgers vectors always aligned at particular angles to the broad face of the β lath structure, as predicted by the invariant line construction. The angle between the $\boldsymbol{a}_1$ and the broad face is always observed to be a shallow angle, close to 15°. Similarly, the $\boldsymbol{a}_2$ and $\boldsymbol{a}_3$ directions typically form angles of 75°

and 45°. Ding et al. [52] confirmed that the same orientation relationship exists in Ti-6Al-4V, as shown in Figure 2-9.

Apart from the misorientation of Burgers vectors, the misorientation of slip plane is another factor can affect the slip transmission. Because of the Burgers orientation relationship $(0001)_\alpha // (101)_\beta$, $[2\bar{1}\bar{1}0]_\alpha // [11\bar{1}]_\beta$, $[0\bar{1}10]_\alpha // [\bar{1}21]_\beta$ between the α phase and the β phase [31] shown in Figure 2-6 (b), the basal slip plane {0001} for <***a***> type dislocations in α phase and the corresponding {101} planes slip planes in β phase are parallel. Therefore, misorientation between the prismatic slip plane $\{0\bar{1}10\}$ (perpendicular to the basal {0001} plane) for $\boldsymbol{a}_1$, $\boldsymbol{a}_2$, $\boldsymbol{a}_3$ dislocations in α phase and the corresponding $\{\bar{1}21\}$ slip planes in β phase (perpendicular to the basal {101} plane) are same as the misorientation of between corresponding Burgers vectors.

Compared with the well-studied <***a***> type slip systems transmission, few papers [10, 53] reported <***c***+***a***> slips transmission through interfaces as they are more difficult to be activated than <***a***> type slip systems in the bulk samples. However, <***c***+***a***> type slip systems are important when the loading direction is along the ***c***-axis in α phase. Ding et al. [10, 53] studied the interaction between <***c***+***a***> dislocations and the α/β interface in micro-scale specimens prepared using FIB. Three possible transmission modes for <***c***+***a***> slip systems were proposed: (1) direct transmission as the $\boldsymbol{a}_1$ prismatic slip mentioned earlier [25, 51]; (2) slip transmission with the generation of residual dislocations at the interface [51]; (3) indirect slip transmission, where the incoming dislocations cannot move across the α/β interface but new dislocations can be generated at the other side of the interface under the

increasing stress accumulation. Based on their TEM observation of bent Ti-6Al-4V micro-cantilevers [10], 4 out of 12 possible 1st order pyramidal <***c***+***a***> slip systems were predicted to be able to transfer across the α/β interface easily in a bent micro-cantilever as they were aligned with <111>$\{1\bar{1}0\}$ slip systems in β phase, but the transmission mode has not been determined because of the low quality of the specimens due to bending etc.

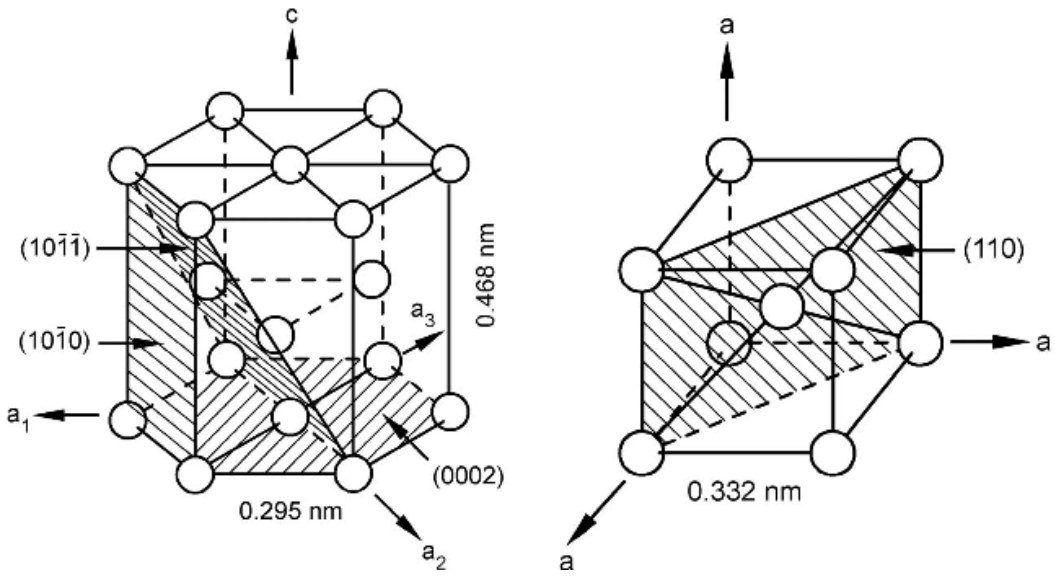

h.c.p *b.c.c*

Figure 2-1 Unit cells of the α phase (h.c.p) and β phase (b.c.c) titanium [16]

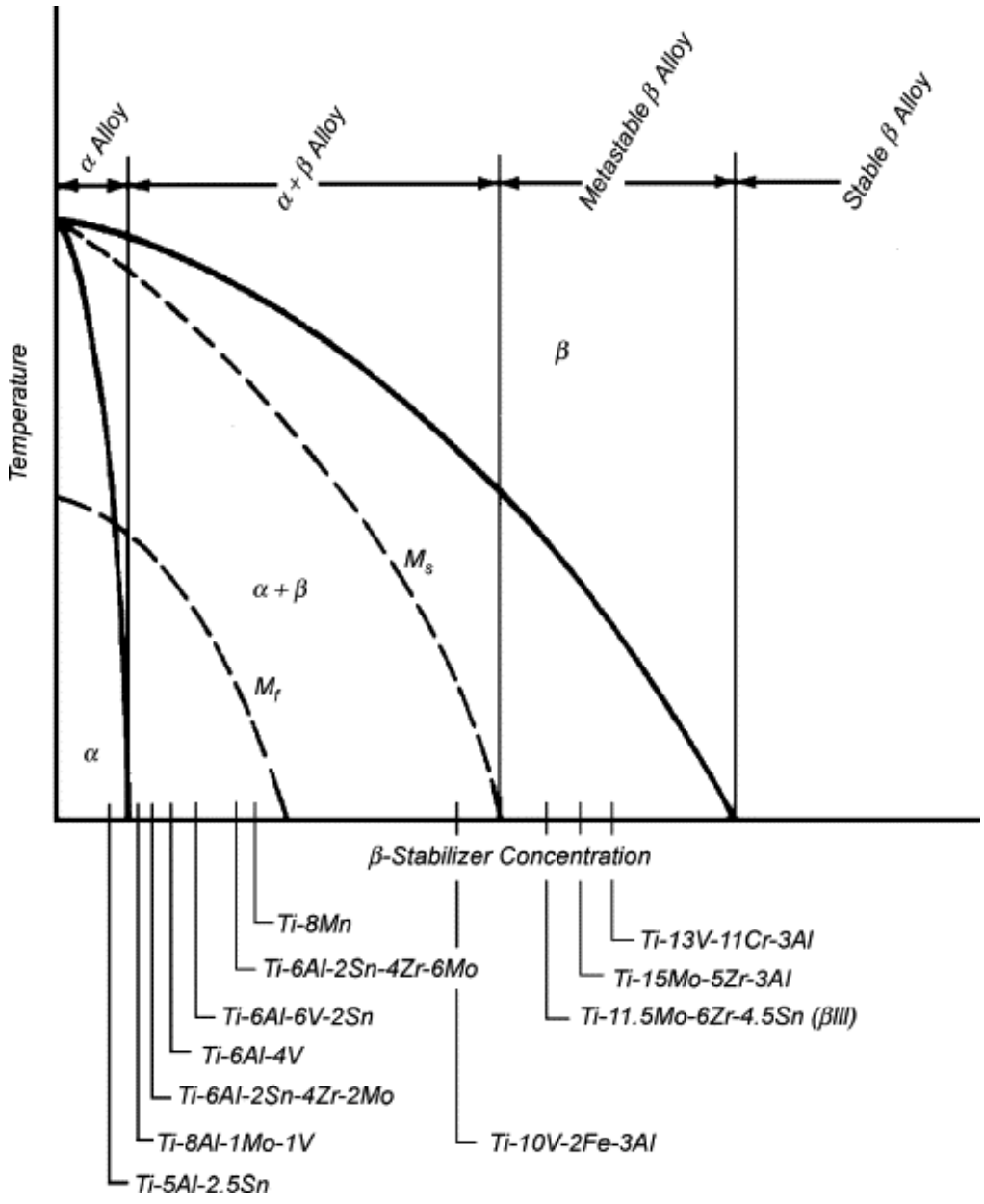

Figure 2-2 Pseudo-binary section through a-β isomorphous phase diagram (schematic) [54]

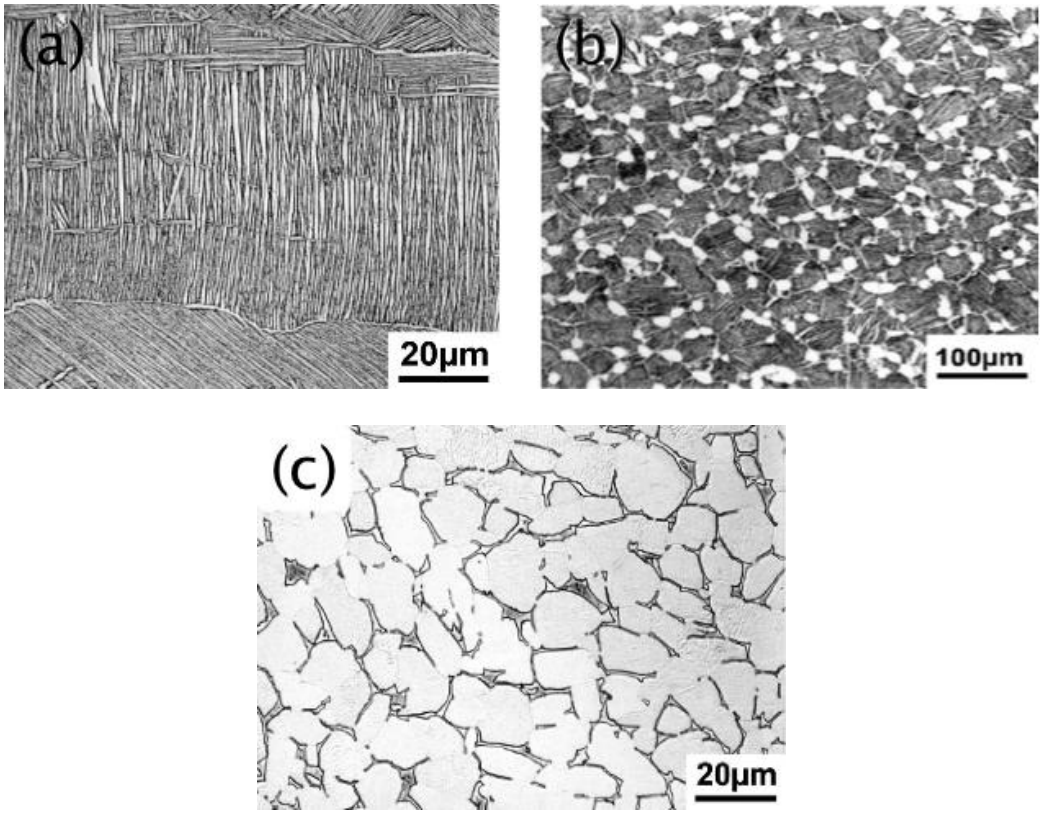

Figure 2-3 Optical micrographs showing (a) lamellar, (b) bi-modal and (c) equiaxed α+β titanium alloys [16].

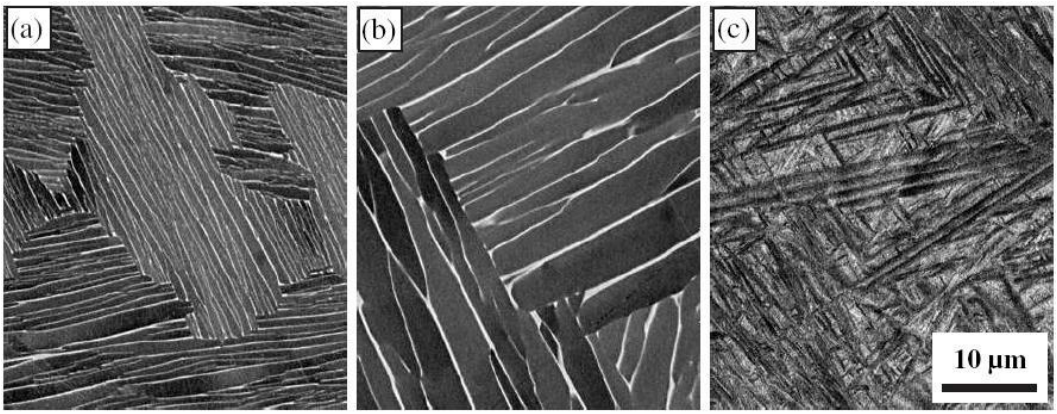

Figure 2-4 Scanning electron microscopy (SEM) images showing the microstructures of Ti-6Al-4V alloys formed with different cooling rates: (a) air cooled, (b) cooled in vermiculite and (c) water quenched [21].

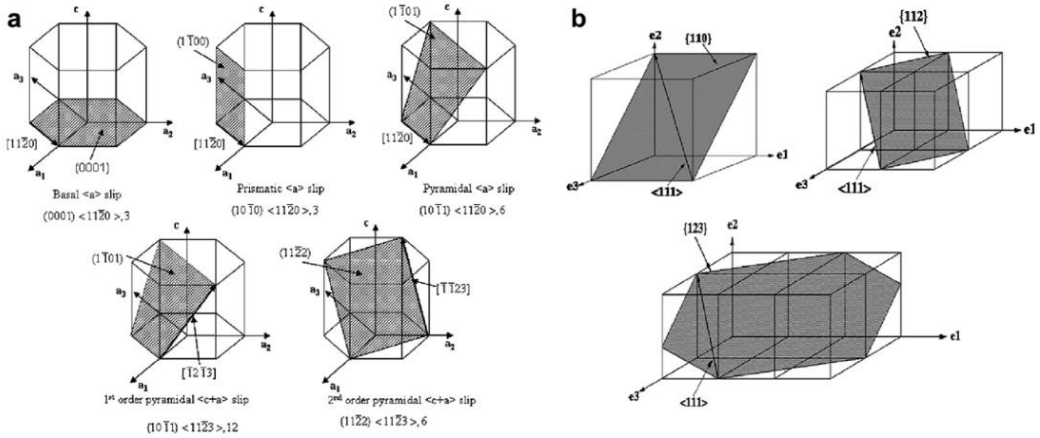

Figure 2-5 Slip systems in (a) h.c.p α phase and (b) b.c.c β phase [55]

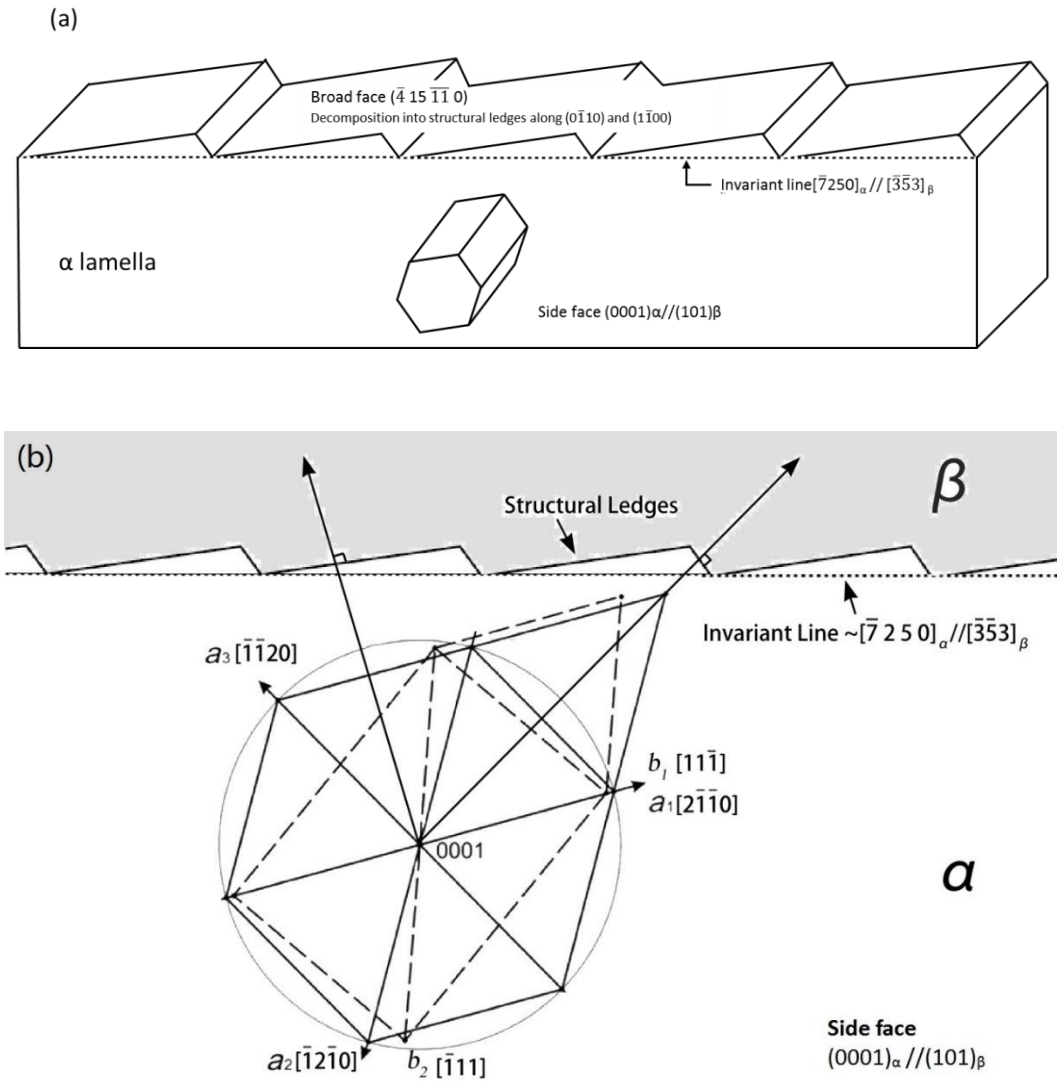

Figure 2-6 (a) A schematic model of the α lath growing along the invariant line and the structure of its interface (broad face and side face) with β. (b) Orientation relationship between α and β at the interface (broad face) when viewing along [0001] $_\alpha$*// [101]* $_\beta$ *(perpendicular to the side face) in the model shown in (a),* $\boldsymbol{a}_1 = a/3[2\bar{1}\bar{1}0]$, $\boldsymbol{a}_2 = a/3[\bar{1}2\bar{1}0]$, $\boldsymbol{a}_3 = a/3[\bar{1}\bar{1}20]$, $\boldsymbol{b}_1 = a/2[11\bar{1}]$, $\boldsymbol{b}_2 = a/2[\bar{1}11]$ *[32]. (c) The schematic showing the morphology of the α/β lamella microstructure accommodating the orientation relationship in (a) and (b).*

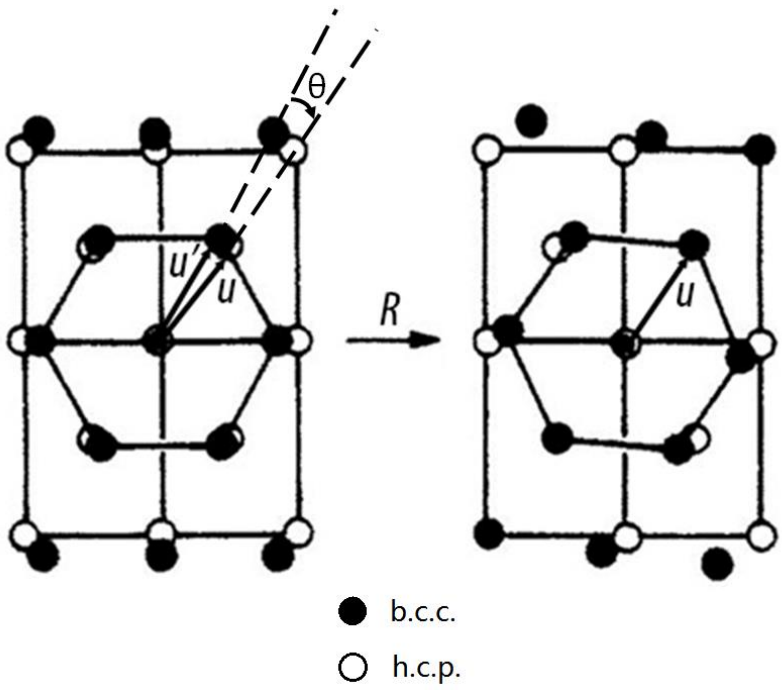

Figure 2-7 The formation of the invariant line during phase transformation from the b.c.c. (hollow circles) to the h.c.p. (solid circles) crystal structure. ***u*** *is the direction of the invariant line.* ***u****'* *is* ***u*** *after phase transformation，* ***u****'* *and* ***u*** *overlap after a rotation θ. [34]*

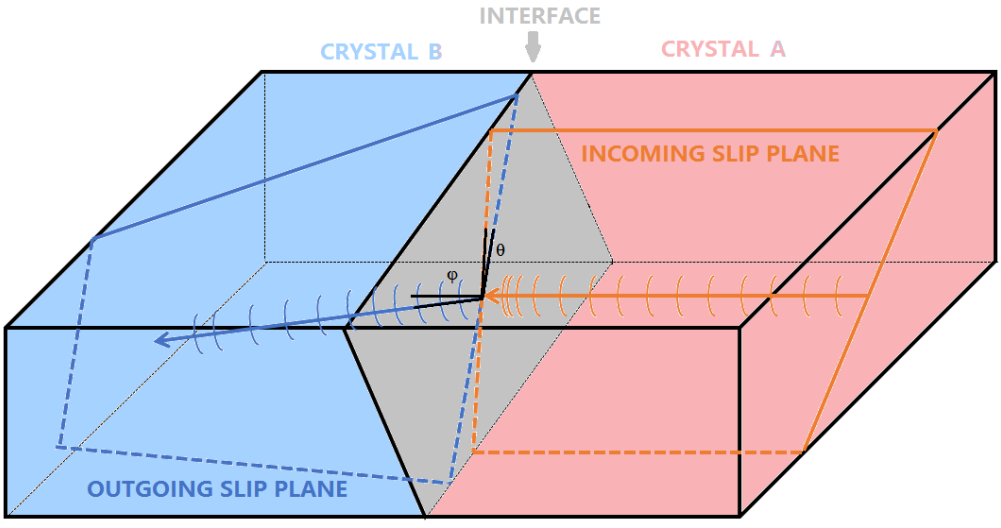

Figure 2-8 Schematic illustration of a slip system transmission through an interface. Angle θ between the two lines of intersections of two slip planes with the interface should be minimum for easy slip transmission. Angles φ between the two Burgers vectors should also be a minimum for easy transmission.

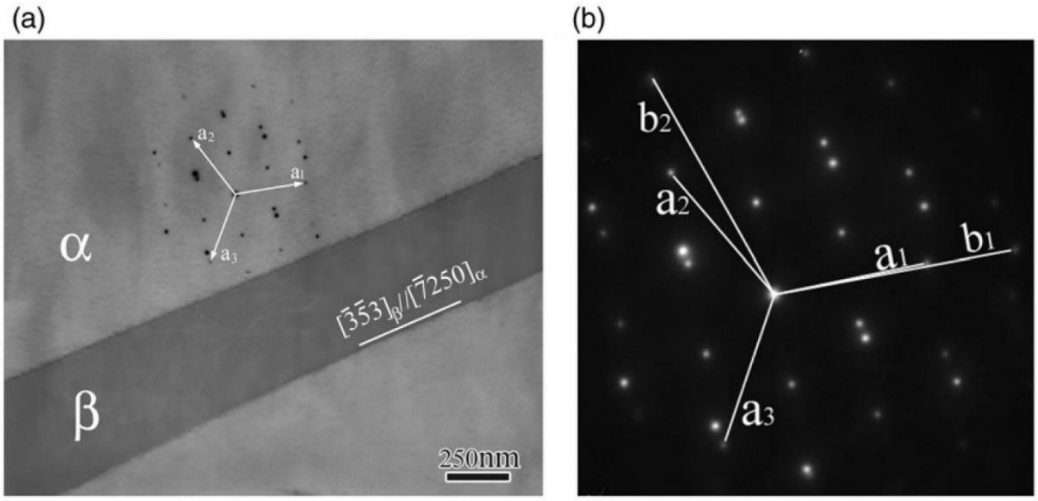

Figure 2-9 Bright-field TEM micrograph (a) with the SAD patterns (b) with the beam direction parallel to [0001]$_\alpha$// [101]$_\beta$ showing the relative inclinations of the three <11$\bar{2}$0>$_\alpha$ directions to the α-β interface in Ti-6Al-4V.[52]

Chapter 3 Sample size effect on the measured strength of crystalline materials

The dislocation-mediated plastic deformation involves the generation and movement of dislocations, which could be subjected to spatial and temporal constraints in bulk samples, which consequently varies with the microstructure and the volume of materials being tested. This section focuses on the role of sample size effect on the mechanical strength measured from crystalline materials.

3.1 Intrinsic size effect on the strength

The size effects can be classified into intrinsic size effects and extrinsic size effects [56]. The intrinsic size effects include those caused by the reduced microstructural feature sizes inside a crystal. For example, the grain size affects the strength of materials and following the Hall-Petch [57, 58] equation. For polycrystalline metal, the yield stress σ_y can be related to the grain size *d*:

$$\sigma_y = \sigma_0 + kd^{-n} \quad \textit{(Equation 3-1)},$$

where *k* is a constant, σ_0 is the lattice friction of the constituting single crystal, and *n* typically has a value of 0.5 [59, 60].

The flow stress $\sigma(\varepsilon)$ at a strain ε can be linked to the grain size *d* [61]:

$$(\varepsilon) = \sigma_0(\varepsilon) + k(\varepsilon)d^{-n} \quad \textit{(Equation 3-2)},$$

where $\sigma_0(\varepsilon)$ and $k\ (\varepsilon)$ are constants at the given strain ε. In both Equation 3-1 and

Equation 3-2, the key structure parameter is *d,* the grain size, or the distance between two neighboring grain boundaries. The smaller the grain size, the more additional strengthening to σ_0. However, as Figure 3-1 shows, there is a limit of the application of the normal Hall-Patch relationship [56]. When the grain size is decreased to about 40 nm, the plastic deformation mechanisms start to change from the dislocation mediated to the grain boundary mediated deformation such as grain boundary sliding, dislocation absorption at grain boundary, which lead to softening [62, 63].

3.2 Extrinsic size effect on the strength

The external size effect often refers to the external dimensions of the sample. Several principal mechanisms have been proposed to explain the sample size effect on strength such as geometrically necessary dislocations (GND) [64-67], dislocation starvation [1, 68, 69], and dislocation source truncation [70-73].

The sample size effect based on the concept of GND and strain gradient usually arises in the non-uniform plastic deformation [65, 74] such as nano-indentation [64, 67] or micro-bending test [66]. In the compression test of micro-pillars, the strain is much more homogeneous through the whole micro-pillar than that in the indentation and bending. In the sub-micrometer size range, the sample size effect observed in the compression of pillars has been attributed to the mechanism of dislocation starvation and surface nucleation. However, at larger pillar sizes, the single-arm dislocation source truncation mechanism was suggested to be dominant [68, 75]. Although both the dislocation starvation and the dislocation source truncation mechanism were proposed independently from different perspectives,

the two mechanisms are not necessarily exclusive in practice. Kiener and Minor [73] reported the observation of both dislocation starvation and dislocation source truncation in the in-situ TEM tensile test of Cu samples, which strengthened the micro-tensile sample at 100-200 nm width. In their work, there was a dislocation density drop by an order of magnitude in the deformed samples compared with the initial dislocation density in the sample. On the other hand, the yield strength increased from 636 MPa to 2.5 GPa corresponds to the spiral dislocation source size decrease from ~20 nm to ~3 nm.

The mechanisms of dislocation starvation and dislocation truncation will be discussed separately below.

3.2.1 Dislocation starvation

It is well known that in the plastic deformation of macroscopic samples, the dislocations multiplication and interaction lead to the strain hardening. Greer and Nix [68] firstly introduced the concept of dislocation starvation in the plastic deformation of small-scale samples. When gold micro-pillars of 200-7450 nm in diameter were compressed, they found that the micro-pillar had 50 times higher strength compared with their bulk counterparts with defects. They explained that when the samples became smaller than a few micrometers, mobile dislocations have a high probability of annihilating at a nearby free surface without multiplying or interacting with other dislocations. Therefore, the overall dislocation density was decreased and sample reached a dislocation starvation state when the existing dislocation sources exhausted. Further plastic deformation is accommodated by the nucleation and motion of new dislocations instead of the multiplication and

interactions of existing dislocations as is the case of macroscopic samples, resulting in a higher strength. In the TEM analysis, it has been proven in the literature [1, 68, 69] that the dislocation density drops with the strength increased in smaller samples.

3.2.2 Dislocation source truncation

The dislocation source truncation mechanism was proposed and confirmed in computer simulation [70-73, 76, 77]. Parthasarathy et al. [70] suggested that the sample size effect on strength can be rationalized by the stochastics of dislocation source length in a sample of a finite size. The dislocation source length can be derived as a function of the sample size.

Theoretically, the CRSS of the micro-scale crystal is the stress required for the first percolation of a dislocation across the sample [78] and it is largely dependent on the initiation of the dislocation multiplication from the shortest source length, typically the double-pinned Frank-Read source [79]. The stress required to bow a Frank-Read source in a bulk sample is defined by [80]

$$\sigma = \frac{Gb}{L} \quad \textit{(Equation 3-3),}$$

where G is the shear modulus, $\boldsymbol{b}$ is the Burgers vector and L is the source length. However, in the model of the micro-pillar sample with a finite dimension, all the double-pinned Frank-Read sources will end up with the interaction with the micro-pillar sample surface. It is because the sample dimension is limited and in the same order of magnitude with the source length. This interaction results in a truncated single-ended source, which has one end pinned and the other at the free surface of the micro-pillar, as schematically shown in Figure 3-2.

The CRSS of a micro-pillar sample containing single-ended sources can then be given by

$$\text{CRSS} = \frac{\alpha G \boldsymbol{b}}{\bar{L}} + 0.5G\boldsymbol{b}\sqrt{\rho} + \tau_0 \quad \textit{(Equation 3-4),}$$

where α is a geometrical constant, G is the shear modulus, $\boldsymbol{b}$ is the Burgers vector, τ_0 is the friction stress, ρ is the total dislocation density, $\bar{L}$ is the mean value of source length. The first part is the stress for activation of Frank–Read sources. The second part is for the strengthening from dislocation interaction given by the Taylor equation [81]. The τ_0 is the friction stress to move a dislocation through an otherwise perfect lattice given by the Peierls-Nabarro equation:

$$\tau_0 = 3G\, exp - (2\pi w/\boldsymbol{b}) \quad \textit{(Equation 3-5)}$$

where w is the dislocation width [80].

3.3 Power-law relationship between strength and sample extrinsic size

Since the report from Uchic et al in 2004 [11] on the sample size effect on the strength of Ni_3Al, many micro-pillar compression experiments have been performed on different materials. The relationship between the measured strength σ and the sample extrinsic size D is often described by the power-law relationship, $\sigma \propto D^{-n}$. It has been suggested [82, 83] that the interpretation of the sample size effect using the power-law relationship is unphysical as the strength predicted would continuously decreases with increasing sample size, or approaching infinite when the sample size is decreased to atom scale. Therefore, the simple power law

relation was corrected into

$$\tau = \tau_0 + AD^{-n} \qquad (Equation\ 3\text{-}6)$$

where τ and τ_0 represent the CRSS of the micro-scale sample and the macroscopic sample respectively, and *A* is constant [83, 84]. Apparently, this has not extended the applicability of the power law relation to very small sample sizes. Experimentally, the values of the exponent *n* vary with materials and the stronger material displays the less pronounced sample size effect, e.g. 1~0.6 for f.c.c. metals, 0.5 or less for b.c.c. metals, and as low as 0.2 or less for ceramics [83]. While the sample size effect on strength has been widely studied in f.c.c. [1, 3, 8, 85] and b.c.c. [86-90] single crystals, only a few studies on h.c.p. crystals have been carried out [84, 91, 92]. For example, Sun et al. [92] studied the sample size effect on the strength of single-crystal commercially pure (CP) Ti loaded along [$11\bar{2}0$], which activated two <***a***> prismatic slip systems. They found that the flow stress increases significantly with the decreasing micro-pillar size in the range from 3 μm to 350 nm. The flow stress σ_f at 5% plastic strain was linked to the micro-pillar diameter *D* using a power law relationship with the power exponent *n* of 0.5. They calculated the CRSS using the source truncation theory [70] and it showed the experimental CRSS inversely scales with the micro-pillar size.

Although a large range of sample sizes fit the power law relationship with the strength measured, there is no convincing theory explaining the physical meaning of the exponent *n* at the beginning of the research. Simulations [71] and experiments [93] had proved in micro-pillars that initial dislocation density also has an influence on the size effect. Increasing the initial dislocation density reduces the observed

sample size effect. On the contrary, decreasing the initial dislocation density can increase the magnitude of the sample size effect observed on the yield stress and flow stress and resulting in increasingly stochastic mechanical responses.

Based on the large numbers of data acquired from previous researches, Huang et al. [94] tried to fit the modelled data with them and constructed an equation for the scale exponent of the sample size effect from the aspect of stochastic dislocation formation in crystalline metals to explain the physical meaning of *n*:

$$n = \begin{cases} 1 - \frac{\mu(\tau+1)}{\alpha} = n_1, \ \rho \ll \rho_c \\ \frac{\mu(\tau+1)}{\alpha} = n_2, \ \rho \gg \rho_c \end{cases} \qquad \textit{(Equation 3-7)}$$

where *n* was discussed in two different conditions, depending on whether dislocation density $\rho \ll \rho_c$ or $\rho \gg \rho_c$. ρ_c is the transition value of dislocation density (inversely proportional to the sample size) between dislocation source activation dominant region and dislocation forest hardening dominant region. Constant μ = 0.5. τ is the exponent in the envelope distribution for the normalized strain [95]. α is the effective mean number of dislocations nucleation during the plastic deformation (dislocation nucleation rate over dislocation recovery rate), which is also proportional to the dislocations sources or the slip systems can be activated in a single crystal. For the intermediate region that $\rho < \rho_c$ or $\rho > \rho_c$,

$$n = \begin{cases} n_1 - (n_1 + \mu - 1)(1 + c_3 \left(\frac{1}{d}\right)^{1-\frac{1-n_1}{\mu}})^{-1}, \ \rho < \rho_c \\ n_2 - (n_2 - \mu)(1 + c_4 \left(\frac{1}{d}\right)^{\frac{n_2}{\mu}-1})^{-1}, \ \rho > \rho_c \end{cases} \qquad \textit{(Equation 3-8)}$$

where c_3 and c_4 are both constants. These equations quantitively explained the experimental observation on the influence of the crystal structure [83], initial

dislocation density [71, 93] on the power-law exponent n by assuming different α values.

3.4 The influence of β phase and α/β interfaces in micro-scale samples

At the micro-scale, samples can be extracted from certain grains with desirable orientations. In the last decade, different slip systems (basal /prismatic <***a***> slip [52, 84, 91, 96], 1st/2nd order pyramidal <***c+a***> slip [10, 29, 91]) in titanium alloys were activated by deforming micro-scale specimens along different orientations. The strength of these specimens was either directly measured from the micro-pillars [29, 96, 97] or derived by fitting finite element analysis (FEA) modelling data with the deformed micro-cantilevers stress-strain curves [10, 52, 84, 91].

Because the interface usually acts as a barrier for dislocation transmission, it strengthens the sample. This was also confirmed at micro-scale titanium alloys. For the single crystal micro-scale samples, Gong and Wilkinson [91] modelled the bending of CP-Ti micro-cantilevers of 5 μm width and determined the CRSS of 209 MPa for $\boldsymbol{a}_3$ basal slip, 181 MPa for $\boldsymbol{a}_3$ prismatic slip and 474 MPa for the 2nd order pyramidal <***c+a***> slip by fitting to the experimental data. For the polycrystalline samples, Gong and Wilkinson [84] also completed a series of similar experimental and modelling tests for Ti-6Al-4V which containing several β layers in the micro-cantilevers. Comparing the micro-cantilevers with the same sizes between CP-Ti, Ti-6Al and Ti-6Al-4V, the modelling results for CRSS of bulk sample is 127 MPa, 287 MPa and 424 MPa [84]. In the micro-cantilevers of 5 μm width, the CRSS increased to 183 MPa, 347 MPa and 483 MPa for $\boldsymbol{a}_3$ prismatic slip system [84]. Ding et al. [10] filled the gap by bending the Ti-6Al-4V micro-cantilevers of 5 μm

width with <***c+a***> dislocations on the 1st order pyramidal plane activated. The CRSS is calculated as 690 MPa. They attributed this increase of the strength to the interfaces in the micro-cantilevers [84]. In other words, both <***a***> and <***c+a***> slips in Ti-6Al-4V micro-cantilevers have higher CRSS than those in CP-Ti, as a result of the α/β interface strengthening [10]. Ding et al. [52] have confirmed the α/β interface strengthens Ti-6Al-4V micro-cantilevers deformed with $\boldsymbol{a_3}$ prismatic slips, but whether the α/β interface has a similar strengthening effect on the $\boldsymbol{a_1}$ / $\boldsymbol{a_2}$ prismatic slips, which can transmit through the interface more easily, remains unknown.

Apart from the interfaces, the effects from β phase should also be considered. Jun et al. [96, 97] discussed the effect of β phase morphology in compressed Ti-6Al-2Sn-4Zr-2Mo micro-pillars. Jun et al [96, 97] and Zhang et al. [45] did a series of compression test of Ti-6Al-2Sn-4Zr-2Mo micro-pillars with the α/β/α structure and activated either $\boldsymbol{a_1}$ / $\boldsymbol{a_2}$ basal or $\boldsymbol{a_3}$ prismatic slips. The micro-pillars with different morphology and volume fractions of the β phase influenced the yield strength and work-hardening of the pillars. Generally, the more β phase volume fraction in the pillar leads to the weaker strength and lower hardening rate [96]. However, there is no quantitative analysis due to unknown morphology and volume fractions of β phase in the FIB milled micro-pillars.

The interface not only influences the CRSS at micro scales but also has an effect on the sample size effect. Bi-crystalline or polycrystalline micro-pillars and micro-cantilevers with grain boundaries have also been studied via experiments or computer simulations [52, 55, 84, 85, 98], in order to understand the role of grain boundaries in the plastic deformation and therefore the sample size effect on

strength [22]. Kunz et al. [85] observed that both Al single crystal and bicrystal samples have very similar sample size effect on the strength. They measured the sample size effect on the strength in single crystal samples (the power exponent n = 0.63) and in the bi-crystal under the same conditions (n = 0.59) with the pillar diameter ranging from 400 nm to 2 μm. However, it should be noted that it was the flow stress at 7.5% strain instead of the yield stress was used, because of the uncertainty of the contact between punch and micro-pillars at the beginning of compression. The change of the sample size effect scale was explained by that the grain boundaries decreased the work hardening rate and acted as dislocation sinks rather than sources in the micro-pillars. Gong and Wilkinson [84, 91] have repeated the systematical bending tests on CP-Ti, α Ti alloys and α+β Ti alloys cantilevers of different sizes orientated for <***a***> prismatic slips. They also reported α/β boundary had an effect on the sample size effect of strength. In terms of the <***a***> prismatic slip, the strength measured from the CP-Ti exhibited the most pronounced sample size effect compared with that measured from Ti-6Al and Ti-6Al-4V alloys. The power law relationship between the critical resolved shear stress (CRSS) and the cantilever width gave the exponent of 0.56 for CP Ti. A much smaller exponent of 0.29 and even smaller exponent of 0.21 have been determined from Ti-6Al and Ti-6Al-4V, respectively.

The compressive CRSS values of different types slip systems in Ti alloys reported in the literature mentioned in Chapter 2 and 3 are summarized in Table 3.1. Generally, the smaller sample has a higher CRSS. However, there are several knowledge gaps among these results:

- **The effect of the α/β interface on the strength.** Some reports [85, 96] showed that the interface weakened the CRSS while others [10, 52, 84] reported completely opposite results where the interface strengthened the CRSS. There is a coincidence that in the micro-scale samples with <***a***> type dislocations activated, only the $\boldsymbol{a_3}$ prismatic dislocations were activated in different groups of researchers on Ti alloys micro-pillars [96] and micro-cantilevers [52, 84]. The $\boldsymbol{a_1}$ dislocations, which can transmit the α/β interface much more easily than the $\boldsymbol{a_3}$ dislocations, has not been studied in the micro-scale samples yet.
- **The effect of the α/β interface on the sample size effect.** Although the Ti-6Al-4V micro-cantilever bending tests have been used to derive the CRSS with the assistance of the FEA modelling, there was no direct experimental measurement using the micro-pillar compression. The mechanism and influence factors of size effect in Ti-6Al-4V remain to be confirmed.
- **The <*c*+*a*> slip system activation and its interaction with the α/β interface.** Some literatures [10, 91] reported the <***c+a***> dislocations on the 1st order pyramidal plane $\{10\bar{1}1\}$ while others [29] reported on the 2nd order pyramidal plane $\{\bar{1}\bar{1}22\}$. The interaction of <***c+a***> dislocations with the interface and the presence of the sample size effect on the strength when <***c+a***> dislocations dominate remain unknown.

Therefore, to have a further investigation on the above points, micro-compression tests will be performed on the single-phase/two-phase Ti-6Al-4V micro-pillars of different diameters. Apart from the sample size effect on the strength which is widely reported in the literature, its underlying causes and its

relationship with the influence of the α/β interface will be studied after observing the dislocations arrangement within the plastically deformed micro-pillars by using the post-mortem TEM analysis.

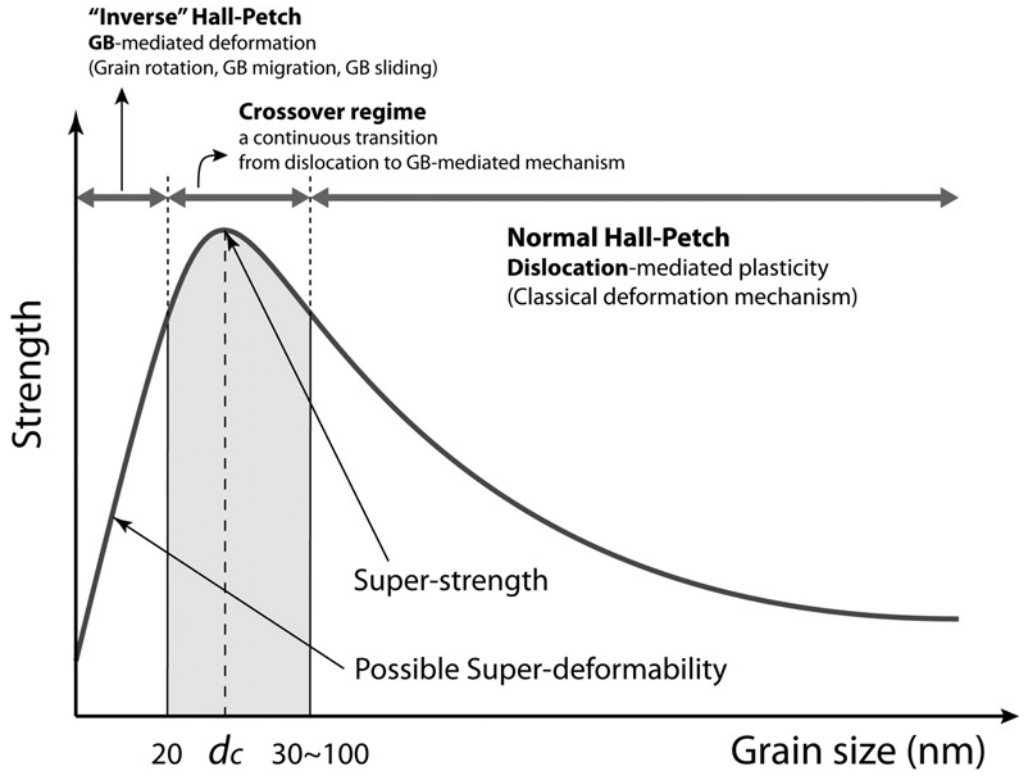

Figure 3-1 Strength of polycrystalline materials as a function of grain size: Hall–Petch relation [56]

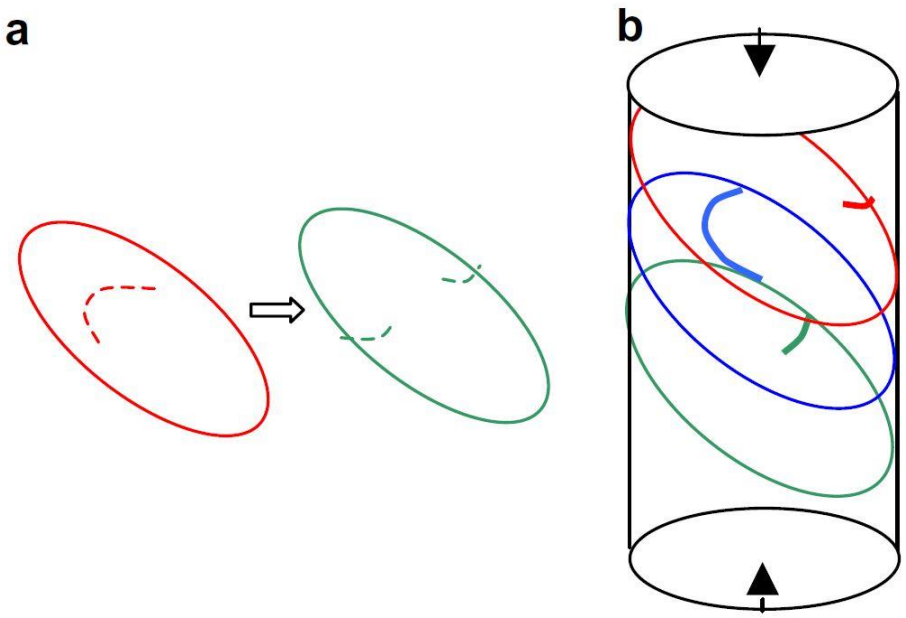

Figure 3-2 The schematic sketch explaining the dislocation source truncation (a) schematic sketch of how double-pinned Frank-Read sources quickly become single-ended sources in samples of finite dimensions. (b) Schematic sketch of single-ended sources in a finite pillar.[70]

Table 3.1 Some bulk, mico and modelling compressive CRSS values of Ti alloys reported in the literature.

Slip system activated	Compression CRSS (MPa)	Condition
<***a***> basal	444	Ti-6Al-4V bulk sample [24]
	209	Modelling CP-Ti micro-cantilever, 5 μm width, without β [91]
	401	Ti-6Al-2Sn-4Zr-2Mo micro-pillar, a_1 basal, 2 μm diameter, without β [96]
	294	Ti-6Al-2Sn-4Zr-2Mo micro-pillar, a_1 basal, 2 μm diameter, with β [96]
	354	Ti-6Al-2Sn-4Zr-2Mo micro-pillar, a_2 basal, 2 μm diameter, with β [96]
<***a***> prismatic	392	Ti-6Al-4V bulk sample [24]
	181	Modelling CP-Ti micro-cantilever, a_3 prismatic, 5 μm width, without β [91]
	424	Modelling Ti-6Al-4V bulk sample [84]
	484~752	Modelling Ti-6Al-4V 10 μm ~1 μm width micro-cantilever [84]
	340	Modelling Ti-6Al micro-cantilever, a_3 prismatic, 3 μm width, without β [52]
	480	Modelling Ti-6Al-4V micro-cantilever, a_3 prismatic, 3 μm width, with β [52]
	287-612	Modelling Ti-6Al 10 μm ~1 μm width micro-cantilever [84]
	327	Ti-6Al-2Sn-4Zr-2Mo micro-pillar, a_3 prismatic, 2 μm diameter, without β [96]
<***a***> pyramidal	404	Ti-6Al-4V bulk sample [24]
1st order pyramidal <***c***+***a***>	631	Ti-6Al-4V bulk sample [24]
	690	Modelling Ti-6Al-4V micro-cantilever, 5 μm width, with β [10]
2nd pyramidal <***c***+***a***>	474	Modelling CP-Ti micro-cantilever, 5 μm width, without β [91]

Chapter 4 Materials and Experimental Methods

A commercial Ti-6Al-4V alloy (the composition as shown in Table 4.1 was determined using Energy-dispersive X-ray spectroscopy (EDS)) was used in this study.

4.1 Heat-treatment and microstructure

To prepare micro-pillars containing α/β interfaces needed to investigate the role of the interface in the plastic deformation, heat-treatment was performed to achieve a fully lamellar microstructure. Specimens of 6 mm × 6 mm × 10 mm were extracted carefully from the as-received Ti-6Al-4V bar using electric discharge machining (EDM) and then heat-treated in a vacuum furnace following a procedure as shown in Figure 4-1. The samples were degassed at 200 °C in the vacuum furnace for 30 mins, and then heated to 1050 °C and maintained for 1 hour. Following this, the samples were cooled at 0.1 °C/min down to 700 °C and then furnace cooled.

After the heat-treatment, the specimens were ground carefully and cut into smaller buttons (5 mm × 5 mm × 4 mm) for micro-pillar preparation. The top surface of the button samples where the pillars were located was carefully polished with a mixture of colloidal silica (OP-S) and hydrogen peroxide (30%) for 20 min. Electron backscatter diffraction (EBSD) was carried out to identify the location with prescribed orientations for the micro-pillars preparation.

The optical micrograph in Figure 4-2 shows the microstructure of the Ti-6Al-4V sample after the heat treatment at low magnification. The α-β colonies ranged in

size from 0.5 to 3 mm. Figure 4-3 (a) and (b) are the SEM images showing the typical microstructures after heat treatment in different colonies. The dark regions correspond to α phase, whereas the thin bright regions are the β phase. The α laths are of 10 μm to 50 μm thick and with the β ranging from 0.5 μm to 10 μm thick. The typical microstructure in the colony with $[1\bar{1}00]$ normal to the paper plane is shown in Figure 4-3 (a) and the typical microstructure in the colony with [0001] normal to the paper plane in Figure 4-3 (b).

4.2 EBSD mapping and Schmid factor calculation

EBSD was used to map out the orientation of α/β colonies, as shown in Figure 4-4. To activate <***a***> prismatic and <***c***+***a***> slips, two colonies with $[1\bar{1}00]$ and $[000\bar{1}]$ normal directions in α phases were selected. The three Euler angles of colony #1 in Figure 4-4 are 2.8°, 90.0°, 33.5°. Therefore, the normal direction is 6.3° away from $[1\bar{1}00]$, the perfect loading direction to activate the <***a***> prismatic slip. The three Euler angles of colony #2 in Figure 4-4 are 102.0°, 2.4°, 46.0°, which means the normal direction is 2.4° away from [0001] of the α phase. This loading direction has higher possibility of activating <***c***+***a***> slips. In both colonies, the α and β phases follow the Burger's orientation relationship $(0001)_\alpha$ // $(101)_\beta$, $[2\bar{1}\bar{1}0]_\alpha$ // $[11\bar{1}]_\beta$, as shown in Figure 4-5. Therefore, the corresponding normal direction of β phase is close to $[10\bar{1}]$ in colony #1 and $[\bar{1}0\bar{1}]$ in colony #2, which are expected to activate slip systems belong to the same family in the β phase in these two colonies. The designation of the crystallographic relationship across the α/β interface follows that $\boldsymbol{a}_1 = [2\bar{1}\bar{1}0]$, $\boldsymbol{a}_2 = [\bar{1}2\bar{1}0]$, $\boldsymbol{a}_3 = [\bar{1}\bar{1}20]$, and $\boldsymbol{b}_1 = [11\bar{1}]$, $\boldsymbol{b}_2 = [\bar{1}11]$. This designation and orientation relationship will be used throughout the thesis.

In the b.c.c. crystal structure, Schmid factor can be calculated as

$$m = \cos\varphi\cos\lambda = \frac{u_1u_2+v_1v_2+w_1w_2}{\sqrt{(u_1{}^2+v_1{}^2+w_1{}^2)(u_2{}^2+v_2{}^2+w_2{}^2)}}\frac{u_1u_3+v_1v_3+w_1w_3}{\sqrt{(u_1{}^2+v_1{}^2+w_1{}^2)(u_3{}^2+v_3{}^2+w_3{}^2)}}$$

(Equation 4-1),

where $[u_1v_1w_1]$ is the loading direction, $[u_2v_2w_2]$ the slip direction and $[u_3v_3w_3]$ the normal direction of the slip plane.

In the h.c.p crystal structure, Schmid factor can be calculated as

$$m = \cos\varphi\cos\lambda =$$

$$\frac{u_1u_2+v_1v_2+t_1t_2+\frac{2c^2}{3a^2}w_1w_2}{\sqrt{(u_1{}^2+v_1{}^2+t_1{}^2+\frac{2c^2}{3a^2}w_1{}^2)(u_2{}^2+v_2{}^2+t_2{}^2+\frac{2c^2}{3a^2}w_2{}^2)}}\frac{u_1u_3+v_1v_3+t_1t_3+w_1w_3}{\sqrt{(u_1{}^2+v_1{}^2+t_1{}^2+\frac{2c^2}{3a^2}w_1{}^2)(u_3{}^2+v_3{}^2+t_3{}^2+\frac{3a^2}{2c^2}w_3{}^2)}}$$

(*Equation 4-2),*

in which $[u_1v_1t_1w_1]$ is the loading direction, $[u_2v_2t_2w_2]$ the slip direction and $[u_3v_3t_3w_3]$ the normal direction of the slip plane [99] and c/a = 1.587 for α phase in Ti-6Al-4V [13].

Based on Equation 4-2, Schmid factors were calculated for all potential slip systems in h.c.p. crystal structure and are listed in Table 4.2. 48 slip systems and the associated Schmid factors in the b.c.c. crystal structure is listed in Table 4.3. These two tables were used to analyse slip systems in Chapter 6.

4.3 Fabrication of micro-pillars

Micro-pillars with diameters in the range from 0.5 μm to 5 μm were prepared using an FEI Quanta 3D FIB/SEM. The experiment conditions used for the micro-pillar

preparation are listed in Table 4.4. The aspect ratio between the pillar height and diameter was controlled at about 2:1 to minimise the plastic instability during the deformations (e.g. higher ratio may cause buckling while lower ratio additional hardening). In the micro-pillars containing both the α and β phases, the thickness of the β fillets was selected to be ~ 30% of the diameters of the micro-pillars. Depending on the crystallography orientation of the pillars, the α/β interfaces have different angles with regards to the axis of the micro-pillars. Figure 4-6 (a) shows in the pillar with $[000\bar{1}]$ loading direction, the β phase lathe goes through the micro-pillars from top to bottom. While in Figure 4-6 (b) with $[1\bar{1}00]$ loading direction, the β phase lathe goes through the micro-pillars at an inclined angle. 50 micro-pillars were prepared in this study and the details are listed in Table 4.5. Attention was paid to reduce the taper angle (less than 4°) so as to minimise the non-uniform stress within the micro-pillars during the subsequent compression test [7, 100, 101].

4.4 Strengthening of ion irradiation damage layer

When FIB is used to prepare micro-pillars, there is a concern that the irradiation damage layer introduced by the energetic Ga+ on the sample surface may alter the mechanical properties of the material [7]. To investigate if the irradiation damage layer affects the mechanical properties of Ti-6Al-4V, indentation tests were performed on the surface near and far from the fabricated micro-pillars.

The indentation test was performed in the load-control mode. The max load was applied to 10 mN and the max depth of the indentation was between 600-650 nm. The load-displacement curves in Figure 4-7 show no obvious difference between the surface near and far from the fabricated micro-pillars. The hardness and reduced

modulus are given by the test and reduced modulus E_r is related to the modulus of elasticity E_{sample} as:

$$\frac{1}{E_r} = \frac{1-\nu^2}{E}_{sample} + \frac{1-\nu^2}{E}_{indenter} \quad \textit{(Equation 4-3)}$$

Where the ν is Poisson's ratio. For a standard diamond indenter probe, $E_{indenter}$ is 1140 GPa and $\nu_{indenter}$ is 0.07. Poisson's ratio ν for Ti-6Al-4V is 0.27. Therefore, the average values of Young's modulus for the ion-free area is 135.8 GPa and 135.2 GPa for the ion irradiated area. The elastic modulus along [0001] loading direction in CP-Ti is 146.2 GPa [102]. The average hardness is 5.4 GPa for the ion-free area and 5.9 GPa for the ion irradiated area, as listed in Table 4.6.

The results show that at this scale there is hardly any effect on E but the ion irradiation may slightly increase the hardness of Ti-6Al-4V. It has been reported that as a factor of two on the hardness was observed at the depth less than 100 nm [7], this strengthening effect is still negligible at the scale used in the current project. The hardness results obtained are close to the literature values [103] considering the slight deviate from [0001] in the current experiment.

4.5 Uniaxial Compression Test

Compression tests on the prepared micro-pillars were carried out on a Hysitron PI85 Pico Indenter with a 20 μm flat-end diamond probe. The tests were carried out in a Tescan Mire 3 SEM. The micro-pillars were compressed under the displacement-control mode via a closed feedback loop until a final nominal strain of 5% - 10%.

To exclude the strain-rate effect on the compression results [97], a nominal constant strain rate of 2.5×10^{-4} s^{-1} was used in all tests. To eliminate the influence of the substrate deformation during the compression, Sneddon correction was applied to accurately measure the change of pillar length using the equation [101]:

$$\Delta l_{pillar} = \Delta l_{total} - \Delta l_{substrate} - \Delta l_{probe}$$

$$= \Delta l_{total} - \frac{(1-v_{sub}^2)\cdot F}{2E_{sub}\cdot r_{bottom}} - \frac{(1-v_{ind}^2)\cdot F}{2E_{ind}\cdot r_{top}} \quad \textit{(Equation 4-4)},$$

where v_{sub} and v_{ind} are the Poisson's ratios of substrate and indenter. F is the applied force on the top of micro-pillars. E_{sub} and E_{ind} are the elastic moduli of the substrate and indenter. r_{bottom} and r_{top} are the bottom and top radius of micro-pillars. E_{ind}, the elastic modulus of the diamond probe used in this compression test, is 1140 GPa and its Poisson's ratio is 0.07. The typical compressive elastic modulus for Ti-6Al-4V (α+β microstructure) substrate at room temperature E_{sub} is measured 129 GPa, and the Poisson's ratio around 0.27 [13].

Engineering stress and strain σ_E and ε_E were calculated using equations:

$$\varepsilon_E = \frac{\Delta l_{pillar}}{l_0} \quad \textit{(Equation 4-5)},$$

$$\sigma_E = \frac{F}{\pi {r_{top}}^2} \quad \textit{(Equation 4-6)},$$

where l_0 is the height of micro-pillar. To calculate the stress, the pillar top diameter (rather than its average diameter) was used as experimentally yielding always started at the top part of the pillars. True stress σ_T and true strain ε_T were used in final stress-strain curves plot. They were calculated using the equations:

$$\varepsilon_T = \ln (1 + \varepsilon_E) \quad \textit{(Equation 4-7)},$$

$$\sigma_T = \sigma_E (1 + \varepsilon_E) \quad \textit{(Equation 4-8)}.$$

Because of the difficulty in the determination of yield point, the yield stresses were determined at 0.2% offset yield point. The elastic modulus was calculated from the average slopes of the linear parts of the loading stress-strain curves.

4.6 TEM sample preparation

TEM foils were prepared from the compressed micro-pillars using the FIB. All TEM foils were extracted parallel to the pillar axis and perpendicular to the slip plane, as shown in Figure 4-8. In this way, the TEM foils are likely to contain most of the dislocations contained in the pillars (from top to the bottom), which makes the subsequent dislocation analysis more straightforward. As the orientation of the micro-pillars and the TEM foil preparation were well controlled crystallographically, the orientations of α/β interfaces in different colonies are known as summarized in Figure 4-9.

Representative micro-pillars (9 in total) were selected and further studied by TEM. The selection of the pillars covers (1) different micro-pillar sizes, (2) different α/β crystal orientations, (3) different β phase content and (4) different strain levels.

The TEM foil extraction using FIB is shown in *Figure 4-10*. The micro-pillar was tilted at 52°. At this angle, the axis of the micro-pillar is parallel with the ion beam direction. The Gas Injection System (GIS) was inserted and a rectangular of Pt was deposited on the top of the micro-pillar. The ion beam voltage of 30keV and the

current of 10 pA/μm^2 were used for the deposition. A 3μm thick Pt layer was deposited. The micro-pillar was then tilted back to 0° and rotated ± 90° to deposit the sides of micro-pillar with same deposition parameters.

After the deposition, the sample was tilted at 52°. Trenches were dug around the micro-pillar which was then milled into a lamella using the ion beam at 30 keV and 3 nA until the lamella thickness of about 1 μm.

The next stage is to lift out the lamella using the Omniprobe. The stage was tilted back to 0° and the Omniprobe was carefully controlled to approach the top of the lamella. GIS was used to weld the probe with the sample. The ion beam voltage of 30 kV and current of 10 pA/μm^2 based on the deposition area were used for the welding. The lamella was then cut off from the bottom and lifted out.

The final sage is to fix the lamella onto a Cu grid and final polishing. The stage was at 0° and the Omniprobe was moved to the single-arm tip of the Cu grid. The lamella was welded to the tip using the Pt deposition at 30 kV and 10pA/μm^2 depending on the deposition area. The Omniprobe was then cut off from the lamella and retracted. The stage was rotated 180° and the other side of welding point was Pt deposited. The stage was tilted at 52° for TEM sample precision milling. The lamella was thinned from both sides using the ion beam at 30 kV and 0.3 ~ 1 nA. When the sample thickness was reduced to about 600 nm, the stage was tilted ± 1° away from the ion beam and a final cleaning cross-section pattern was applied on both sides of the TEM sample under the 30 kV and 0.1 nA beam current till the sample thickness was reduced to ~200nm which is thin enough for Ti-6Al-4V.

FIB milling usually induced defects on the prepared TEM foils [104-106]. Experiments and simulations have shown that the thickness of the damage layer is independent of the ion beam current but dependent on the beam voltage, the incidence angle of the ion beam and the material being milled [104, 105]. Low ion beam energy 5 kV (the lowest usable voltage) and 48 pA was used and TEM sample was tilted ± 6° away from the ion beam for the final polishing on both sides. The conditions were summarised in Table 4.7.

4.7 Dislocation analysis

Dislocation analysis of the compressed pillars was carried out on an FEI Tecnai F20 TEM operated at 200 kV.

The slip system determination included the dislocation Burgers vector $\boldsymbol{b}$ determination based on the invisibility criterion $\boldsymbol{g}\cdot\boldsymbol{b} = 0$ [80] and the slip plane determination based on the edge-on condition. Usually, dislocation appears as a dark curved line in the bright field TEM image, because the bent plane near the dislocation changed the intensity of the directly transmitted beam. At a two-beam condition (only the directly transmitted beam and one diffracted beam were strongly excited), if the diffraction vector $\boldsymbol{g}$ is perpendicular to $\boldsymbol{b}$ ($\boldsymbol{g}\cdot\boldsymbol{b} = 0$), the dislocation becomes invisible (or associated with very weak contrast). If another $\boldsymbol{g}$ can be found to make the dislocation invisible by tilting the specimen in the TEM, the $\boldsymbol{b}$ can be determined by $\boldsymbol{g}_1 \times \boldsymbol{g}_2$. As the orientation of the micro-pillar was known and that the activated slip systems predictable, one $\boldsymbol{g}$ is sufficient to confirm the $\boldsymbol{b}$ for the slip systems in the α phase listed in Table 4.2, and in the β phase listed in Table 4.3. The slip plane can be determined by the edge-on condition when the slip plane is

tilted in parallel to the electron beam direction. All dislocations on this plane appear as straight lines.

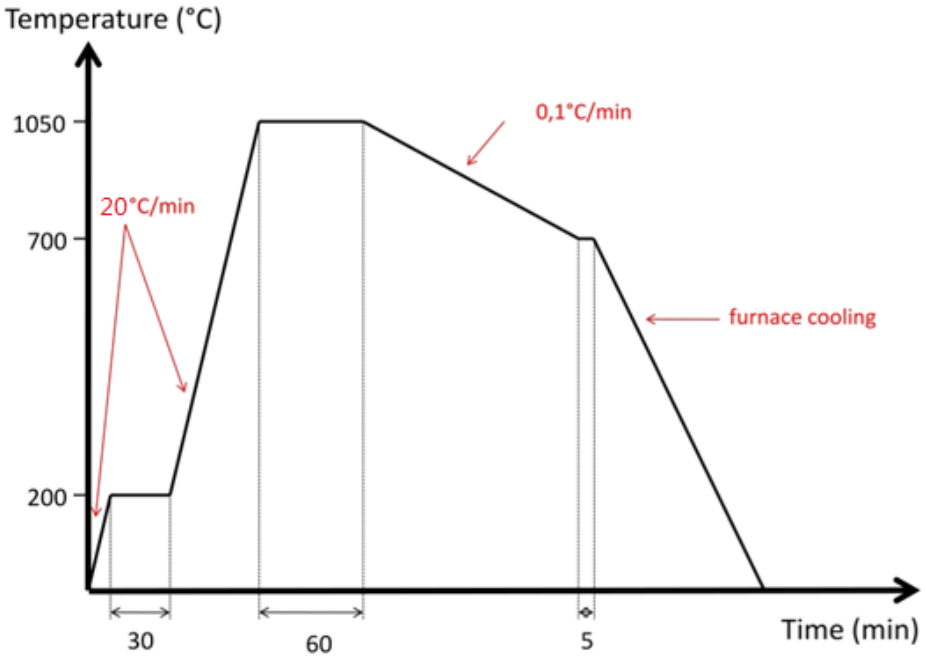

Figure 4-1 The heat treatment procedure of the Ti-6Al-4V samples prior to the plastic deformation.

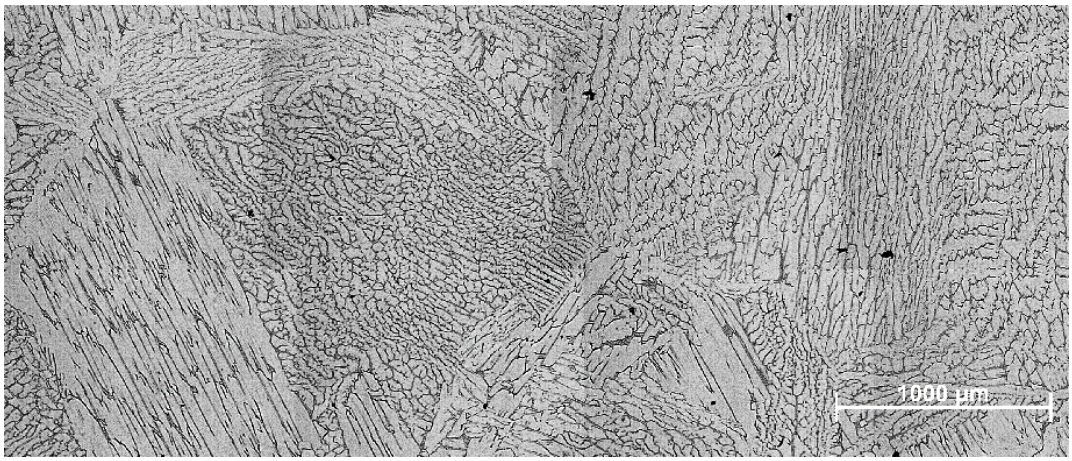

Figure 4-2 Optical micrograph showing the typical microstructure of the heat-treated Ti-6Al-4V.

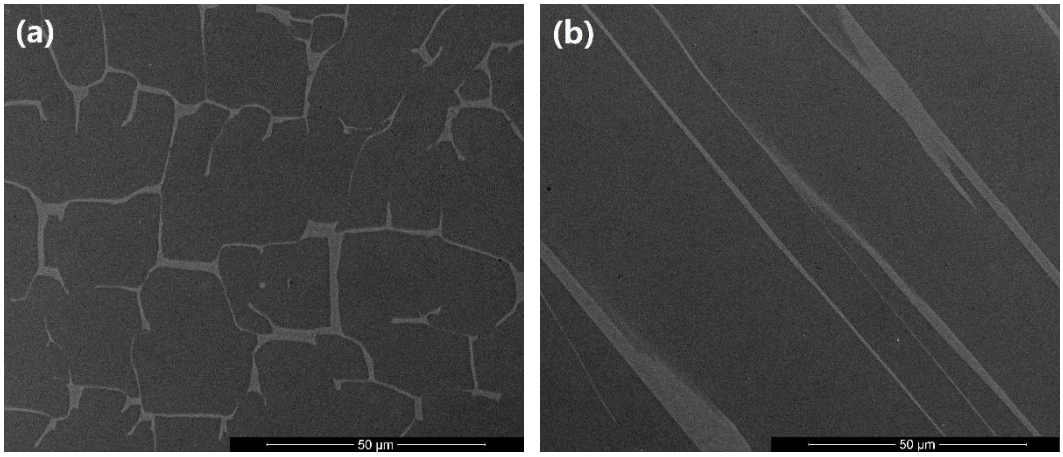

Figure 4-3 SEM images showing the typical microstructure of the Ti-6Al-4V after the heat treatment. (a) SEM image of the colony with [1$\bar{1}$00] normal to the paper plane, (b) SEM image of the colony with [000$\bar{1}$] normal to the paper plane.

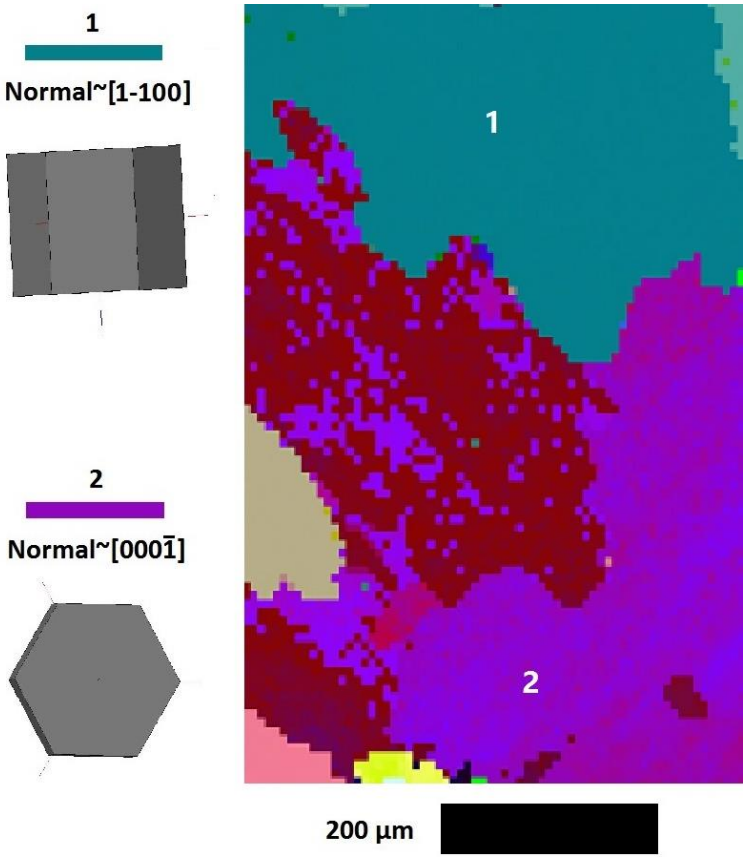

Figure 4-4 EBSD map showing the crystallographic orientation of colonies for micro-pillar fabrication. Colony 1 has its normal direction close to [1$\bar{1}$00] and colony 2 has its normal direction close to [000$\bar{1}$].

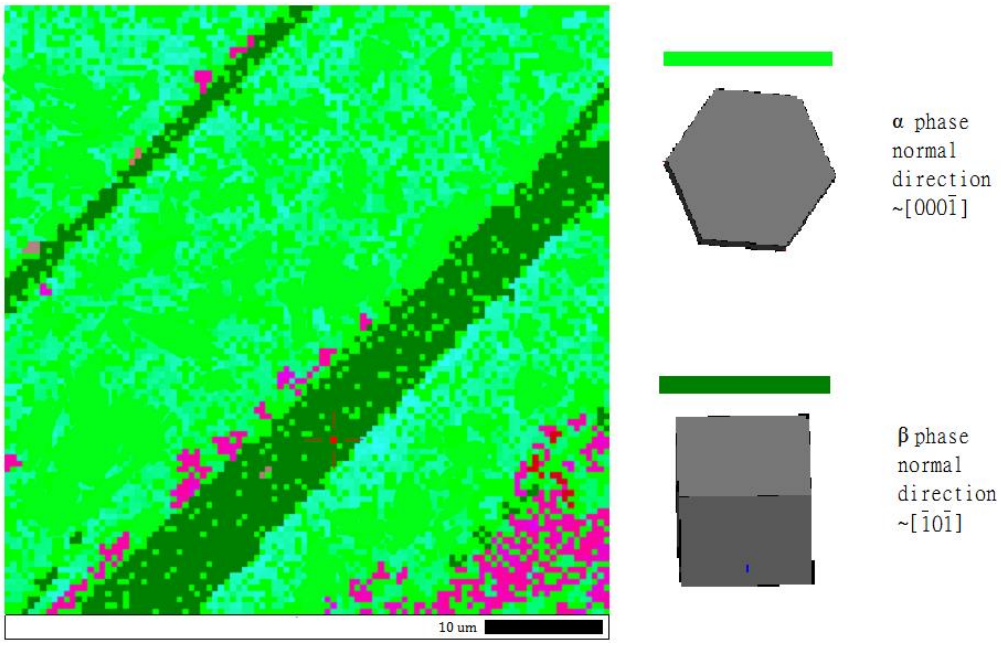

Figure 4-5 The orientation relationship between the α and β phases in a colony are $(000\bar{1})_{\alpha}$ // $(\bar{1}0\bar{1})_{\beta}$, $[2\bar{1}\bar{1}0]_{\alpha}$ // $[11\bar{1}]_{\beta}$

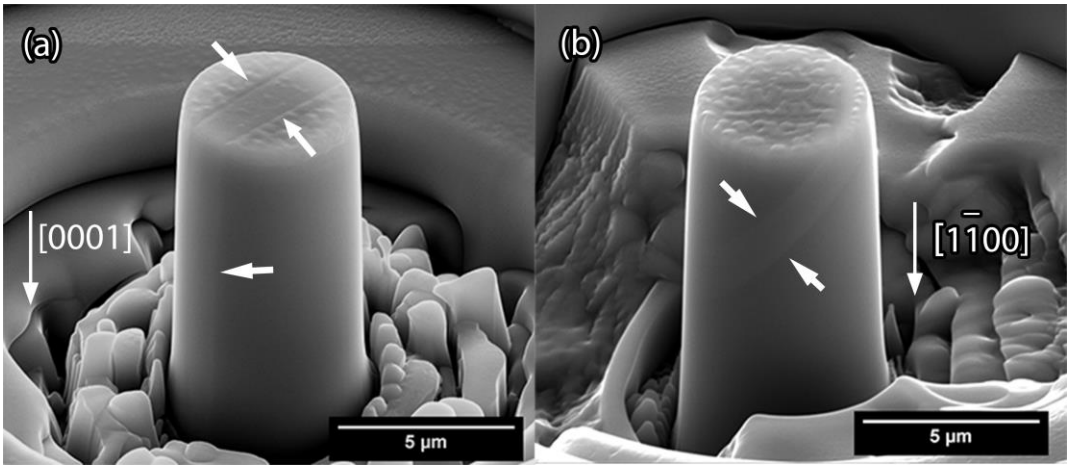

Figure 4-6 (a) Micro-pillar prepared in the colony with a [0001] axis direction. It has β go through the micro-pillar straight from top to bottom. (b) Micro-pillar prepared in the colony with $[01\bar{1}0]$ *axis direction has β go across the micro-pillar at an angle.*

Figure 4-7 The load-displacement curves of indentation test on the ion-irradiated area and the ion-free area.

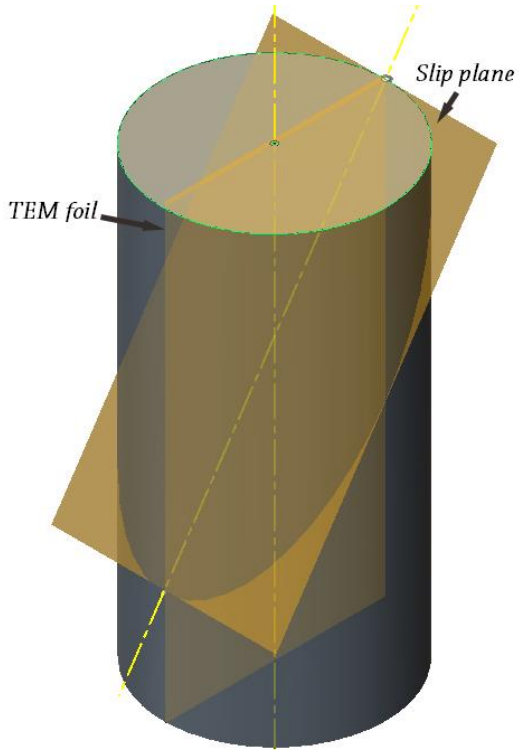

Figure 4-8 Sketch of the orientation relationship between the extracted TEM foil plane and slip plane in the micro-pillar.

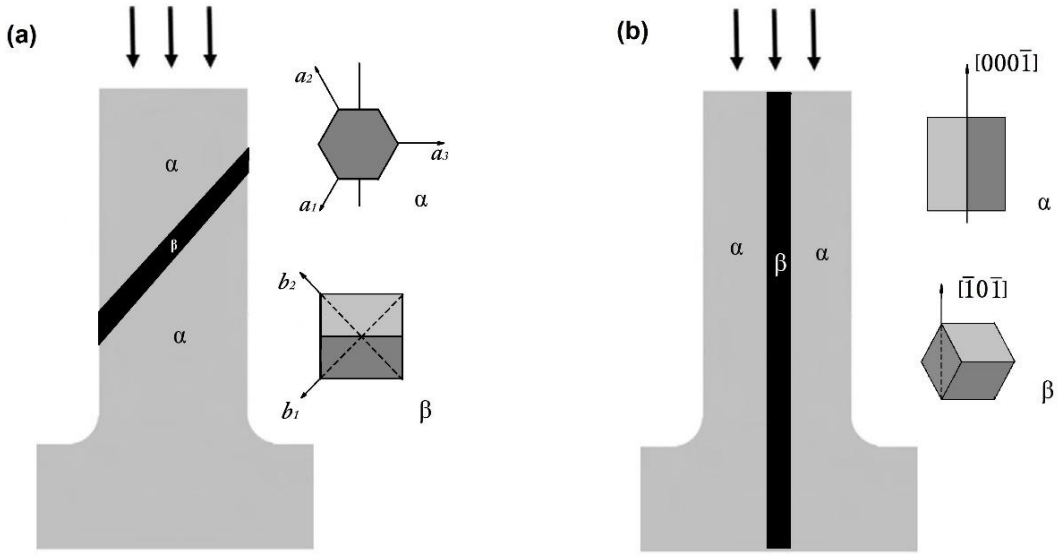

Figure 4-9 Sketch of the TEM samples and α/β crystal orientations in different colonies (a) Loading direction [1$\bar{1}$00]$_\alpha$// [10$\bar{1}$]$_\beta$, foil normal direction [000$\bar{1}$]$_\alpha$// [$\bar{1}$0$\bar{1}$]$_\beta$, (b) Loading direction [0001]$_\alpha$// [101]$_\beta$, foil normal direction [2$\bar{1}\bar{1}$0]$_\alpha$// [11$\bar{1}$]$_\beta$

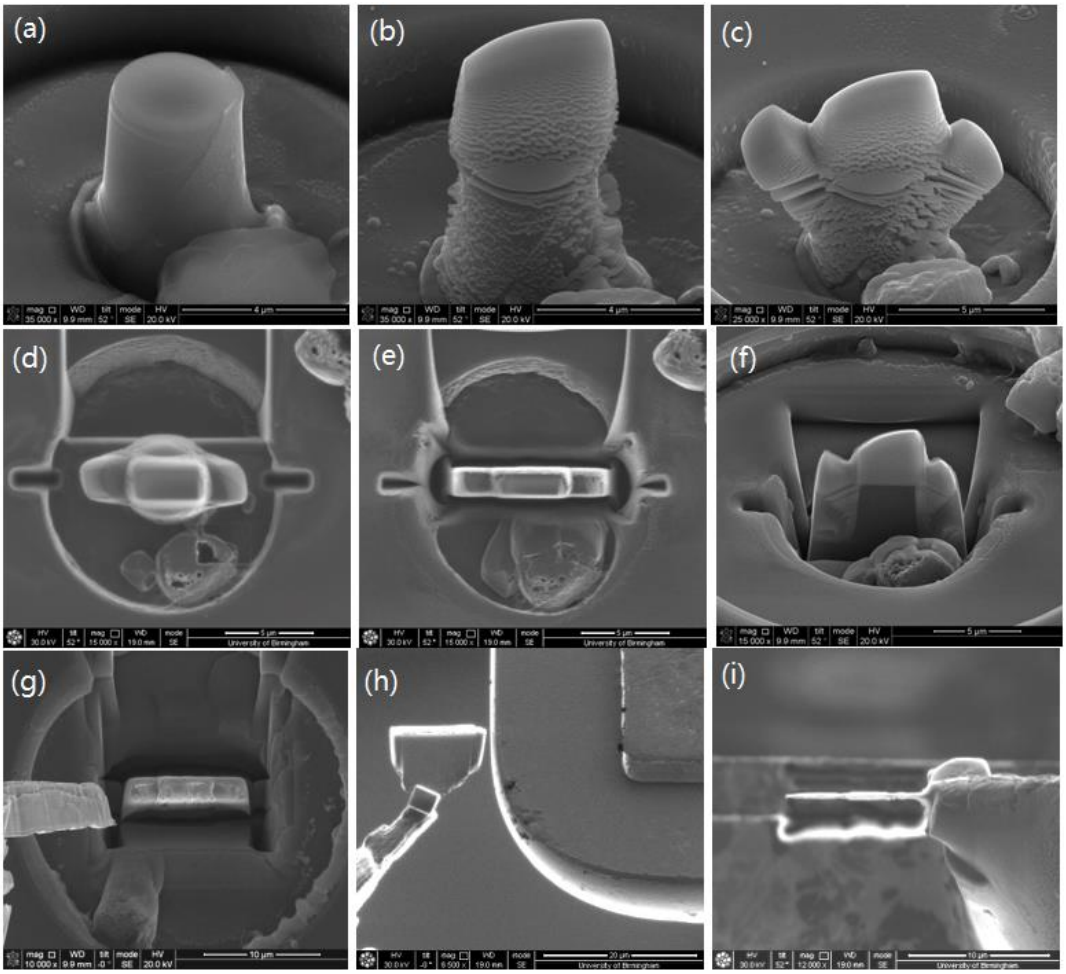

Figure 4-10 The secondary electron or ion beam images showing the process of producing a TEM foils from a compressed 3μm diameter micro-pillar.

Table 4.1 Composition of Ti-6Al-4V used in this project

Component	**Ti**	**Al**	**V**
wt.%	90.14	5.81	4.05

Table 4.2 Schmid factor for possible slip systems in h.c.p crystal structure in Ti-6Al-4V with the loading directions along [0001], [1$\bar{1}$00] and [11$\bar{2}$0].The highest Schmid factor is in bold.

Slip system	Slip direction	Slip plane	Schmid factor in different loading direction		
			[0001]	[1$\bar{1}$00]	[11$\bar{2}$0]
Basal <***a***> slips	[11$\bar{2}$0]	(0001)	0	0	0
	[1$\bar{2}$10]	(0001)	0	0	0
	[$\bar{2}$110]	(0001)	0	0	0
Prismatic <***a***> slips	[11$\bar{2}$0]	(1$\bar{1}$00)	0	0	0
	[1$\bar{2}$10]	(10$\bar{1}$0)	0	**0.433**	0.433
	[$\bar{2}$110]	(01$\bar{1}$0)	0	**0.433**	0.433
Pyramidal <***a***> slips	[11$\bar{2}$0]	(1$\bar{1}$01)	0	0	0
	[11$\bar{2}$0]	($\bar{1}$101)	0	0	0
	[1$\bar{2}$10]	(10$\bar{1}$1)	0	0.380	0.380
	[1$\bar{2}$10]	($\bar{1}$011)	0	0.380	0.380
	[$\bar{2}$110]	(01$\bar{1}$1)	0	0.380	0.380
	[$\bar{2}$110]	(0$\bar{1}$11)	0	0.380	0.380
1st order pyramidal <***c+a***> slips	[$\bar{1}\bar{1}$23]	(10$\bar{1}$1)	0.405	0	0.405
	[$\bar{1}\bar{1}$23]	(01$\bar{1}$1)	0.405	0	0.405
	[11$\bar{2}$3]	($\bar{1}$011)	0.405	0	0.405
	[11$\bar{2}$3]	(0$\bar{1}$11)	0.405	0	0.405
	[$\bar{1}$2$\bar{1}$3]	(0$\bar{1}$11)	0.405	0.405	0.202
	[$\bar{1}$2$\bar{1}$3]	(1$\bar{1}$01)	0.405	0.202	0
	[1$\bar{2}$13]	($\bar{1}$101)	0.405	0.202	0
	[1$\bar{2}$13]	(01$\bar{1}$1)	0.405	0.405	0.202
	[2$\bar{1}\bar{1}$3]	($\bar{1}$101)	0.405	0.202	0
	[2$\bar{1}\bar{1}$3]	($\bar{1}$011)	0.405	0.405	0.202
	[$\bar{2}$113]	(1$\bar{1}$01)	0.405	0.202	0
	[$\bar{2}$113]	(10$\bar{1}$1)	0.405	0.405	0.202
2nd order pyramidal <***c+a***> slips	[11$\bar{2}$3]	($\bar{1}\bar{1}$22)	**0.451**	0	**0.451**
	[$\bar{1}\bar{1}$23]	(11$\bar{2}$2)	**0.451**	0	**0.451**
	[1$\bar{2}$13]	($\bar{1}$2$\bar{1}$2)	**0.451**	0.338	0.113
	[$\bar{1}$2$\bar{1}$3]	(1$\bar{2}$12)	**0.451**	0.338	0.113
	[$\bar{2}$113]	(2$\bar{1}\bar{1}$2)	**0.451**	0.338	0.113
	[2$\bar{1}\bar{1}$3]	($\bar{2}$112)	**0.451**	0.338	0.113

Table 4.3 Typical slip systems in b.c.c crystal structure. The highest Schmid factor is in bold.

Slip System Number	Slip Direction	Slip Plane	Schmid factor along different loading directions	
			[101]	[10$\bar{1}$]
1	[1 $\bar{1}$ 1]	(0 1 1)	0.408	0
2	[1 1 $\bar{1}$]	(0 1 1)	0	0.408
3	[$\bar{1}$ 1 1]	(1 0 1)	0	0
4	[1 1 $\bar{1}$]	(1 0 1)	0	0
5	[$\bar{1}$ 1 1]	(1 1 0)	0	0.408
6	[1 $\bar{1}$ 1]	(1 1 0)	0.408	0
7	[1 1 1]	(0 $\bar{1}$ 1)	0.408	0
8	[$\bar{1}$ 1 1]	(0 $\bar{1}$ 1)	0	0.408
9	[1 1 1]	(1 0 $\bar{1}$)	0	0
10	[1 $\bar{1}$ 1]	(1 0 $\bar{1}$)	0	0
11	[1 1 1]	($\bar{1}$ 1 0)	0.408	0
12	[1 1 $\bar{1}$]	($\bar{1}$ 1 0)	0	0.408
13	[1 1 $\bar{1}$]	(1 1 2)	0	0.236
14	[1 $\bar{1}$ 1]	($\bar{1}$ 1 2)	0.236	0
15	[$\bar{1}$ 1 1]	(1 $\bar{1}$ 2)	0	0.236
16	[1 1 1]	(1 1 $\bar{2}$)	0.236	0
17	[1 $\bar{1}$ 1]	(1 2 1)	**0.471**	0
18	[1 1 $\bar{1}$]	($\bar{1}$ 2 1)	0	**0.471**
19	[1 1 1]	(1 $\bar{2}$ 1)	**0.471**	0
20	[$\bar{1}$ 1 1]	(1 2 $\bar{1}$)	0	**0.471**
21	[$\bar{1}$ 1 1]	(2 1 1)	0	0.236
22	[1 1 1]	($\bar{2}$ 1 1)	0.236	0
23	[1 1 $\bar{1}$]	(2 $\bar{1}$ 1)	0	0.236
24	[1 $\bar{1}$ 1]	(2 1 $\bar{1}$)	0.236	0
25	[1 1 $\bar{1}$]	(1 2 3)	0	0.309
26	[1 $\bar{1}$ 1]	($\bar{1}$ 2 3)	0.309	0
27	[$\bar{1}$ 1 1]	(1 $\bar{2}$ 3)	0	0.309
28	[1 1 1]	(1 2 $\bar{3}$)	0.309	0
29	[$\bar{1}$ 1 1]	(3 1 2)	0	0.154
30	[1 1 1]	($\bar{3}$ 1 2)	0.154	0
31	[1 1 $\bar{1}$]	(3 $\bar{1}$ 2)	0	0.154
32	[1 $\bar{1}$ 1]	(3 1 $\bar{2}$)	0.154	0

(Continued Table 4.3)

Slip System Number	Slip Direction	Slip Plane	Schmid factor along different loading directions	
			[101]	[10$\bar{1}$]
33	[1 $\bar{1}$ 1]	(2 3 1)	0.463	0
34	[1 1 $\bar{1}$]	($\bar{2}$ 3 1)	0	0.463
35	[1 1 1]	(2 $\bar{3}$ 1)	0.463	0
36	[$\bar{1}$ 1 1]	(2 3 $\bar{1}$)	0	0.463
37	[1 $\bar{1}$ 1]	(1 3 2)	0.463	0
38	[1 1 $\bar{1}$]	($\bar{1}$ 3 2)	0	0.463
39	[1 1 1]	(1 $\bar{3}$ 2)	0.463	0
40	[$\bar{1}$ 1 1]	(1 3 $\bar{2}$)	0	0.463
41	[1 1 $\bar{1}$]	(2 1 3)	0	0.154
42	[1 $\bar{1}$ 1]	($\bar{2}$ 1 3)	0.154	0
43	[$\bar{1}$ 1 1]	(2 $\bar{1}$ 3)	0	0.154
44	[1 1 1]	(2 1 $\bar{3}$)	0.154	0
45	[$\bar{1}$ 1 1]	(3 2 1)	0	0.309
46	[1 1 1]	($\bar{3}$ 2 1)	0.309	0
47	[1 1 $\bar{1}$]	(3 $\bar{2}$ 1)	0	0.309
48	[1 $\bar{1}$ 1]	(3 2 $\bar{1}$)	0.309	0

Table 4.4 Experiment conditions used for the micro-pillars preparation using FIB

Step	**Voltage**	**Current (depending on the pillar diameter)**	**Type of Milling Box**
Outer trench	30 KeV	5 - 30 nA	Circle
Inner trench	30 KeV	1 - 10 nA	Circle
Cleaning	30 KeV	30 pA -1 nA	Circle

Table 4.5. The dimensions and compressed nominal strains of the micro-pillars using in this study.

No.	Axis direction	Phases	Top diameter (μm)	Bottom diameter (μm)	Height (μm)	Taper angle (°)	Nominal Strain (%)
1	~[1$\bar{1}$00] Euler angles (2.8°, 90°, 33.5°)	α	5.05	5.78	11.63	1.80	10
2			5.01	5.64	11.78	1.53	5
3			2.76	3.18	6.03	2.00	5
4			2.31	2.70	4.88	2.29	10
5			1.13	1.32	2.23	2.44	5
6			1.24	1.34	2.18	1.31	2
7			1.22	1.39	2.32	2.10	5
8			0.77	0.92	1.61	2.67	5
9			0.77	0.90	1.60	2.33	3
10		α+β	5.55	6.29	11.81	1.80	3
11			3.35	3.99	7.80	2.35	5
12			2.57	2.96	5.42	2.06	5
13			1.54	1.77	3.11	2.12	5
14			0.72	0.87	1.40	3.07	5
15	~[0001] Euler angles (102.0°, 2.4°, 46.0°)	α	4.95	5.54	10.16	1.66	5
16			4.91	5.49	10.08	1.65	10
17			3.03	3.76	7.47	2.80	10
18			2.94	3.85	6.48	4.02	5
19			2.97	3.85	6.55	3.85	10
20			3.09	3.73	6.43	2.85	10
21			2.84	3.12	6.13	1.31	8
22			1.03	1.18	2.31	1.86	5
23			1.05	1.25	2.10	2.73	8
24			1.15	1.36	2.36	2.55	10
25			0.61	0.71	1.25	2.29	5
26			0.83	1.04	1.75	3.44	10
27		α+β	4.86	5.78	10.07	2.62	10
28			4.75	5.51	10.05	2.17	5
29			5.08	5.38	10.35	0.83	8
30			4.78	5.56	10.66	2.10	10
31			5.01	5.63	10.74	1.65	8
32			2.93	3.69	6.42	3.39	5
33			3.09	3.85	6.40	3.40	8
34			3.03	3.67	6.73	2.72	10
35			2.94	3.59	6.64	2.80	10

(Continued Table 4.5)

No.	Axis direction	Phases	Top diameter (μm)	Bottom diameter (μm)	Height (μm)	Taper angle (°)	Nominal Strain (%)
36	~[0001] Euler angles (102.0°, 2.4°, 46.0°)	α+β	2.89	3.68	6.56	3.45	10
37			2.10	2.47	4.08	2.60	10
38			2.01	2.21	4.02	1.43	5
39			1.10	1.58	2.66	5.17	10
40			1.18	1.55	2.30	4.61	10
41			1.06	1.19	2.03	1.83	5
42			1.10	1.29	2.33	2.34	10
43			0.99	1.25	2.37	3.14	0
44			1.15	1.34	2.49	2.19	15
45			1.29	1.48	2.67	2.04	10
46		β	2.84	3.43	6.60	2.56	10
47			3.02	3.73	6.45	3.15	10
48			2.98	3.71	6.76	3.09	10
49			3.13	3.55	6.07	1.98	5
50			4.98	5.71	11.10	1.88	5

Table 4.6 The Young's modulus and hardness of undamaged and irradiation damaged α phase

	E (MPa)		**Hardness (GPa)**	
	Average	SD	Average	SD
Ion-free area	135.8	4.8	5.4	0.1
Ion-irradiated area	135.2	4.9	5.9	0.1

Table 4.7 Experiment conditions used for the TEM sample preparation using FIB

Step	Type of Milling Box	Voltage	Current	Tilt Angle
Pt coating on top	Rectangle	30 KeV	0.1nA	52°
Pt coating on side	Rectangle	30 KeV	0.1nA	0°
Trench milling	Regular cross-section	30 KeV	15nA	52°
Bulk milling	Rectangle	30 KeV	3nA	52°
Omniprobe/Cu grid welding	Rectangle	30 KeV	0.1nA	0°
Bottom cutting	Rectangle	30 KeV	1nA	0°
Omniprobe cutting	Rectangle	30 KeV	3nA	0°
Thinning	Rectangle	30 KeV	1nA-0.1nA	52°±1.5°
Cleanning	Rectangle	5 KeV	48pA	52°±6°

Chapter 5 Compression of micro-pillars

5.1 Loading direction along $[1\bar{1}00]_{\alpha}$ // $[10\bar{1}]_{\beta}$

5.1.1 α single phase micro-pillars

Figure 5-1 shows the stress-strain curves obtained from the compression of the micro-pillars containing only the α phase along $[1\bar{1}00]$ loading direction. The micro-pillar diameters range from 500 nm to 5 μm. All curves have the similar smooth stress-strain curves (except the curve obtained from the 3 μm pillar which deviates from the rest) before the yielding. The yielding is well defined in all cases and the yield stresses determined are listed in Table 5.1. The yield stress increases from 775 MPa to 1125 MPa when the pillar size decreases from 5 μm to 500 nm. When the micro-pillars are loaded along $[1\bar{1}00]$, $[2\bar{1}\bar{1}0](0\bar{1}10)$ and $[1\bar{2}10](10\bar{1}0)$ are the slip systems associated with the highest Schmid factor of 0.43. Assuming this is the case, the CRSS for the prismatic <***a***> slip increases from 336 MPa to 487 MPa for micro-pillars with 5 μm to 500 nm diameter. Beyond the yielding, the stress-strain curve obtained from the 5 μm diameter micro-pillar (red curve in Figure 5.1) is smoother than those obtained from the smaller pillars. The curve obtained from the micro-pillar of 500 nm diameter (black curve in Figure 5.1) is characterized by the small stress drops (serration) beyond the yielding. Furthermore, the 5 μm diameter micro-pillar shows an obvious stable work hardening behaviour during the compression with the flow stress increases gradually from 780 MPa to 912 MPa. The other three smaller pillar samples all show a flow stress drop after

the yielding with no noticeable work hardening observed on the 500-nm pillar. This is consistent with the literature on the micro-pillar compression [90].

The sample size effect on elastic modulus has mostly been reported in nanowires [107-110], due to the surface-stress-induced elasticity [110] rather than in micro-pillars. Modelling results indicated that the sample size effect only becomes distinct when the sample diameter is less than 500 nm or smaller (depending on the materials and their orientations [110]). The 128 GPa-140 GPa of the elastic modulus *E* for different sizes measured in Table 5.1 is higher than the 104 GPa reported in CP-Ti [102]. It could be caused by the fact that the α phase has slightly different composition from the CP-Ti.

Figure 5-2 is a SEM image of the micro-pillars containing the α phase only after the compression along $[1\bar{1}00]$. With 4% strain, only one set of slip traces can be observed as indicated by the arrow. The slip traces meet the top surface of the pillar at an angle of about 60°. According to the EBSD results, in the SEM images, the horizontal direction is $[\bar{1}\bar{1}20]$ and the pillar axis direction is $[1\bar{1}00]$. Along this loading direction, the <***a***> prismatic slip system (i.e. with a $\frac{1}{3}[2\bar{1}\bar{1}0]$ Burgers vector on $(0\bar{1}10)$ slip plane and Schmid factor of 0.433) is likely to be activated. The other micro-pillars in this colony have similar morphology after compression.

5.1.2 Micro-pillars containing a β layer through α phase

Figure 5-3 shows the stress-strain curves obtained from the compression of micro-pillars of 5 μm to 1 μm diameter, containing α and β phases with the loading direction along $[1\bar{1}00]_{\alpha}$ // $[10\bar{1}]_{\beta}$. The yield stress becomes larger when the pillar

size gets smaller. After yielding, softening occurred on the larger size samples but hardening on the small samples. The flow stress serration beyond the yielding increases with the decreasing micro-pillars size. Compared with micro-pillars in section 5.1.1, the yield stress and CRSS for the prismatic slip in α phase decreased when the β layer is included in the micro-pillars (Table 5.2 vs. Table 5.1). The elastic modulus measured is also lower with the introduction of the β phase in the micro-pillars [111]. As shown in Table 5.2, the elastic moduli were ranging from 108 GPa -118 GPa. These values are in the range between the elastic moduli of α phase and β phase and they are dependent on the α/β volume fractions ratio. There is no any sample size effect trend as well.

Figure 5-4 shows SEM images of a 5 μm diameter micro-pillar containing β fillet through the α phase compressed along $[1\bar{1}00]_\alpha$ // $[10\bar{1}]_\beta$ colony by 4% strain. In Figure 5-4 (a) the 4% micro-pillar shows one set of slip trace which is 60° from the pillar top surface, but different from the multiple slip traces in the α only micro-pillar, there is only one observable slip trace through the micro-pillar cutting through the β phase. Figure 5-4 (b) shows there is an angle of 15° between the slip plane and the interface between the α and β. The angle between the $\boldsymbol{a}_1$ $(0\bar{1}10)$ slip plane and the broad face is close to 15°. Therefore, the activated slip system is probably the $\boldsymbol{a}_1$ prismatic slip.

5.2 Loading direction along $[0001]_\alpha$ // $[101]_\beta$

5.2.1 α single phase micro-pillars

Figure 5-5 shows the stress-strain curves obtained from the α micro-pillars when

loaded along the [0001] direction. After the micro-pillars reach the yield point, serration on the stress can be observed. In the curves obtained from the 3 μm micro-pillars, there is a large stress drop at about 7% strain. When micro-pillar size decreases, there is no such shearing and large stress drop observed. The yield stresses recorded are listed in Table 5.3. The yield stress was increased from 2298 MPa to 2963 MPa with the micro-pillars diameters reducing from 5 μm to 1 μm. However, the 0.5 diameter μm micro-pillar has a drop of yield stress to 2544 MPa. This could be caused by the uncertainty of the contact between the punch and the top surface of the micro-pillar at the beginning of compression.The elastic moduli measured from the linear loading parts of the compression stress-strain curves in Table 5.3 are of 173 GPa -148 GPa when the micro-pillar diameters reduced from 5 μm to 0.5 μm, which is a bit higher than the 146 GPa reported from CP-Ti along [0001] direction [102].

The SEM images in Figure 5-6 show the morphology of a 3 μm diameter micro-pillars containing the α phase after compression to different strains. There is no observable shearing of micro-pillar at 2% strain, with only some fine slip traces appeared on the side surface of α micro-pillars. A slip trace moving from the top surface and through the micro-pillar appeared on the side surface of micro-pillars after 5% strain (Figure 5-6 (b)), and a large shearing of the top part of micro-pillar can be observed at 7% strain (Figure 5-6 (c)). There is only one slip band with a large step on the side surface to accommodate the deformation instead of multiple slip bands, corresponding to the large stress drop in Figure 5-5. In the SEM images, the angles between the top surface of micro-pillar and the slip plane were ~30° for

all pillars. This angle is close to the angle between (0001) and pyramidal planes. Therefore, the slip system is likely to be <***c+a***> slip rather than <***a***> slip

5.2.2 Micro-pillars containing a β layer through the α phase

Figure 5-7 shows the stress-strain curves obtained from the compression of micro-pillars containing α and β phases along [0001] loading direction. Compared with the curves in Figure 5-5, the curves in Figure 5-7 are smoother and there is no large stress drop in all curves. It was also reflected in the SEM images in Figure 5-8, no large shear observed in the micro-pillars containing β fillet.

The SEM images in Figure 5-8 show the morphology of a 3 μm diameter micro-pillars containing α and β phases after compression to different strains along [0001]. Images from top to bottom show the samples with 2%, 5%, and 7% strain. Compared with the micro-pillars without a β phase in Figure 5-6, there is no apparent difference of micro-pillar at 2% strain. However, the micro-pillars containing both α and β phases show no observable slip trace until 7% strain. Another difference in the series of micro-pillars containing a β layer is that the plastic deformation no longer appeared in the form of shearing with clear slip traces. Instead, a swell on the side wall of micro-pillars accommodated the deformation.

5.2.3 Micro-pillars containing large volume fraction of β phase

The results above show that the strength changes after introducing the β phase into micro-pillars. To understand the strength of the β phase, micro-pillars containing a large volume fraction of β phase were prepared in the $[0001]_{\alpha}$ // $[101]_{\beta}$ colony. The compression results of the micro-pillars with 3 μm diameter along $[0001]_{\alpha}$ // [101]

β loading direction containing large volume fraction of β are put together with stress-strain curves of other micro-pillars of 3 μm diameter in the same colony, as shown in Figure 5-9. The strength of micro-pillars decreased with the increasing volume fraction of β phase. The stress obtained from the micro-pillars containing a large volume fraction of β phase can be regarded as the strength of β phase as there is no observable deformation in the α phase. However, compared with the micro-pillars containing only the α phase, the micro-pillars containing β fillet between two α, the stress decreased because the softer β phase shared the cross-section area with the stronger α phase. For example, the yield stress of the 3 μm diameter α phase micro-pillar is 2878 MPa. The yield stress of the 3 μm diameter micro-pillar containing 0.7 μm thickness β phase decreased to 2199 MPa. As the measured yield stress of micro-pillars contains higher volume fraction of β in Table 5.5 shows, the β phase yield strength is 615 MPa along this orientation in the 3 μm size.

In Figure 5-9, the three different types of micro-pillars were compressed to three distinctively different sets of stress-strain curves. There are 3 or 4 repeated tests under each test condition and they show good reproducibility.

The SEM images of a micro-pillars with a large volume fraction of β phase are shown in Figure 5-10. The top half is the β phase and the bottom half the α phase. Figure 5-10 (a) shows the micro-pillar before compression and Figure 5-10 (b) shows the micro-pillar after 8% compression. It is shown clearly in Figure 5-10 (b) that the top β phase was deformed heavily, but α phase at the bottom of the micro-pillar had no observable deformation.

Another micro-pillar with a different shape of β phase, the half β phase at the top

left and half α phase at the bottom right, was prepared in the same colony as shown in Figure 5-11 (a). After applying 8% plastic strain shown in Figure 5-11 (b), the β phase on the top of the micro-pillar has been deformed heavily with two sets of visible slip bands while no observable deformation can be seen in the α phase.

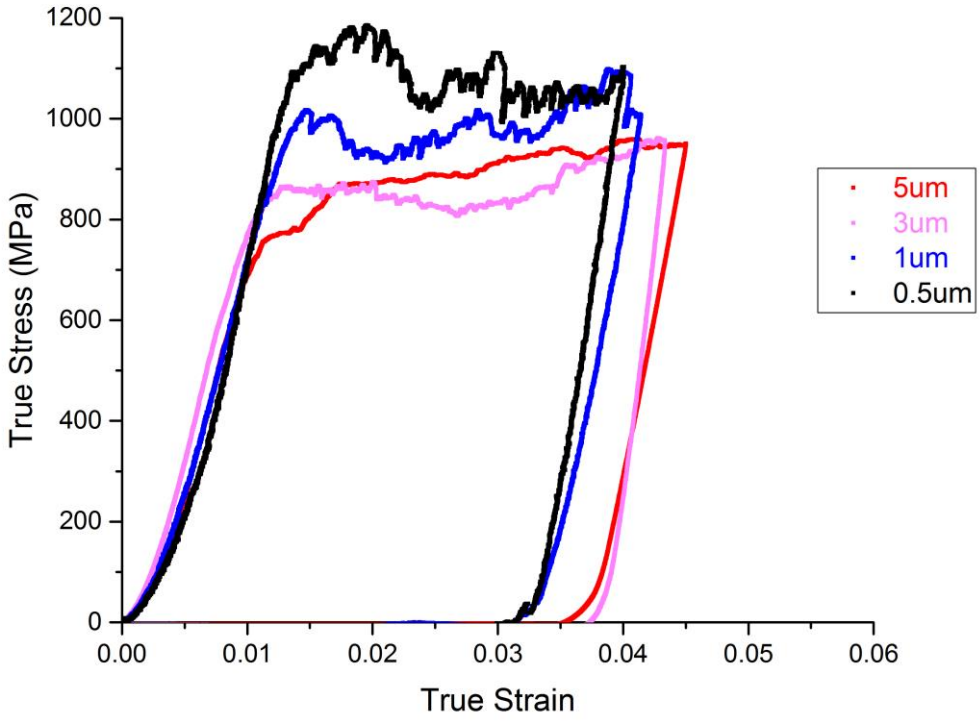

Figure 5-1 Stress-strain curves obtained from the compressed micro-pillars of different diameters containing α only along [1$\bar{1}$00] loading direction (5μm: pillar #1, 3μm: pillar #3, 1μm: pillar #5, 0.5μm: pillar #8). There are increasing yield stresses with decreasing diameter, but the work hardening rates decreased with decreasing diameters.

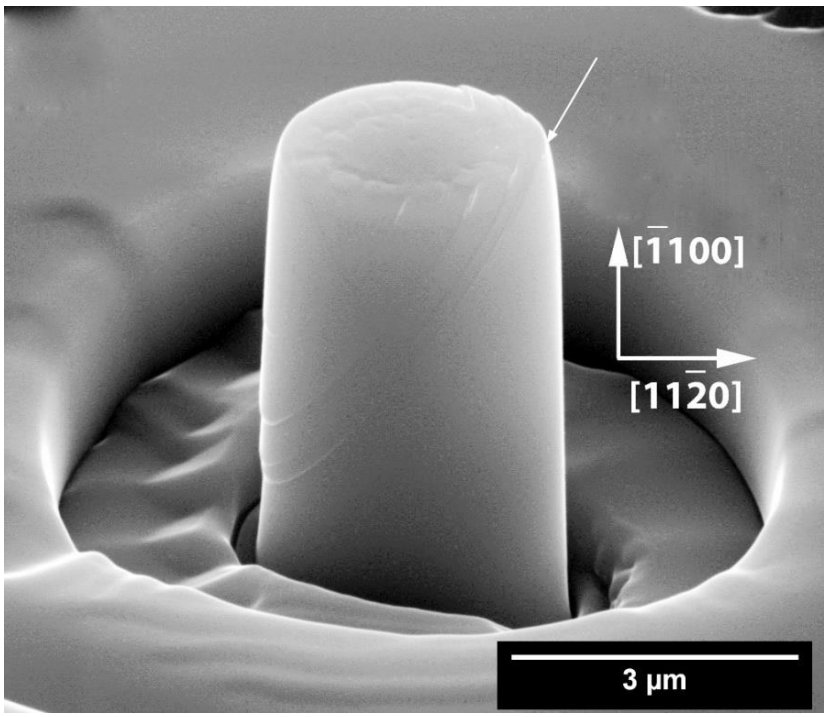

Figure 5-2 SEM images of 3 μm diameter micro-pillars containing α phase after 4% strain. The typical morphology of micro-pillars compressed in [1$\bar{1}$00] colony is one set of slip traces can be observed, as indicated by the arrow.

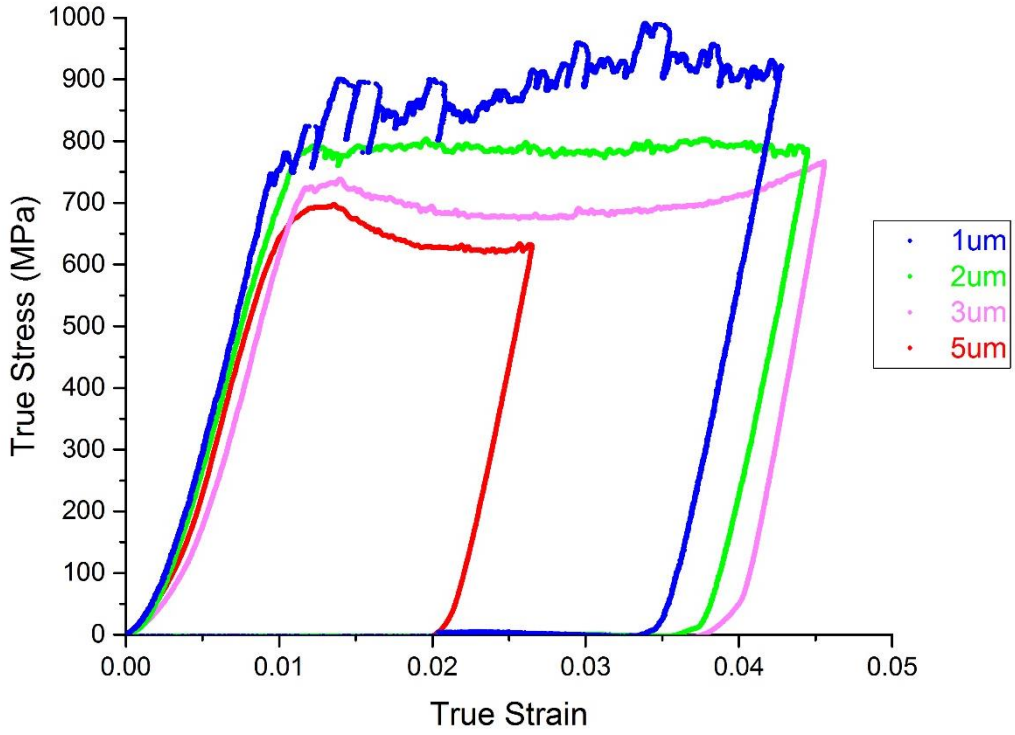

Figure 5-3 Stress-strain curves of the 2% – 4% compressed micro-pillars of different diameters containing β fillet between two α along $[1\bar{1}00]_{\alpha}$// $[10\bar{1}]_{\beta}$ loading direction (5μm: pillar #10, 3μm: pillar #11, 2μm: pillar #12, 1μm: pillar #13). The yield stress, work hardening rate, flow stress serration increased with micro-pillar size decreasing.

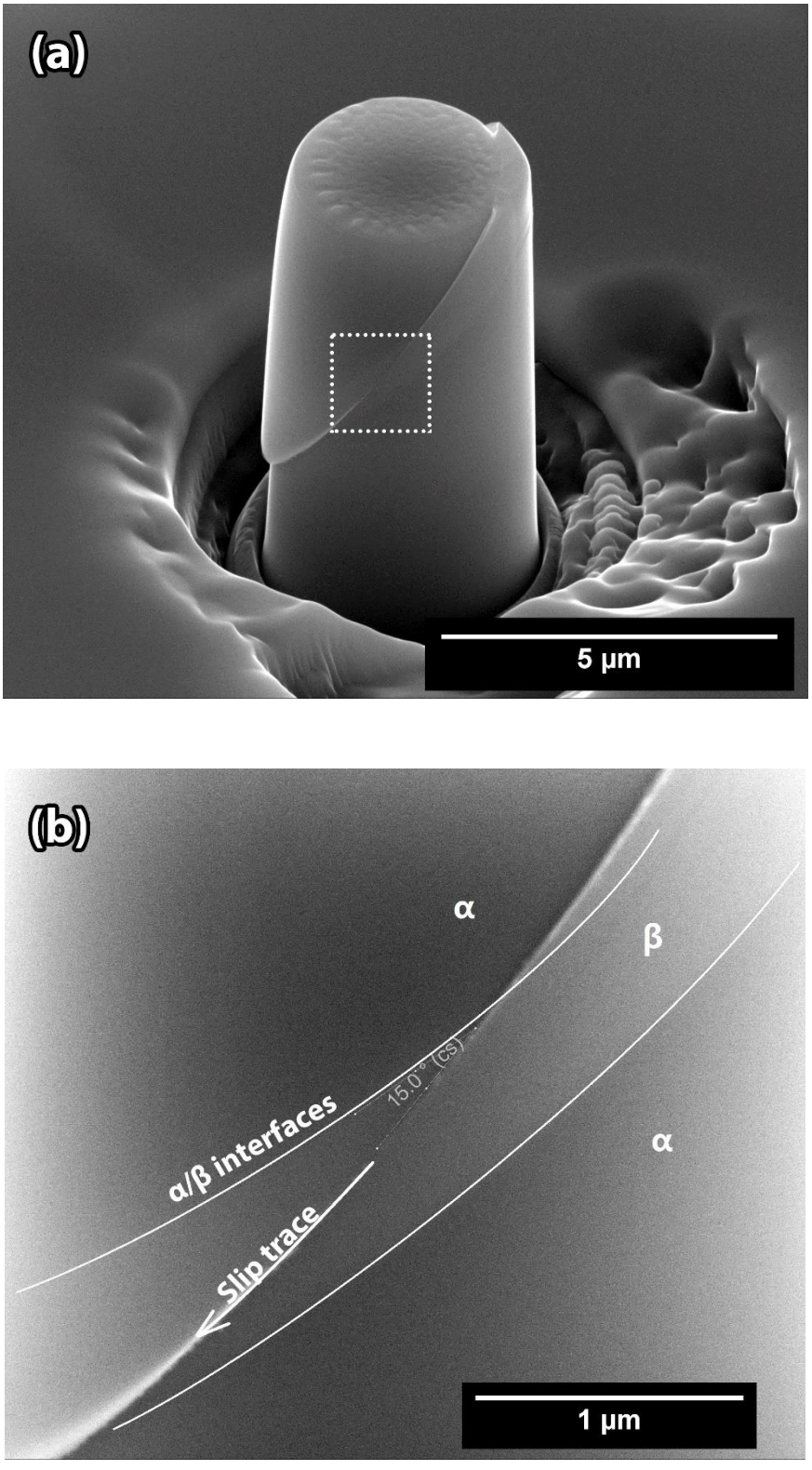

Figure 5-4 (a) SEM images of 3µm diameter micro-pillar containing β fillet through α phase after 4% strain in $[1\bar{1}00]_{\alpha}$ *//* $[10\bar{1}]_{\beta}$ *loading direction. (b) The high magnification in the region marked in the image (a). It shows 15° between the slip plane and the α/β interfaces. The other micro-pillars compressed in* $[1\bar{1}00]$ *have similar morphology.*

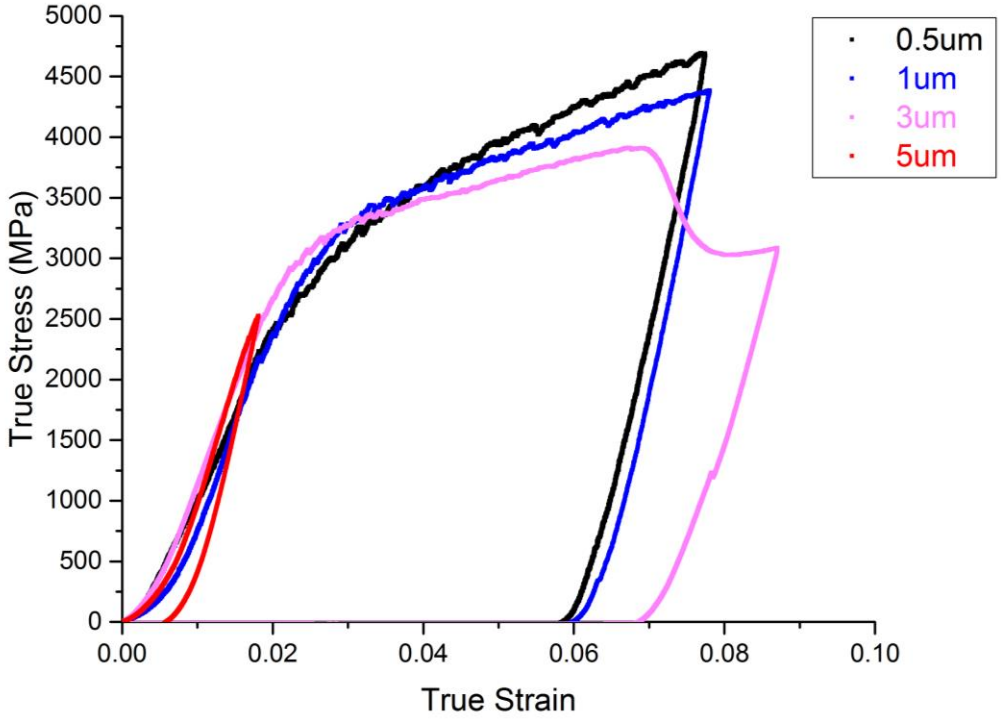

Figure 5-5 Stress-strain curves obtained from the compression of micro-pillars of different diameters containing only α phase along [0001] (5μm: pillar #15, 3μm: pillar #17, 1μm: pillar #24, 0.5μm: pillar #26). There is not much difference in the yield stresses between different sizes, but the work hardening rate increased with micro-pillar size decreasing. (The 5μm micro-pillar reached the max force of the indenter after yielding)

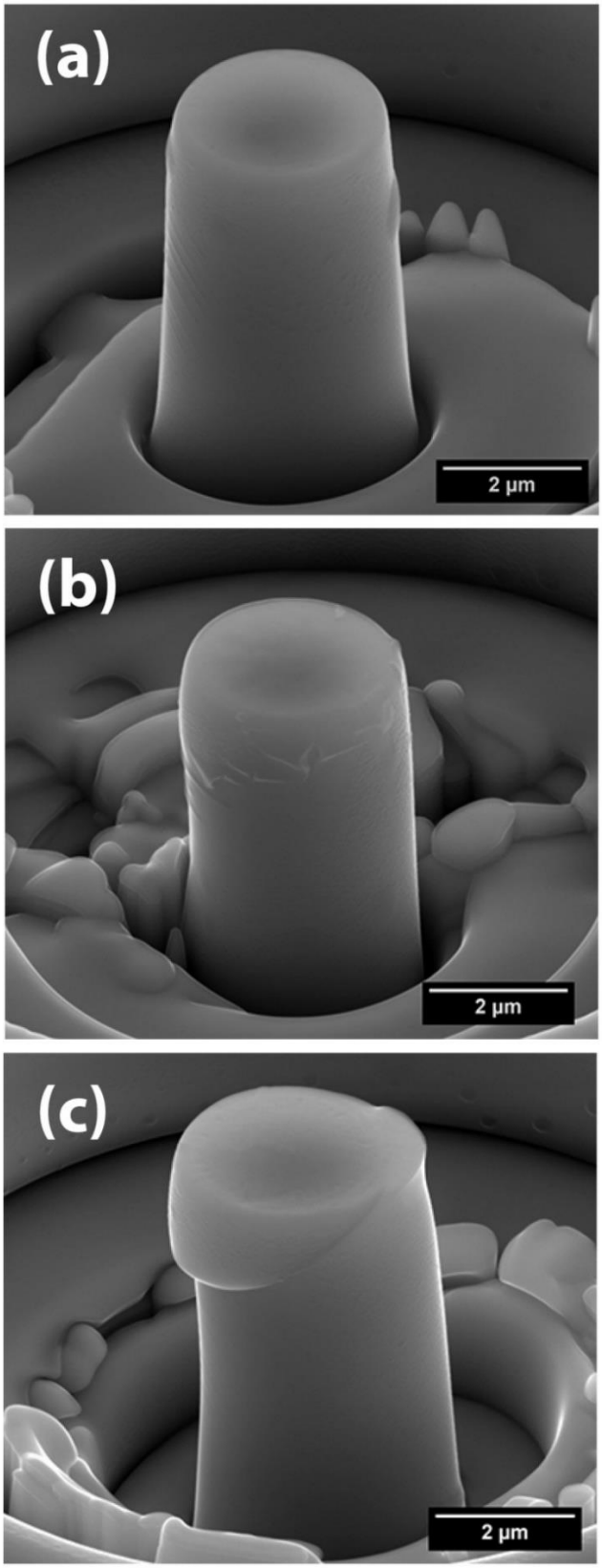

Figure 5-6 SEM images of (a) 2% strain, (b) 5% and (c) 7% compressed 3 µm micro-pillars containing only α phase with [0001] loading direction. There is no observable shearing of micro-pillar at 2% strain and a large shearing of the top part of micro-pillar appeared at 7% strain

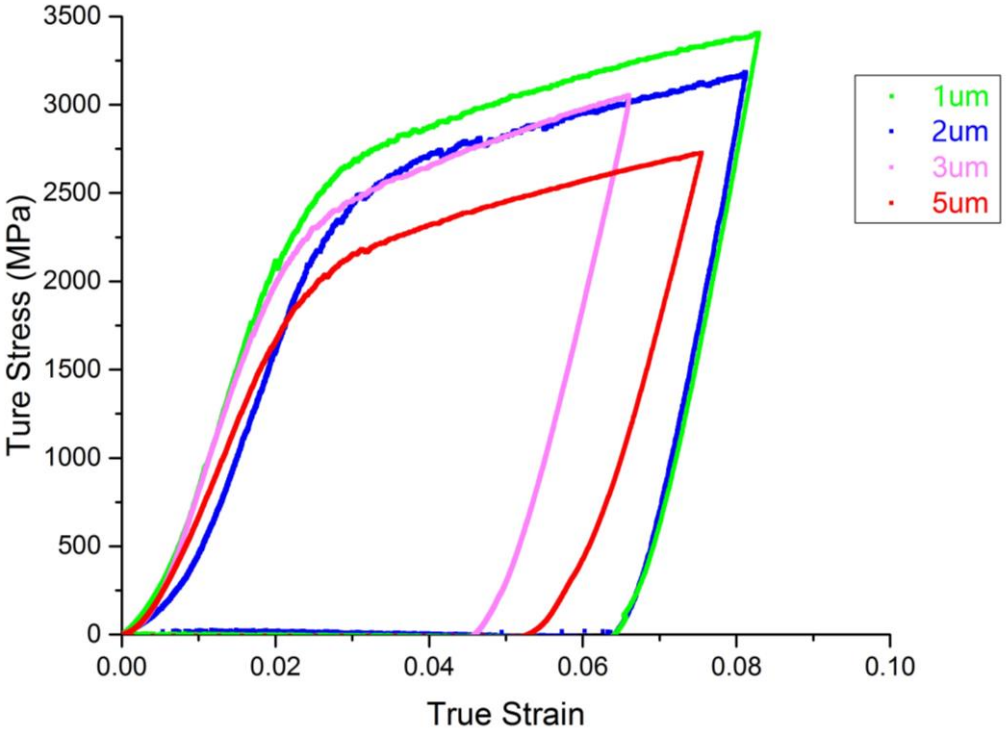

Figure 5-7 Stress-strain curves of the 5% compressed micro-pillars of different diameters containing β fillet between two α along [0001]$_{\alpha}$// [101]$_{\beta}$ loading direction (5µm: pillar #30, 3µm: pillar #33, 2µm: pillar #37, 1µm: pillar #42). There is no observable change of work hardening rate with diameter in this group of micro-pillars)

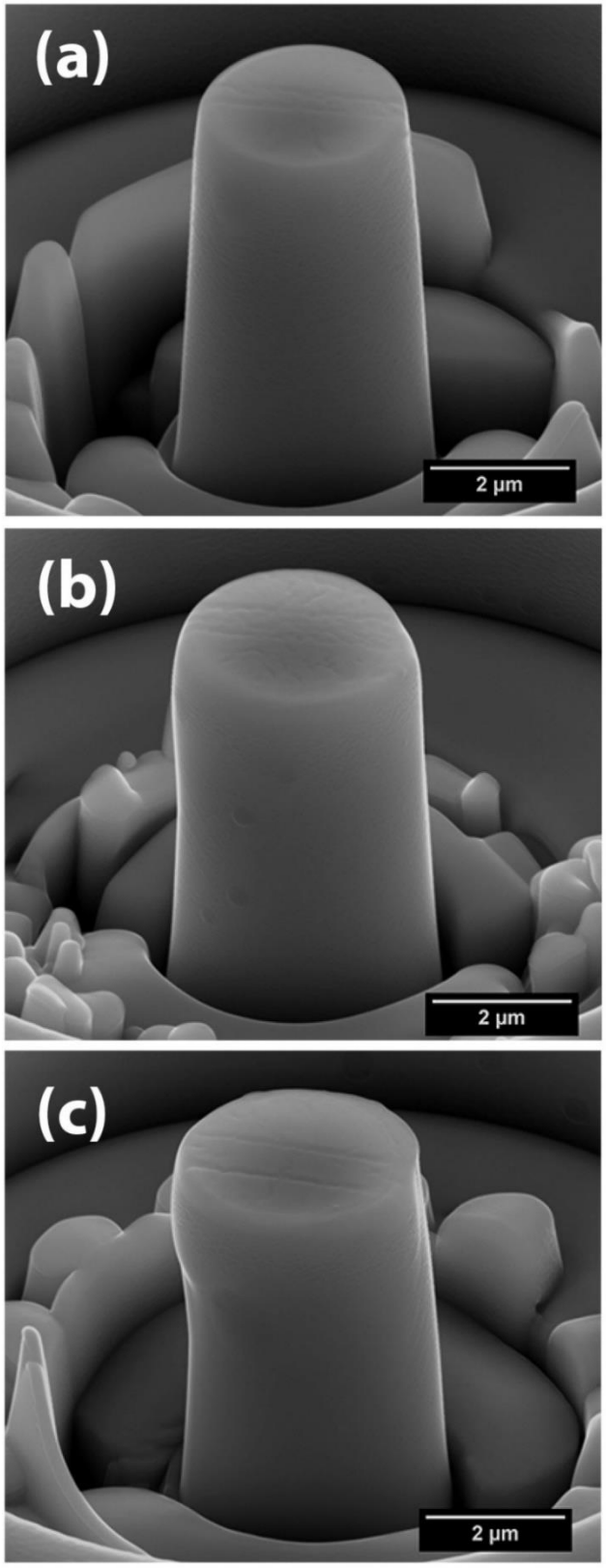

Figure 5-8 SEM images of (a) 2% strain, (c) 5% strain and (b) 7% compressed 3 µm micro-pillars containing α and β phases along [0001] $_{\alpha}$ *// [101]* $_{\beta}$ *loading direction. The plastic deformation does not appear in the form of shearing.*

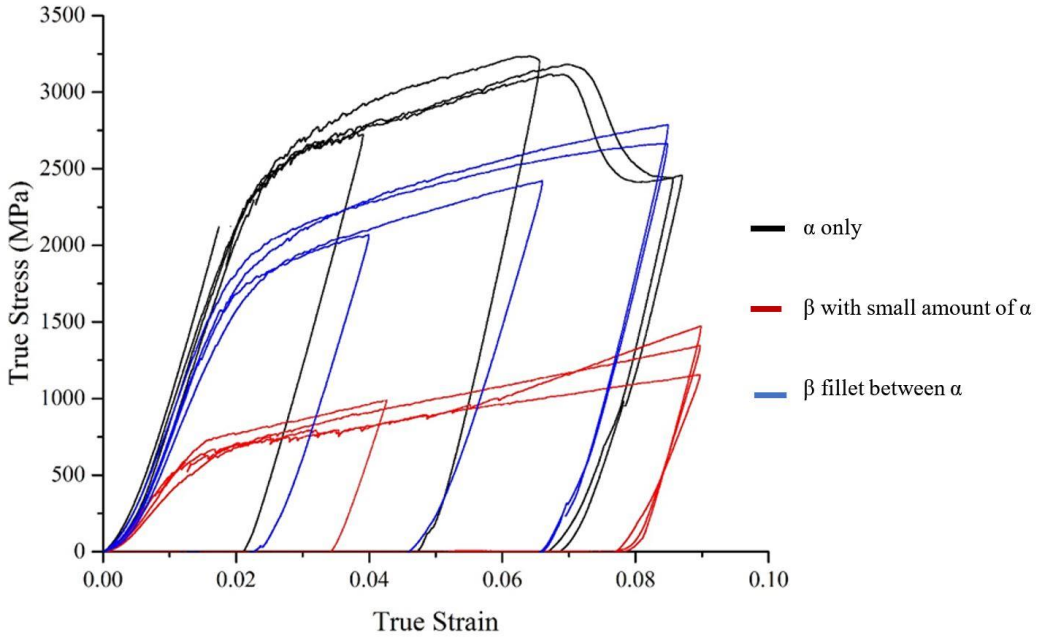

Figure 5-9 Stress-strain curves of the 2%, 5%, and 7% compressed 3 μm micro-pillars containing only α (black curves), β fillet between two α (blue curves), and major β with small amount of α (red curves) along [0001]$_{\alpha}$ // [101]$_{\beta}$ loading direction

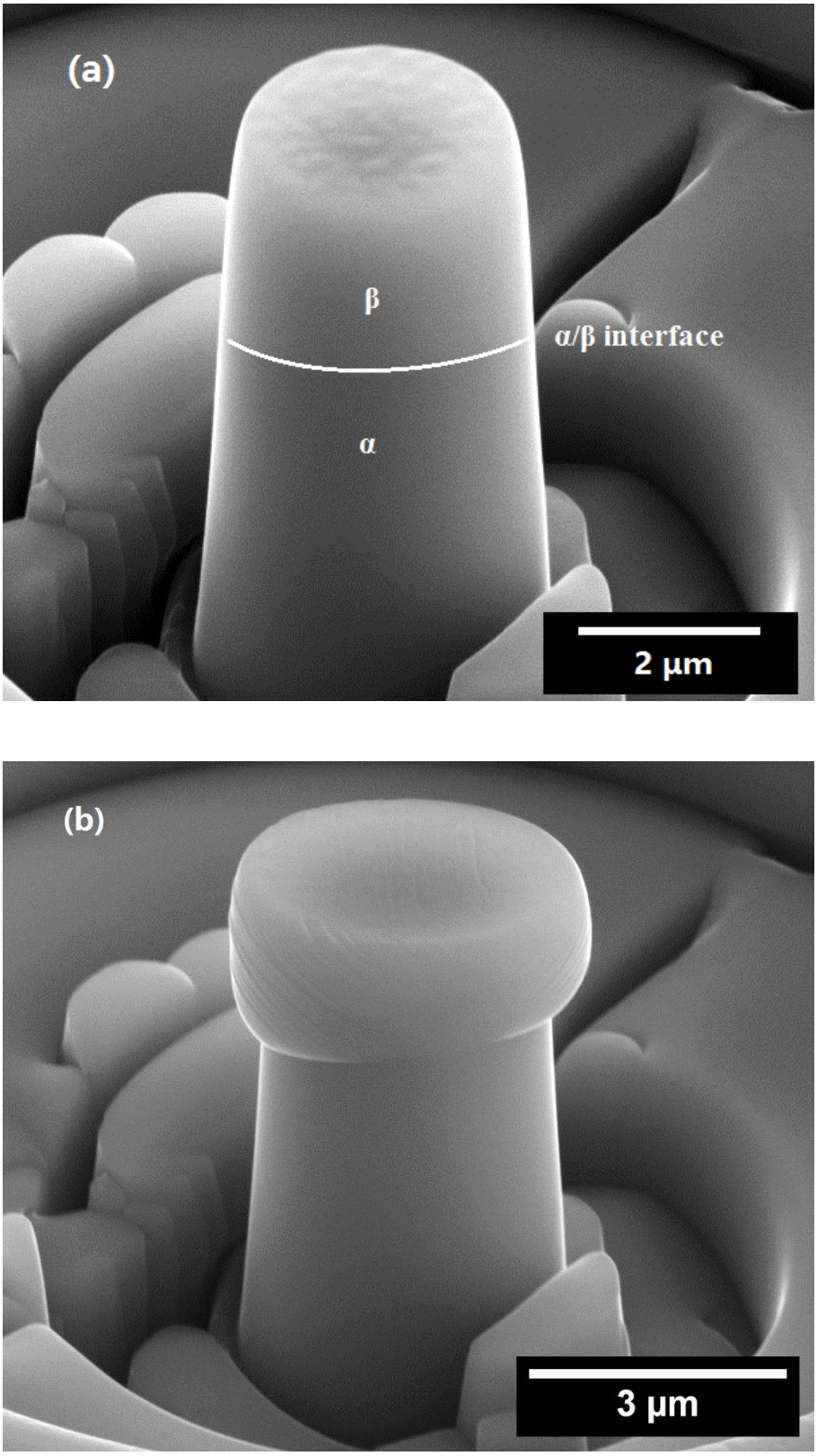

Figure 5-10 SEM images of the 3 µm micro-pillar containing β phase in the top and α phase in the bottom along [0001]$_{\alpha}$// [101]$_{\beta}$ loading direction. (a) is before compression and (b) is after 8% compression

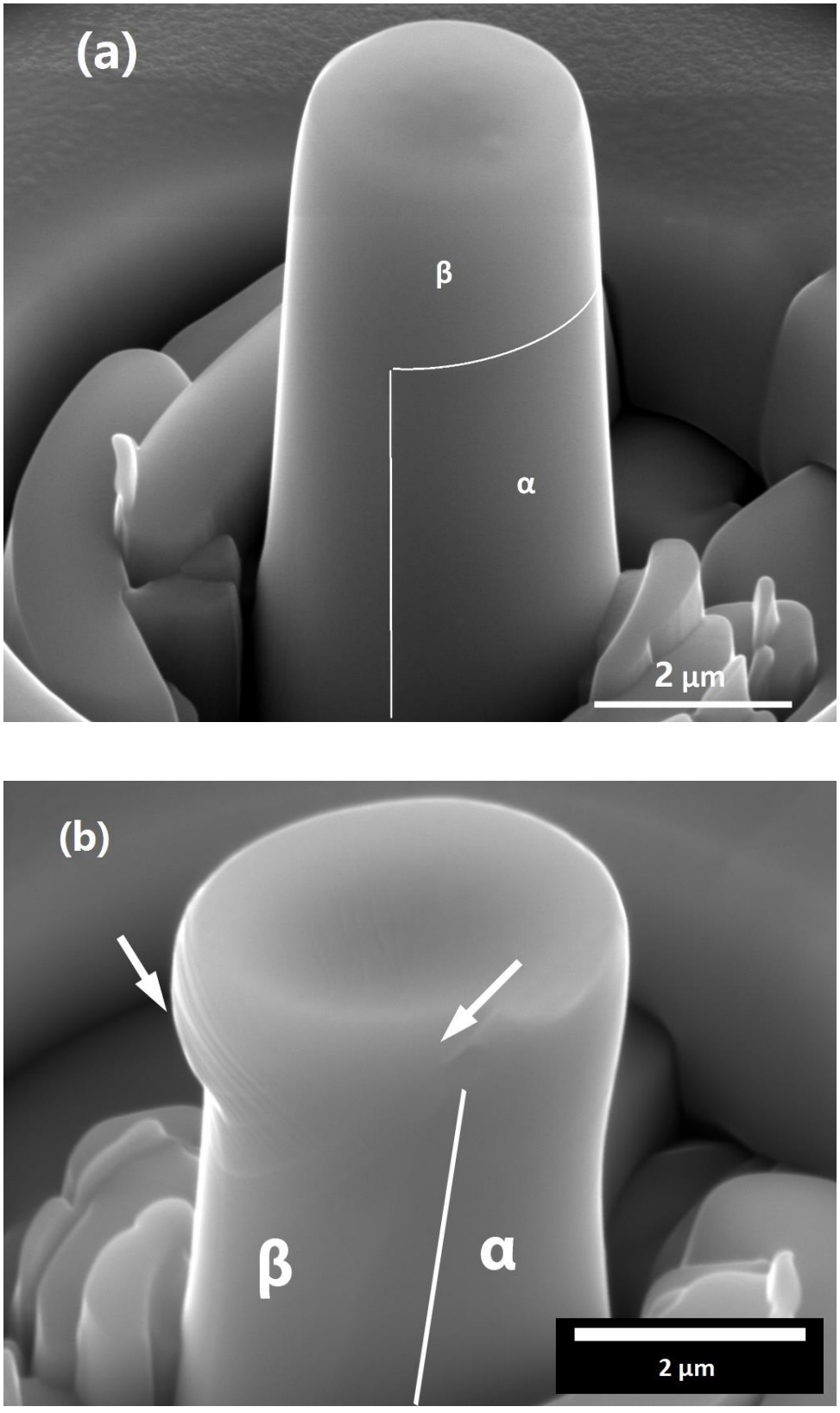

Figure 5-11 SEM images of the 3 μm micro-pillar containing half β phase at the top left and half α phase at the bottom right along [0001]$_{\alpha}$// [101]$_{\beta}$ loading direction. (a) is before compression and (b) is after 8% compression. Two sets of slip bands (indicated by arrows) generated in β phase.

Table 5.1 The yield stress calculated CRSS determined from the compression of pillars of different diameters containing α only in [1$\bar{1}$00] loading direction. (SD = standard deviation)

Pillar diameter	Pillar No.	E (GPa)			0.2% offset yield stress (MPa)			CRSS for <***a***> prismatic slip (MPa)
		Individual	Average	SD	Individual	Average	SD	
5 μm	1	162	140	31	771	775	5	336
	2	118			779			
3 μm	3	134	143	13	923	881	59	381
	4	153			839			
1 μm	5	151	138	18	1217	1114	144	482
	7	126			1012			
0.5 μm	8	145	128	23	1144	1125	26	487
	9	112			1106			

Table 5.2 Experimental yield stress and flow stress of different diameters containing β between α along [1$\bar{1}$00]$_{\alpha}$// [10$\bar{1}$]$_{\beta}$ loading direction. Yield stress and CRSS for the prismatic slip in α phase decreased.

Pillar diameter	Pillar No.	E (GPa)	0.2% offset yield stress (MPa)	CRSS for <***a***> prismatic slip (MPa)
5 μm	10	108	692	300
3 μm	11	118	729	316
2 μm	12	113	785	340
1 μm	13	109	823	356

Table 5.3 Experimental yield stress and flow stress of different diameters containing α only along [0001] loading direction.

Pillar diameter	Pillar No.	E (GPa)			0.2% offset yield stress (MPa)			CRSS for <***c***+***a***> slip on {11$\bar{2}$2} plane (MPa)
		Individual	Average	SD	Individual	Average	SD	
5 μm	15	167	173	9	2241	2298	80	1036
	16	180			2355			
3 μm	17	163	171	5	2853	2878	281	1298
	18	175			3062			
	19	171			3109			
	21	175			2491			
1 μm	22	154	156	2	2884	2963	111	1336
	24	158			3041			
0.5 μm	26	148	148	-	2544	2544	-	1147

Table 5.4 Experimental yield stress and flow stress of different diameters containing β between α phases along [0001]$_{\alpha}$// [101]$_{\beta}$ loading direction.

Pillar diameter	Pillar No.	E (GPa)			0.2% offset yield stress (MPa)			CRSS for <***c***+***a***> slip on {11$\bar{2}$2} plane (MPa)
		Individual	Average	SD	Individual	Average	SD	
5 μm	27	89.5	92	6	1900	1938	122	874
	28	93.7			1964			
	29	101.3			2104			
	30	84.3			1764			
	31	90.8			1959			
3 μm	32	120	115	9	2178	2199	45	992
	33	102			2231			
	34	121			2242			
	35	118			2145			
2 μm	37	102	105	5	1905	2059	217	929
	38	109			2213			
1 μm	41	122	118	6	2207	2278	100	1027
	42	114			2349			

Table 5.5 Experimental yield stress of 3 μm diameter micro-pillars diameters containing different β volume fractions with α phases along [0001]$_α$ // [101]$_β$ loading direction. Yielding happened in β phase first in all these samples.

β volume fraction	Pillar No.	E (GPa)			0.2% offset yield stress (MPa)		
		Individual	Average	SD	Individual	Average	SD
49 % through pillar	46	51	60	6	588	615	58
71 % though pillar	47	66			579		
34 % at pillar top	48	61			591		
69 % at pillar top	49	62			703		

Chapter 6 Dislocation analysis

The study on the deformation microstructure focuses on the dislocation analysis of the micro-pillars with different diameters (from 1 μm to 5 μm) compressed along different loading directions ($[1\bar{1}00]_\alpha$ // $[10\bar{1}]_\beta$ or $[0001]_\alpha$ // $[101]_\beta$) to different strains.

First of all, the microstructure of the alloy before any compression test was studied on several TEM foils prepared from the undeformed bulk Ti-6Al-4V sample after the heat-treatment. For example, a TEM foil extracted with its normal direction parallel to [0001] is shown in Figure 6-1, the sample is almost free of dislocations. Therefore, the effect of initial dislocation densities is regarded as negligible in the current study.

6.1 Micro-pillars compressed along $[1\bar{1}00]_\alpha$ // $[10\bar{1}]_\beta$

6.1.1 The α single phase micro-pillar of 5 μm diameter compressed along $[1\bar{1}00]$

The pillar #2 in Table 4.5 is an α single phase micro-pillar of 5-μm diameter after compressed to 3.5% strain along $[1\bar{1}00]$. Its SEM image is shown in Figure 6-2. There are several slip bands observable between the two arrows indicated in Figure 6-2. The stress-strain curve of the sample is shown in Figure 6-3 and it can be generally characterized as (i) elastic loading, (ii) followed by a transition to stable flow and a continually decreasing work-hardening rate after the onset of plastic flow, (iii) displaying no large strain bursts.

A TEM foil parallel to the basal plane was extracted from the deformed pillar following the dashed lines indicated in Figure 6-2 and its images were shown in Figure 6-4. When imaged along [0001] with $\boldsymbol{g} = 11\bar{2}0$, as shown in Figure 6-4 (a), two sets of dislocations are visible and their slip planes are edge-on. Two more STEM images were taken to determine the Burgers vectors and slip planes of these dislocations. Figure 6-4 (b) was taken with B.D.~[0001], $\boldsymbol{g} = 01\bar{1}0$. The prismatic $\boldsymbol{a_1}$ dislocations $1/3[2\bar{1}\bar{1}0](0\bar{1}10)$ become invisible. The prismatic $\boldsymbol{a_2}$ dislocations $1/3[1\bar{2}10](10\bar{1}0)$ are visible and the slip plane becomes edge-on. Figure 6-4 (c) was taken with B.D.~[0001], $\boldsymbol{g} = 10\bar{1}0$. The prismatic $\boldsymbol{a_2}$ dislocations $1/3[1\bar{2}10](10\bar{1}0)$ become invisible. The prismatic $\boldsymbol{a_1}$ dislocations $1/3[2\bar{1}\bar{1}0](0\bar{1}10)$ become visible and their slip planes are shown as edge-on. The diffraction conditions used for the imaging of these two sets of prismatic $\boldsymbol{a}_1$ and $\boldsymbol{a}_2$ dislocation are listed in Table 6.1. The analysis results are consistent with the Schmid factor calculation (Table 4.2) where two <***a***> prismatic slip systems are expected to be activated.

As explained in section 4.2, the loading direction is 6.3° away from $[1\bar{1}00]$. This resulted in the prismatic $\boldsymbol{a_1}$ slip system $1/3[2\bar{1}\bar{1}0](0\bar{1}10)$ became the dominant one which has sheared the micro-pillar and generated 8 steps as high as ~230 nm in total on the side surface of the micro-pillar in Figure 6-4. Only a few dislocations are of $\boldsymbol{a_2}$ $1/3[1\bar{2}10](10\bar{1}0)$ type and they are mainly located at the top right corner of the sample.

To assess the edge or screw character of the dislocations, the beam direction was tilted within the normal plane of the Burgers vector. If the projections of the dislocation lines are parallel with the corresponding Burgers vector, the dislocations

are screw type; if perpendicular, they are edge type; otherwise, they are mixed type. For example, the STEM images in Figure 6-5 is a bright field STEM image taken along B.D.~[01$\bar{1}$2], showing that a heavily deformed region corresponding to the shear banded region. As the dislocation lines in the slip system are curved, or the straight segments are neither edge nor screw, they are mixed dislocations.

The dislocation density is determined as the total length of dislocation line in a unit volume [112]. It is defined as:

$$\rho = (4/\pi)R/At \qquad (Equation\ 6\text{-}1),$$

where R is the total projected length of dislocation lines in a given area A on a TEM micrograph, t is the thickness of the TEM sample. Dislocation densities in the compressed micro-pillars were calculated based on the STEM image in Figure 6-5. To shorten the calculation time, the dislocation density ρ was approximated using equation [112, 113]:

$$\rho \approx 2N / tL \qquad (Equation\ 6\text{-}2),$$

where N is the number of intersected dislocations with a set of random lines with a total length L. The dislocation density in the dominant slip bands was calculated to be ~5.9 x 10^{13} m^{-2} in Figure 6-5.

6.1.2 The α single phase micro-pillar of 1 μm diameter compressed along [1$\bar{1}$00]

A TEM sample was prepared from the α single phase micro-pillar of 1 μm diameter compressed to 3% strain along [1$\bar{1}$00] (pillar #5 in Table 4.5). Its stress-strain curve is shown in Figure 6-6, Differently from Figure 6-3, the sample with smaller

diameter can be characterized as (i) nonlinear loading at the first 0.5% strain which was commonly displayed in the smaller pillars due to the misalignment between the top surface of micro-pillar and the punch, (ii) work-hardening transiting to work softening at ~0.5% after the yield point, (iii) containing several large stress drops and their magnetite increased with strain. When imaged along [0001] with $\boldsymbol{g} = 11\bar{2}0$, as shown in Figure 6-7 (a), two sets of dislocations are visible and their slip planes are edge-on. Similarly, they can be identified using STEM image in Figure 6-7 (b) taken with B.D.~[0001], $\boldsymbol{g} = 10\bar{1}0$. The prismatic $\boldsymbol{a_2}$ dislocations $1/3[1\bar{2}10](10\bar{1}0)$ become invisible. The prismatic $\boldsymbol{a_1}$ dislocations $1/3[2\bar{1}\bar{1}0](0\bar{1}10)$ become visible and their slip planes are shown as edge-on. The diffraction conditions used for the imaging of these two sets of $\boldsymbol{a}_1$ and $\boldsymbol{a}_2$ prismatic slip systems are listed in Table 6.2. The dislocation density was estimated to be ~ 3.1 x 10^{13} m^{-2} based on the STEM images in Figure 6-7 (c) with B.D.~$[01\bar{1}2]$. g = $\bar{2}110$, and multiple slip steps can be observed on the side surface of the 1 μm diameter micro-pillar, as indicated by arrows in Figure 6-7 (a).

6.1.3 The α/β micro-pillar of 3 μm diameter compressed along $[1\bar{1}00]_\alpha$ // $[10\bar{1}]_\beta$

A micro-pillar of 3 μm diameter containing both α and β phases (the pillar #11 in Table 4.5) was prepared from the same colony and compressed along $[1\bar{1}00]_\alpha$ // $[10\bar{1}]_\beta$. Figure 6-8 (a) shows a shear band runs through the whole pillar from the top surface and left a big step on the right side of the pillar, as indicated by the white arrow. This shear band corresponds to the one recorded on SEM (cf. Figure 5-4). There is another set of dislocations (indicated by black arrow) generated from just

underneath the β phase which however has not run through the whole pillar and stopped in front of the black arrow. Figure 6-8 (b) shows the magnified area in Figure 6-8 (a) that short dislocations come out from the upside of α/β. The dislocation density in the α phase was calculated to be ~4.7 x 10^{13} m^{-2} based on the STEM image in Figure 6-8 (a), which is slightly lower than that in the 5 μm diameter α single phase pillar but slightly higher than that in the 1 μm diameter α single phase micro-pillar. What should be noticed is that this dislocation density only revealed the situation in the micro-pillar unloaded at the 4% strain. The dislocation densities are probably different at different strains based on the stress-strain curve of this sample shown in Figure 6-9. It showed a work-hardening for ~0.3% strain after the yield and turned to work softening to ~2% strain and then gradually transited to work hardening again. The serration of stress is much smaller compared with the micro-pillar without α/β interface in Figure 6-3.

The STEM bright field image in Figure 6-10 (a) was taken with the electron beam direction parallel to the foil normal direction $[0001]_\alpha$ // $[101]_\beta$ with $\boldsymbol{g} = 11\bar{2}0$. All dislocations are visible and the slip bands are shown edge-on in both α and β phases. The two sets of prismatic $\boldsymbol{a}_1$ and $\boldsymbol{a}_2$ slip systems could be identified following the diffraction conditions used, as listed in Table 6.2. The primary slip system is the $\boldsymbol{a}_1$ prismatic slip system $1/3[2\bar{1}\bar{1}0](0\bar{1}10)$, the same as that in the single α phase pillar of 5 μm diameter. The $\boldsymbol{a}_2$ prismatic slip system $1/3[1\bar{2}10](10\bar{1}0)$ however has not cut through the α/β interface.

The slip systems activated in β phase were also identified based on the dislocations visibility criterion and the slip plane edge-on condition. In Figure 6-10 (a) when

B.D. ~ $[101]_{\beta}$, both slip planes of two sets of slip systems are shown edge-on. In Figure 6-11 (a), when B.D.~[111], $\boldsymbol{g} = \bar{1}10$, the dominant slip system became invisible and the other slip system is visible. In Figure 6-11 (b), when B.D.~[111], $\boldsymbol{g} = 01\bar{1}$, the dominant slip system is visible and the other slip system becomes invisible. Based on the diffraction conditions of the slip systems summarized in Table 6.2, the two slip systems can be inferred as $\boldsymbol{b}_1$ $1/2[11\bar{1}](\bar{1}21)$ plane and $\boldsymbol{b}_2$ $1/2[1\bar{1}\bar{1}](12\bar{1})$ from the slip systems as listed in Table 4.3 and they are consistent with the prediction based on the Schmid factors of the slip system as shown in Table 4.3.

A series of higher magnification STEM bright filed images under the same beam condition as that in Figure 6-10 (a) are shown in Figure 6-12. The slip $\boldsymbol{b}_1$ and $\boldsymbol{b}_2$ are corresponding to the two sets of slip $\boldsymbol{a}_1$ and $\boldsymbol{a}_2$ in the α phase. The angle between $\boldsymbol{a}_1$ and $\boldsymbol{b}_1$ was measured to be ~ 0.5°. The fact that the magnitude difference between $|\boldsymbol{a}_1| = 0.295$ nm and $|\boldsymbol{b}_1| = 0.284$ nm [51] is less than 4% suggests that the dislocation of the $\boldsymbol{a}_1$ prismatic slip system can transfer through the α/β interface, with very small residual strain at the interface, as reported in the bulk Ti-6Al-4V sample [51]. However, $\boldsymbol{a}_2$ and $\boldsymbol{b}_2$ have a large angular difference of ~ 12.8°. As the angles between two planes (0001) and (101) is almost zero and the prismatic slip planes for $\boldsymbol{a}_1$ and $\boldsymbol{a}_2$ and $(\bar{1}21)$ / $(12\bar{1})$ slip planes for $\boldsymbol{b}_1$ and $\boldsymbol{b}_2$ are all normal to $(0001)_{\alpha}$ // $(101)_{\beta}$. Therefore, the angle between $(0\bar{1}10)$ and $(\bar{1}21)$ slip plane are same as the ~ 0.5° angle between $\boldsymbol{a}_1$ and $\boldsymbol{b}_1$, and the angle between $(10\bar{1}0)$ and $(12\bar{1})$ slip plane are same as the ~ 12.8° angle between $\boldsymbol{a}_2$ and $\boldsymbol{b}_2$.

As shown in Figure 6-10, no $\boldsymbol{a}_2$ dislocation or shear band formed have cut through the α/β interface. Several $\boldsymbol{b}_2$ dislocations can be observed in the β phase near the top α/β interface, but not in the middle or bottom α/β.

6.1.4 The α/β micro-pillar of 1 μm diameter compressed along $[1\bar{1}00]_\alpha // [10\bar{1}]_\beta$

The SEM image in Figure 6-13 is obtained from the micro-pillar (the pillar #13 in Table 4.5) of 1 μm diameter containing both α and β phases compressed along $[1\bar{1}00]_\alpha // [10\bar{1}]_\beta$ showing only one set of visible parallel slip bands. The stress-strain curve of the micro-pillar is shown in Figure 6-14. It showed a gradually decreased work-hardening rate after yield and relatively large magnitude serration of stress compared with the pillar of larger diameter in section 6.1.3.

The TEM foil was prepared parallel to the basal plane (0001) of the α phase. In the STEM bright field image shown in Figure 6-15 (a) taken with B.D.~ $[0001]_\alpha$ // $[101]_\beta$, $\boldsymbol{g} = 11\bar{2}0_\alpha // 020_\beta$, there is one set of slip system in the α phase and its slip plane is shown edge-on. When the imaging condition is changed to B.D.~ [0001], $\boldsymbol{g} = 01\bar{1}0$, as shown in Figure 6-15 (b), the dislocations in the α phase become invisible. When the imaging condition is changed to B.D.~ $[1\bar{2}13]$, $\boldsymbol{g} = 10\bar{1}0$, as shown in Figure 6-15 (c), $\boldsymbol{a}_1$ dislocations show as curved dislocation lines. Therefore, these are $\boldsymbol{a}_1$ dislocations belong to the prismatic slip system $1/3[2\bar{1}\bar{1}0](0\bar{1}10)$. The diffraction conditions used for the imaging are listed in Table 6.4. A higher magnification STEM bright field image of the β phase is shown in Figure 6-16 (a) with B.D.~[101], $\boldsymbol{g} = 020$. It shows that one set of corresponding $\boldsymbol{b}_1$ dislocations in the β phase become visible and their slip plane is shown edge-on.

When the imaging condition is changed to ~[102], $\boldsymbol{g}$ = 020, as shown in Figure 6-16 (b), the curved dislocations are clearly visible. The curvature indicated the dislocations moving from the side surface of the micro-pillar towards the upside α/β interface. It can be inferred that these are 1/2 $[11\bar{1}]$ $(\bar{1}21)$ dislocations from the slip systems as listed in Table 4.3 according to the observation of diffraction condition summarized in Table 6.5.

6.2 Micro-pillars compressed along [0001] $_{\alpha}$ // [101] $_{\beta}$

6.2.1 The α single phase micro-pillar of 1 μm diameter compressed along [0001]

In Figure 6-17, the α single phase micro-pillar (Table 4.5 micro-pillar #24) of 1 μm diameter compressed to 6% strain along [0001] shows no obvious slip band on the side surface in the SEM image. Instead, it swells at the right side of the micro-pillar. The stress-strain curve of the micro-pillar is shown in Figure 6-18. The first ~1% strain after yield shows a strong work-hardening, and then it changes to a relatively low but constant work hardening rate. The serration of stress keeps at a low magnitude.

A TEM foil was extracted from the middle of the micro-pillar along the dash lines in Figure 6-17, with the foil normal direction parallel to $[2\bar{1}\bar{1}0]$. Figure 6-19 is the STEM image taken with the electron beam direction ~$[2\bar{1}\bar{1}0]$, $\boldsymbol{g}$ = 0002, where all <$\boldsymbol{c}$+$\boldsymbol{a}$> type dislocations are visible. In this sample, the top part of the pillar has been subjected to heavy deformation and contains a very dense dislocation structure which is difficult to analyze individually.

In the middle of the micro-pillar, three groups of dislocations can be identified and are marked as I, II and III in Figure 6-19 (a). The three groups can be identified from the twelve 1st order pyramidal <***c+a***> slip systems and six 2nd order pyramidal <***c+a***> slip systems as listed in Table 4.2, based on the invisibility and edge-on condition of these dislocations and slip planes under different imaging conditions used as shown in Figure 6-19. Firstly, no 1st order pyramidal <***c+a***> dislocation on $\{10\bar{1}1\}$ plane should be shown edge-on when beam direction is along ~$[4\bar{2}\bar{2}\bar{3}]$, $[1\bar{1}00]$, or $[10\bar{1}0]$, while the slip planes of dislocations (I and III) are edge-on in Figure 6-19 (c) and (d). Therefore, these slip systems are likely the 2nd order pyramidal <***c+a***> dislocations. The visibility analysis of six 2nd order pyramidal <***c+a***> dislocations is listed in Table 6.6. Group I dislocations are always visible in Figure 6-19 (a), (b), (c), (d), and (e) and become edge-on only in Figure 6-19 (d) when the beam direction is along $[1\bar{1}00]$. Therefore, they belong to slip system $1/3[11\bar{2}3]$ $(\bar{1}\bar{1}22)$. Group III dislocations are always visible in Figure 6-19 (a), (b), (c), (d), and (e) and their slip planes become edge-on when the beam direction is parallel to $[4\bar{2}\bar{2}\bar{3}]$ as shown in Figure 6-19 (c) or parallel to $[10\bar{1}0]$ as shown in Figure 6-19 (e). Therefore, this set of dislocations belong to slip system $1/3$ $[\bar{1}2\bar{1}3]$ $(1\bar{2}12)$. For Group II dislocations, they are always visible except when $\boldsymbol{g} = 0\bar{1}10$ and they are not shown edge-on in any of the conditions used here. However, in Figure 6-19 (a) (d) and (e), the dislocation lines of Group II dislocations are at their longest length when B.D. is ~$[2\bar{1}\bar{1}0]$, and the same dislocation line has about $\sqrt{3}/2$ of the longest length when B.D. is ~$[1\bar{1}00]$ and $[10\bar{1}0]$. This indicates these dislocation lines are <***c+a***> dislocations on either $(2\bar{1}\bar{1}2)$ or $(\bar{2}112)$ rather on $\{10\bar{1}1\}$ planes. It is also noticed that when the beam direction was tilted from

$[2\bar{1}\bar{1}0]$ to $[4\bar{2}\bar{2}\bar{3}]$, the spacing between dislocations in this group becomes shorter. This suggests that these dislocations are likely on $(\bar{2}112)$ plane rather than on $(2\bar{1}\bar{1}2)$. In other words, the Group II dislocations belong to slip system $1/3[2\bar{1}\bar{1}3]$ $(\bar{2}112)$.

6.2.2 The α/β micro-pillar of 1 μm diameter compressed along [0001]$_\alpha$ // [101]$_\beta$

A TEM foil in Figure 6-20 was prepared from the α/β micro-pillar (the pillar #39 in Table 4.5) of 1 μm diameter compressed to 2% strain along $[0001]_\alpha$ // $[101]_\beta$. Its stress-strain curve is shown in Figure 6-21. The pillar was unloaded shortly after the yield and it only shows the part of the stress-strain curve with high work-hardening rate and no obvious serration of stress. The foil normal direction is parallel to $[2\bar{1}\bar{1}0]_\alpha$ // $[11\bar{1}]_\beta$. As shown in Figure 6-20 (a), two sets of dislocations marked as I and II are observable. Set I dislocations are determined to be $1/3[\bar{2}113]$ $(\bar{2}112)$. The procedure used to determine the slip system is the same as that stated in the previous section. Dislocations in set II are visible and their slip plane is edge-on when the imaging condition is B.D.~ $[2\bar{1}\bar{1}0]$ and $\boldsymbol{g} = 000\bar{2}$. Therefore, this set of dislocations are likely the <***c+a***> dislocations on $(01\bar{1}1)$ plane. However, the available imaging conditions are not enough $\boldsymbol{g}$ to determine the Burgers vector between $1/3[1\bar{2}13]$ and $1/3[\bar{1}\bar{1}23]$ in this set of dislocations. Although the shear of β phase in the 1 μm micro-pillar can be seen clearly in Figure 6-20, the β phase in this sample is too narrow to analyze the dislocations inside.

6.2.3 The α/β micro-pillar of 2 μm diameter compressed along [0001]$_\alpha$ // [101]$_\beta$

A TEM foil with foil normal direction ~[$2\bar{1}\bar{1}0$]$_\alpha$ // [$11\bar{1}$]$_\beta$ was extracted from a α/β micro-pillar (the pillar #37 in Table 4.5) of 2 μm diameter compressed to 6.5% strain along [0001]$_\alpha$ // [101]$_\beta$, with the SEM image shown in Figure 6-22 and the stress-strain curve shown in Figure 6-23. There is no observable slip trace on the side face of the micro-pillar. Correspondingly, the stress-strain curve is relatively smooth without any observable stress drops. The work-hardening rate shows similar trend as other pillars in this orientation: a large work-hardening rate after the yield transiting into a constant work-hardening rate after ~1% strain.

In this sample, there is a heavily deformed area with some recognizable dislocations outside of the area. The slip systems outside of the heavily deformed area are similar to those in the α single phase micro-pillar of 1 μm diameter compressed to 6.5% strain along [0001]. Based on the invisibility and edge-on condition analysis, as shown in Figure 6-24, dislocations marked (I, II and III) are determined to be <***c***+***a***> dislocations on the 2nd order pyramidal plane. Slip system I is 1/3 [$\bar{1}\bar{1}23$] ($11\bar{2}2$). Slip system II is 1/3 [$\bar{1}2\bar{1}3$] ($1\bar{2}12$). Slip system III is 1/3 [$2\bar{1}\bar{1}3$] ($\bar{2}112$). The imaging conditions used are listed in Table 6.8. As the slip systems analysis is similar to the section 6.2.1, it is not repeated here.

6.2.4 The α/β micro-pillar of 3 μm diameter compressed along [0001]$_\alpha$ // [101]$_\beta$

A TEM sample (as shown in Figure 6-25 and Figure 6-26) was extracted from the α/β micro-pillar of 3 μm diameter compressed to 2.5% strain along [0001]$_\alpha$ // [101]$_\beta$ with the foil normal direction ~[$2\bar{1}\bar{1}0$]$_\alpha$ // [$11\bar{1}$]$_\beta$, i.e. perpendicular to the α/β interface (the pillar #32 in Table 4.5). Its stress-strain curve in Figure 6-27 shows similar trend as other pillars in the orientation. The STEM image in Figure 6-25 (a) was taken with B.D.~[$2\bar{1}\bar{1}0$]$_\alpha$ // [$11\bar{1}$]$_\beta$, $\boldsymbol{g}$ = $000\bar{2}_\alpha$ // $\bar{1}0\bar{1}_\beta$. Two sets of <***c*+*a***> dislocations in the α phase, marked as I and II, are visible. Two sets of dislocations in the β phase are also visible as well. The dislocations in set I become edge-on when B.D.~[$4\bar{2}\bar{2}3$], $\boldsymbol{g}$ = $1\bar{1}02$ as shown in Figure 6-25 (b). This slip system was identified as the 2nd order pyramidal <***c*+*a***> slip 1/3[$\bar{1}\bar{1}23$] ($11\bar{2}2$). The slip planes of dislocations in set II become edge on when B.D.~[$2\bar{1}\bar{1}0$], $\boldsymbol{g}$ = $000\bar{2}$ as shown in Figure 6-25 (a). These dislocations can be identified as <***c*+*a***> pyramidal slip on ($01\bar{1}1$) plane. However, the available imaging conditions are not enough $\boldsymbol{g}$ to determine the Burgers vector between 1/3[$1\bar{2}13$] and 1/3[$\bar{1}\bar{1}23$] in this set of dislocations. The imaging conditions are listed in Table 6.9.

Two groups of dislocations are observable in the β phase. In Figure 6-25 (c), they are marked as $\boldsymbol{b}_1$ and $\boldsymbol{b}_2$, all dislocations in the β phase are shown edge-on when B.D.~ [$10\bar{1}$], $\boldsymbol{g}$ = $\bar{1}0\bar{1}$. According to the STEM image in Figure 6-26 (a) taken with B.D.~ [$11\bar{1}$], $\boldsymbol{g}$ = $1\bar{1}0$, the dislocations in group $\boldsymbol{b}_1$ become invisible. In Figure 6-26 (b) taken with B.D. ~[$11\bar{1}$], $\boldsymbol{g}$ = 011, the dislocations in group $\boldsymbol{b}_2$ become invisible.

According to the imaging conditions as summarized in Table 6.10. The two groups of dislocations can be identified as 1/2[111](1$\bar{2}$1) and $\boldsymbol{b}_2$ 1/2[1$\bar{1}$1](121).

6.2.5 The micro-pillar containing β phase in majority of 3 μm diameter compressed along [0001]$_\alpha$ // [101]$_\beta$

The SEM image in Figure 6-28 shows two sets of slip traces on the 3 μm diameter micro-pillar containing β phase in majority along [0001] $_\alpha$ // [101] $_\beta$ after 8% deformation (the pillar # 37 in Table 4.5). Its stress-strain curve is shown in Figure 6-29. In the first ~1% strain after yield, the serration of stress is obvious. It is likely to be the deformation of the β phase at the top of the pillar. After that, it transits into a smooth curve with constant work-hardening rate, which is quite similar to the deformation curves of α phase in the previous section.

A TEM foil with the normal direction parallel to [10$\bar{1}$] was extracted from the deformed pillar. The STEM image in Figure 6-30 (a) was taken with B.D. ~[10$\bar{1}$], $\boldsymbol{g}$ = 0$\bar{2}$0. The left part (about 2/3 of the total foil area) is the β phase and the right part is the α phase. Most dislocations are accommodated in the β phase. In the β phase, two sets of dislocations ($\boldsymbol{b}_1$ and $\boldsymbol{b}_2$) are visible and shown edge-on. The imaging conditions for Figure 6-30 (b) are B.D.~ [11$\bar{1}$], $\boldsymbol{g}$ = 1$\bar{1}$0, which makes the $\boldsymbol{b}_1$ dislocations invisible. In Figure 6-30 (c) with B.D. ~[11 $\bar{1}$], $\boldsymbol{g}$ = 011, $\boldsymbol{b}_2$ dislocations are invisible under the imaging conditions. According to the imaging conditions analysis summarized in Table 6.11, these two slip systems can be identified as $\boldsymbol{b}_1$ 1/2[111](1$\bar{2}$1) and $\boldsymbol{b}_2$ 1/2[1$\bar{1}$1](121).

In summary, the slip systems activated in the micro-pillars compressed along two different orientations were identified in this chapter. In all micro-pillars compressed

along ~[$1\bar{1}00$], regardless of the existence of the α/β interface, $\boldsymbol{a}_1$ prismatic slip is dominant and fewer $\boldsymbol{a}_2$ prismatic dislocations are activated due to the deviation from the exact [$1\bar{1}00$]. In micro-pillars compressed along [0001], both 1st order and 2nd order pyramidal <***c+a***> dislocations can be observed at 2% strain. However only 2nd order pyramidal <***c+a***> slip can be identified from the edge of the heavily deformed area when compressed to 7% strain. The dislocation distributions and interaction with the α/β interface were also observed. The relation between the TEM analysis results in this chapter and the mechanical test results in Chapter 5 will be discussed in the next chapter.

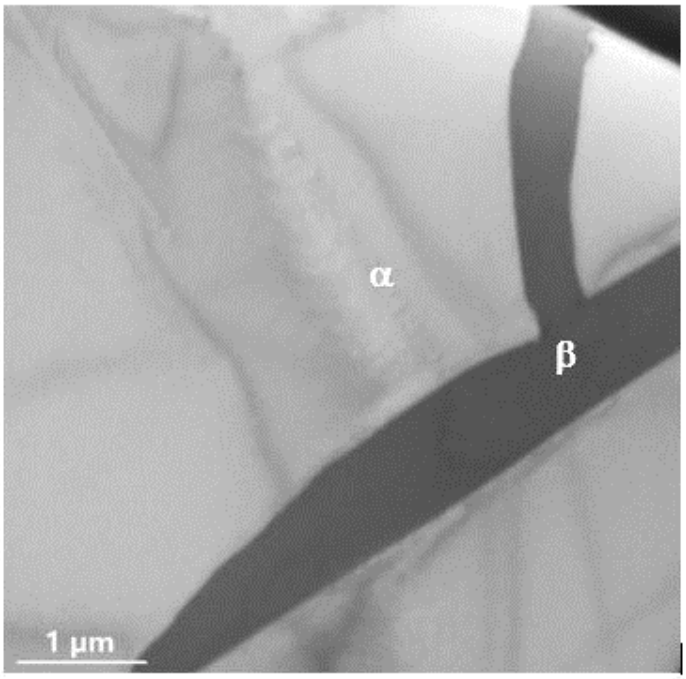

Figure 6-1 Bright-field TEM image obtained from the as-annealed Ti-6Al-4V sample. The sample is free of dislocations in both α and β phases under different beam conditions.

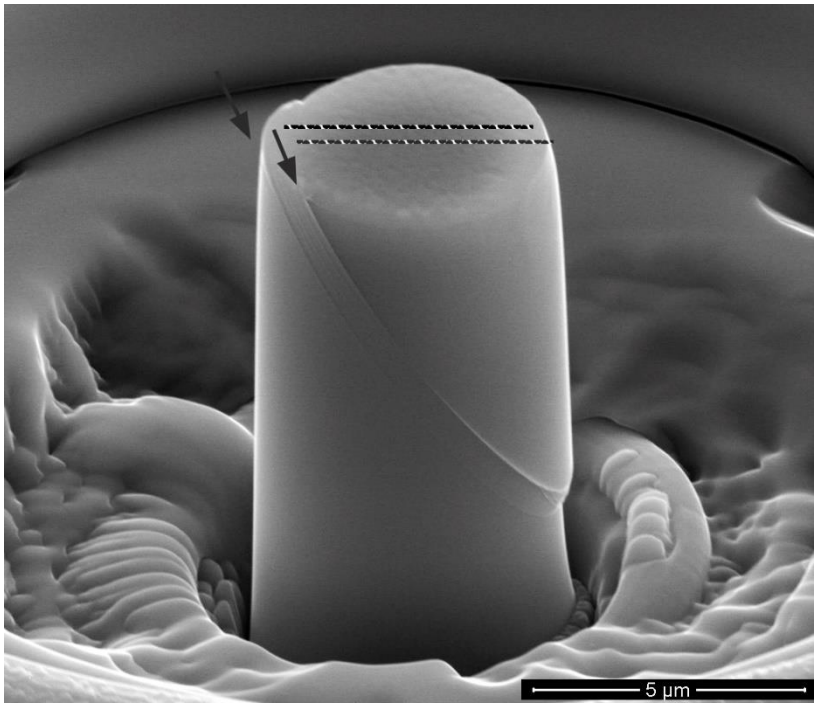

Figure 6-2 SEM image obtained from an α single phase pillar of 5 µm diameter deformed to 3.5% strain along [1$\bar{1}$00]. Two parallel shear bands (as indicated by the arrows) are visible. The TEM foil was cut from top to bottom along the dashed line.

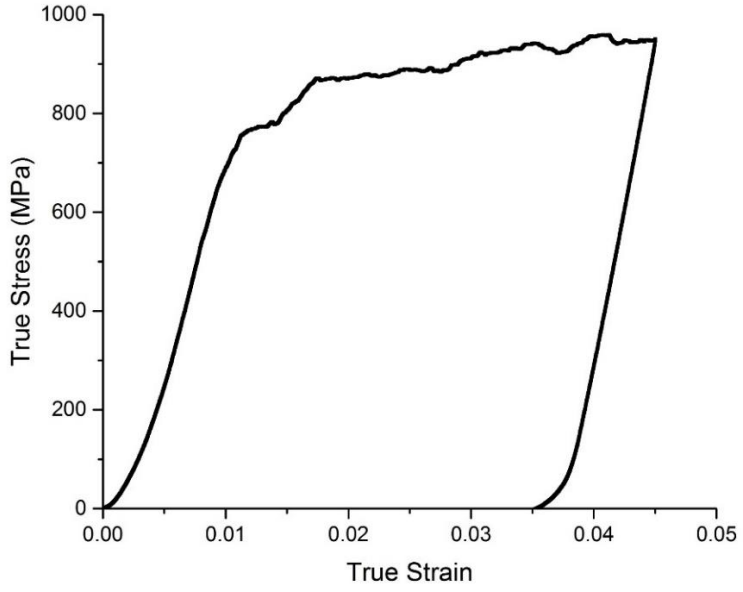

Figure 6-3 The stress-strain curve corresponding to the TEM sample in section 6.1.1.

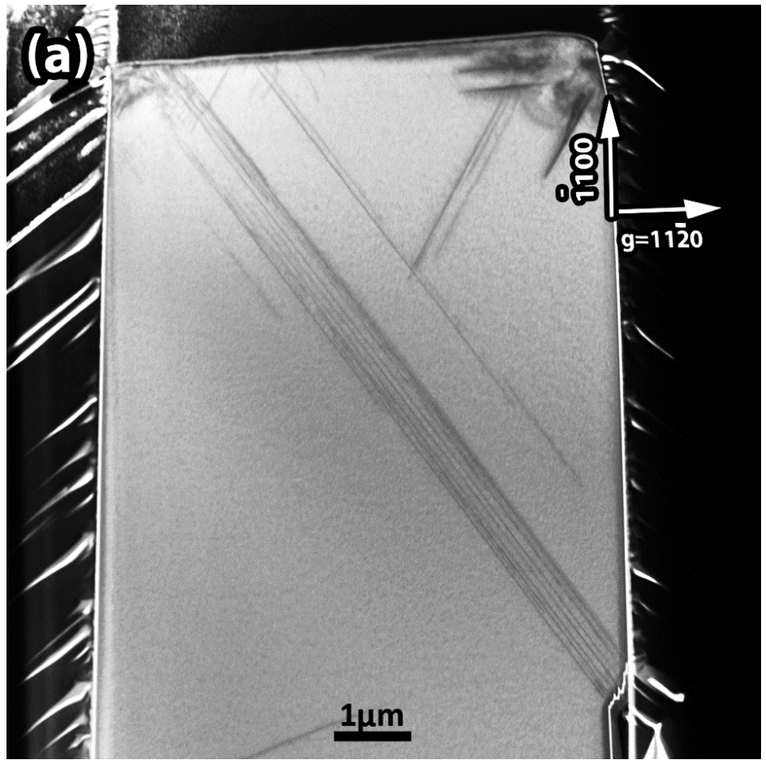

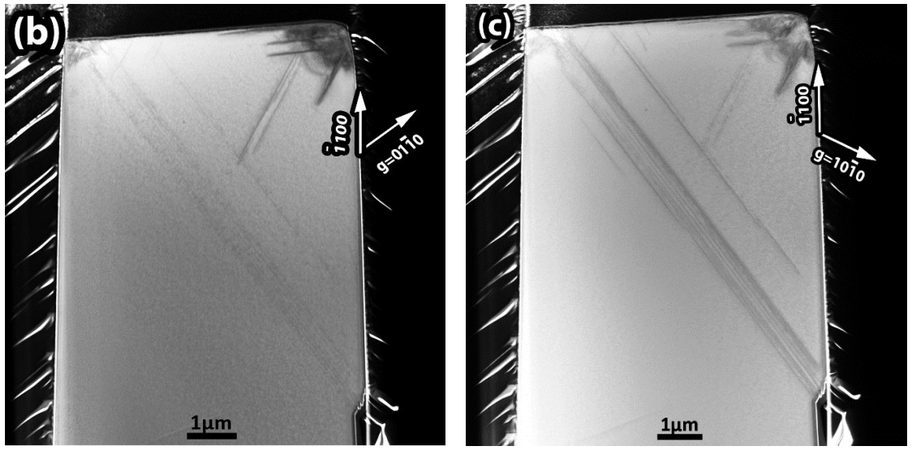

*Figure 6-4 STEM bright image obtained from an α single phase pillar of 5 μm diameter compressed along [0$\bar{1}$10]. The foil normal direction is parallel to [000$\bar{1}$], (a) B.D.~[0001], **g** =11$\bar{2}$0. Two sets of slip systems are visible and their slip planes are edge-on. (b) B.D.~[0001], **g** = 01$\bar{1}$0. Slip system 1/3[2$\bar{1}\bar{1}$0](0$\bar{1}$10) became invisible. (c) B.D.~[0001], **g** = 10$\bar{1}$0. Slip system 1/3[1$\bar{2}$10](10$\bar{1}$0) became invisible.*

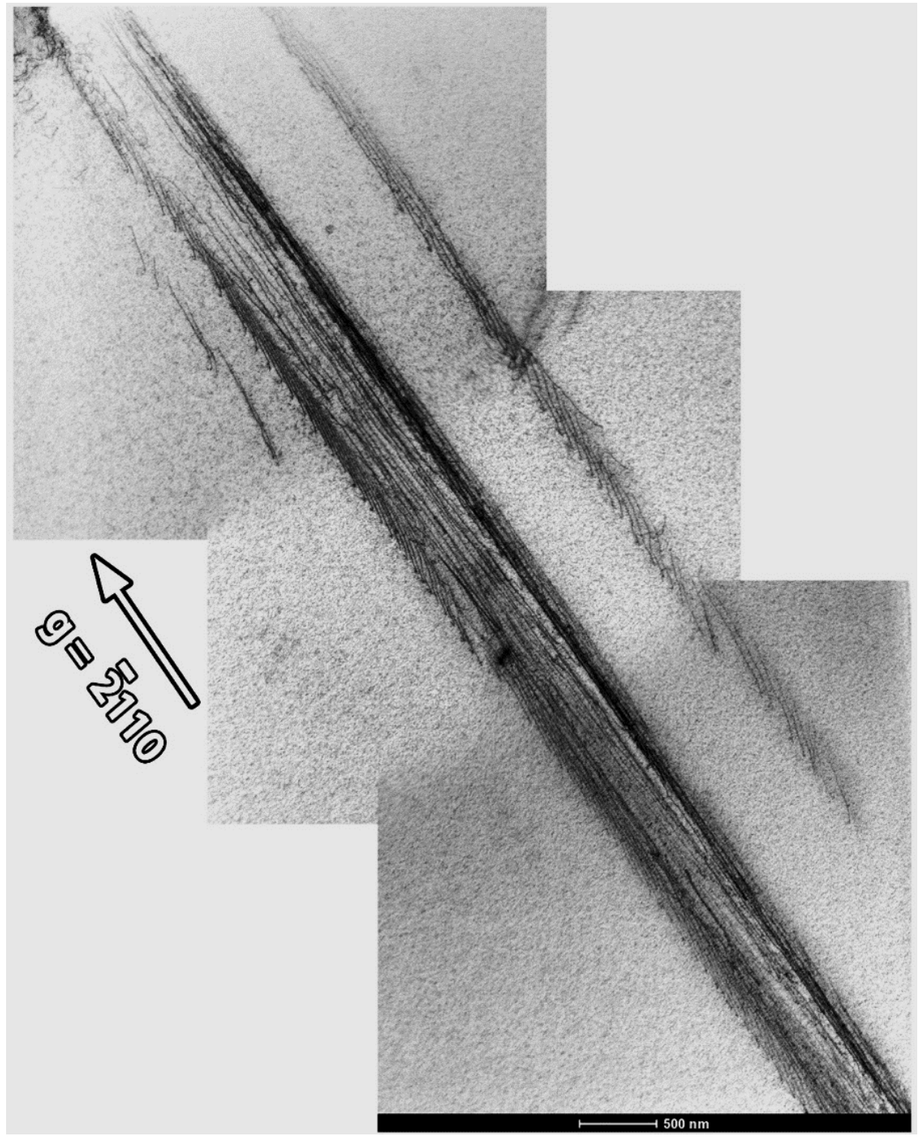

*Figure 6-5 STEM image of slip bands in Figure 6-2 B.D.~[01$\bar{1}$2], **g** = $\bar{2}$110. The slip bands consist of curved dislocation lines coming from the micro-pillar top surface.*

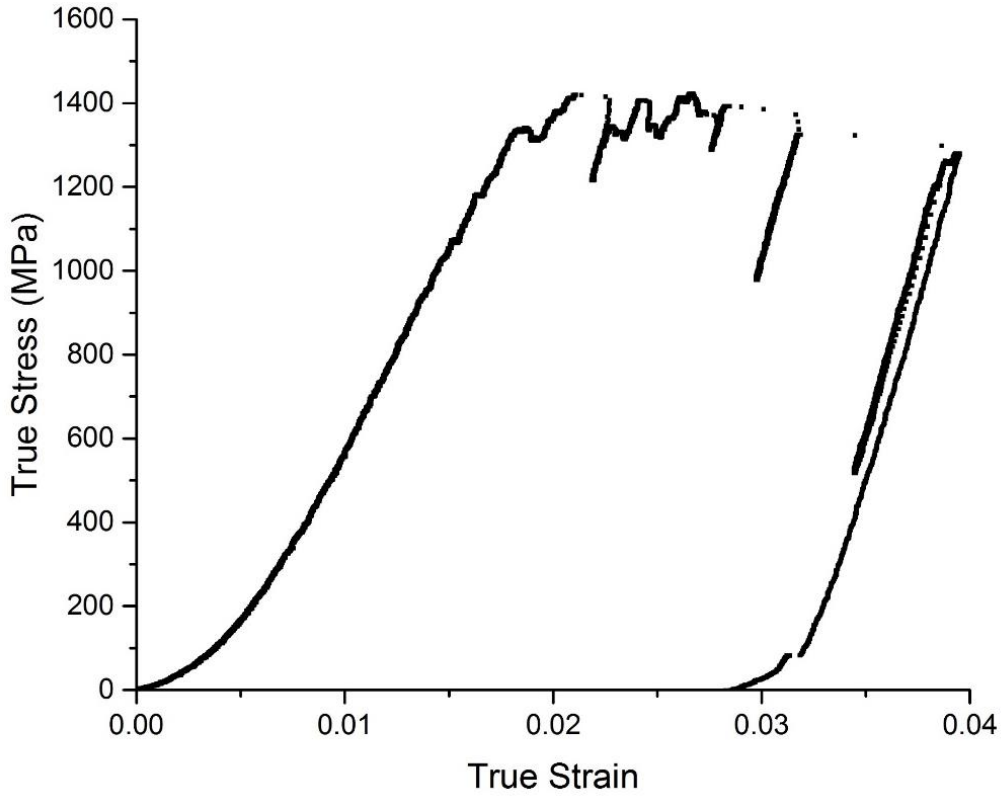

Figure 6-6 The stress-strain curve corresponding to the TEM sample in Section 6.1.2

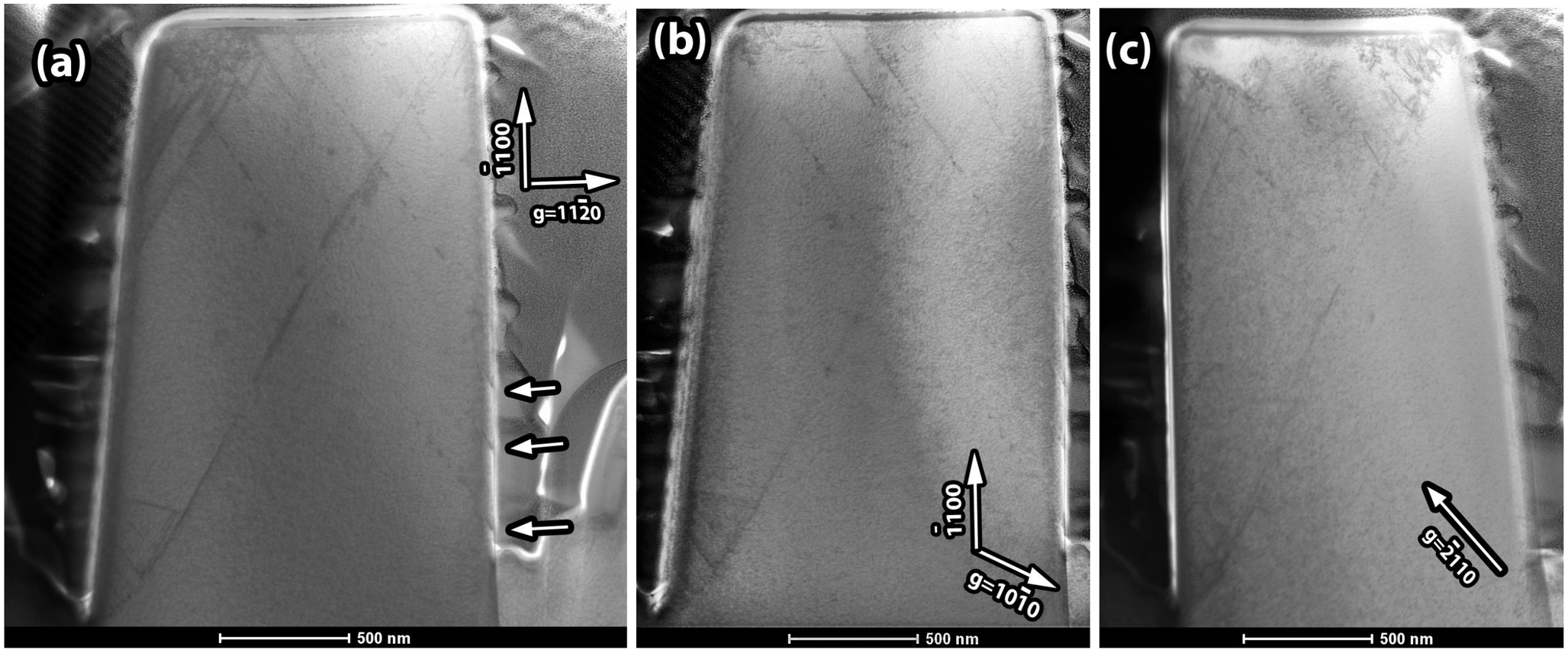

*Figure 6-7 STEM image of the α single phase micro-pillar of 1 μm diameter compressed along [1$\bar{1}$00], (a) B.D.~[0001], g = 11$\bar{2}$0. Two sets of dislocations are visible and their slip planes are edge-on. The slip bands are intermittent but steps generated on both side of side faces of the micro-pillar (as indicated by arrows). (b) B.D.~[0001], **g** = 10$\bar{1}$0. Slip system 1/3[1$\bar{2}$10](10$\bar{1}$0) became invisible (c) B.D.~[01$\bar{1}$2]. g = $\bar{2}$110. The dislocation density in the sample is smaller than the 5 μm diameter micro-pillar in Figure 6-4.*

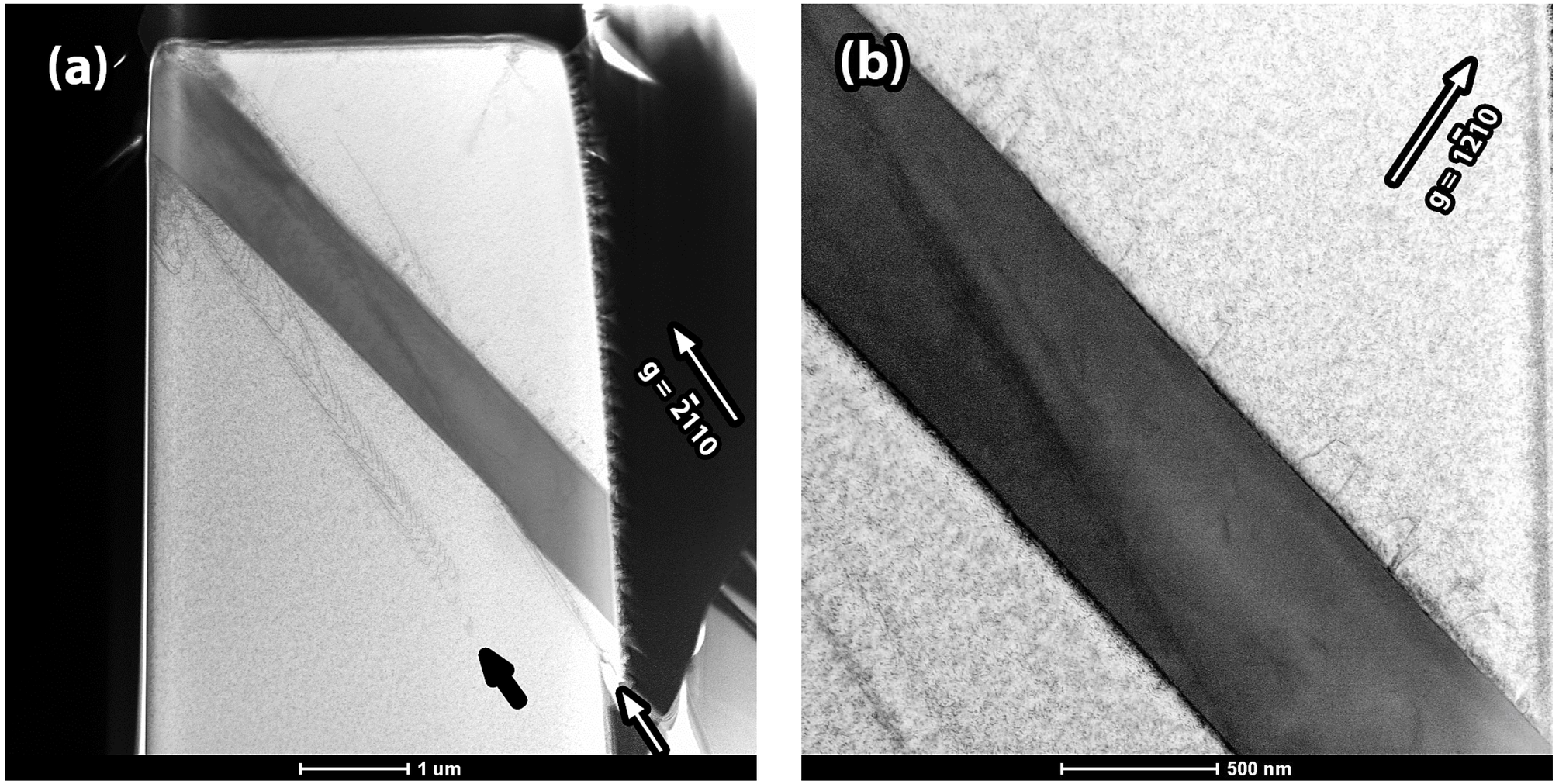

*Figure 6-8 STEM bright field image of micro-pillar obtained from the α/ β micro-pillar of 3 μm diameter compressed along [1$\bar{1}$00]$_{\alpha}$// [10$\bar{1}$]$_{\beta}$. (a) B.D.~[01$\bar{1}$2], **g** = $\bar{2}$110. A set of dislocations original from the top surface sheared the β lath and generated a step on the side surface as indicated by the white arrow. Another set of dislocations original from the downside α/β interface but failed to move through the micro-pillar as indicated by the black arrow. (b) B.D.~[10$\bar{1}$2], **g**= 1$\bar{2}$10. Some dislocations came out from the upside α/β interface.*

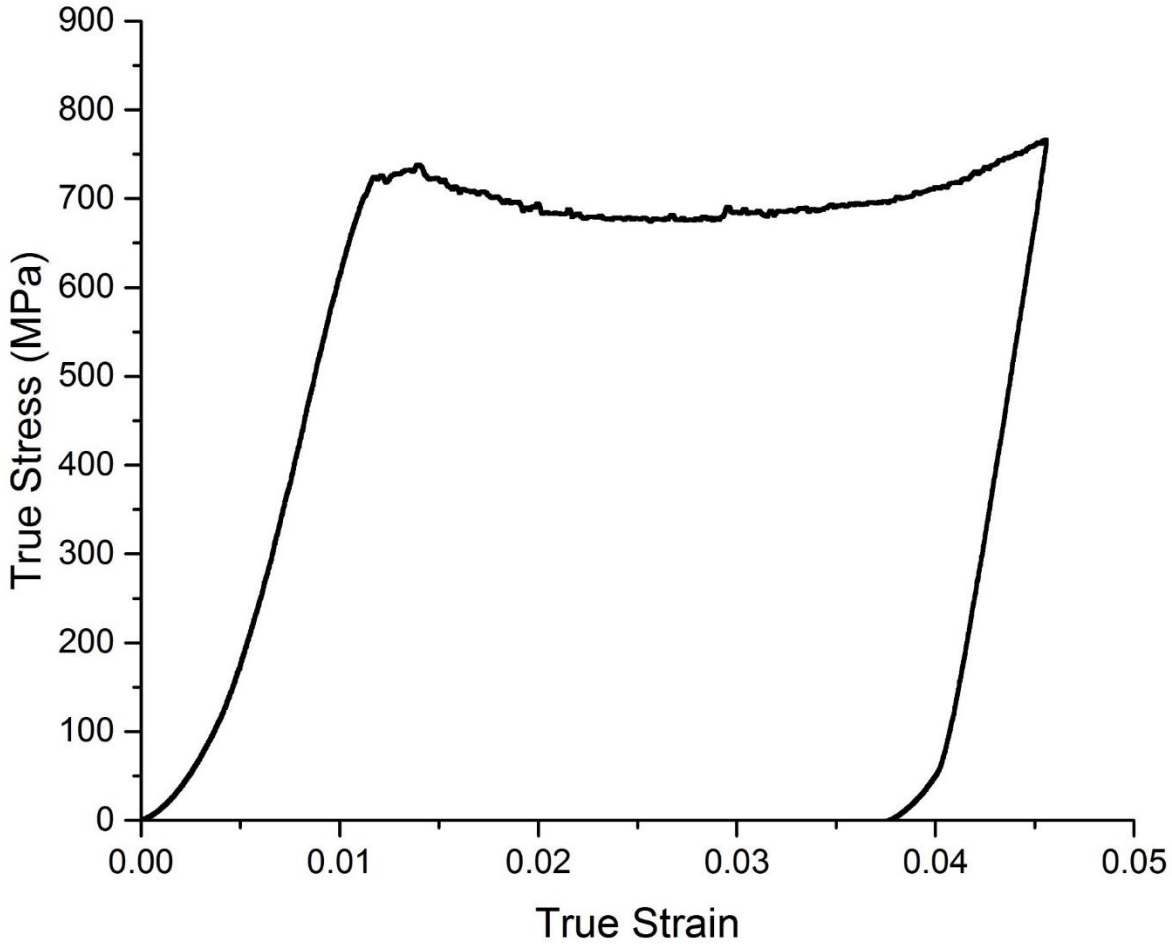

Figure 6-9 The stress-strain curve corresponding to the TEM sample in Figure 6-8

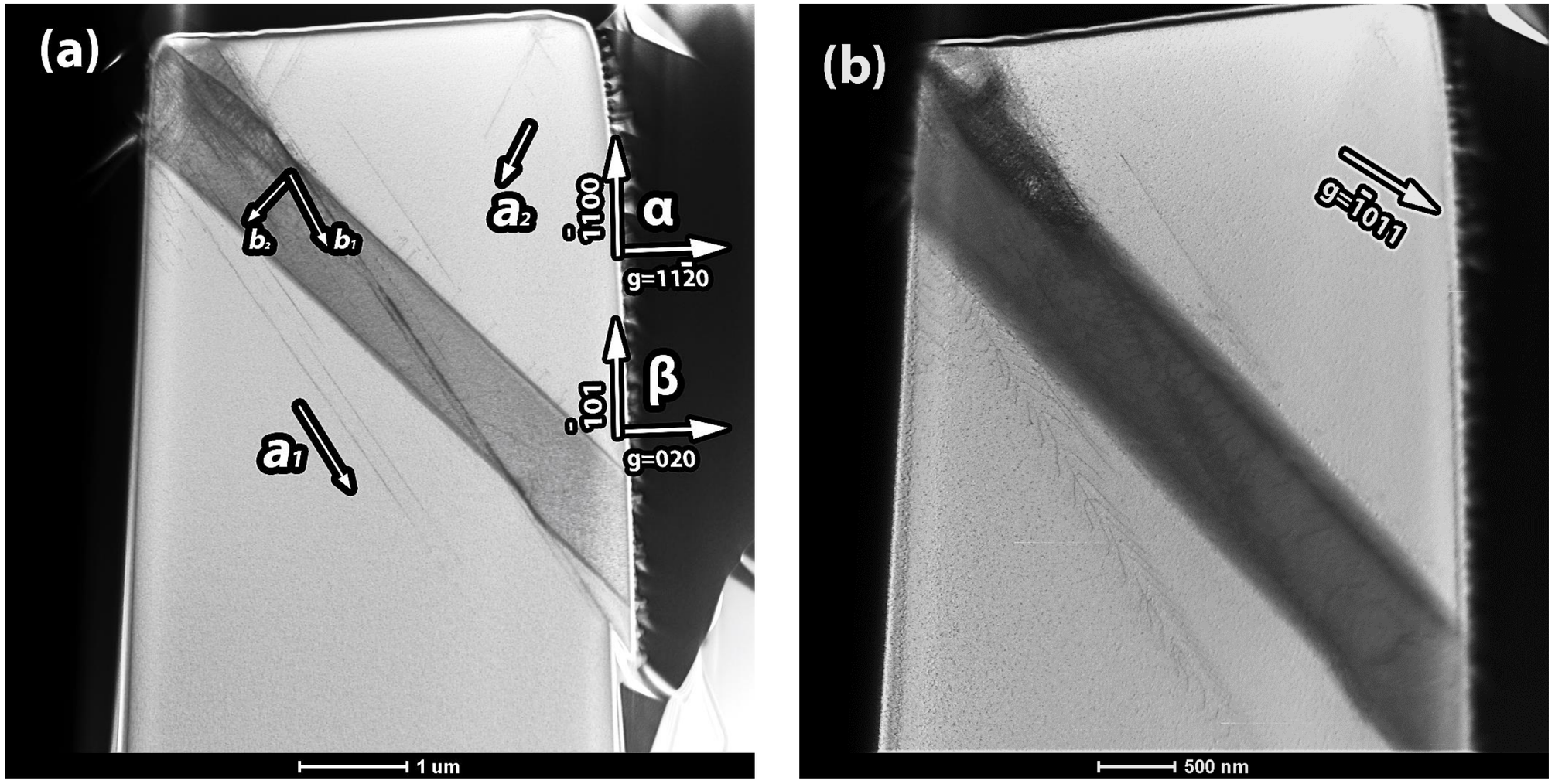

*Figure 6-10 STEM bright field image of micro-pillar obtained from the α/ β micro-pillar of 3 μm diameter compressed along [1$\bar{1}$00]$_\alpha$// [10$\bar{1}$]$_\beta$. (a) B.D.~[0001]$_\alpha$// [101]$_\beta$, g = 11$\bar{2}$0$_\alpha$// 0$\bar{2}$0$_\beta$. **a**$_1$ and **a**$_2$, **b**$_1$ and **b**$_2$ are visible and their slip planes are edge on. (b) B.D.~[$\bar{1}\bar{1}$23], **g**= $\bar{1}$011. **a**$_2$ at the right top corner and the upside α/β interface are invisible.*

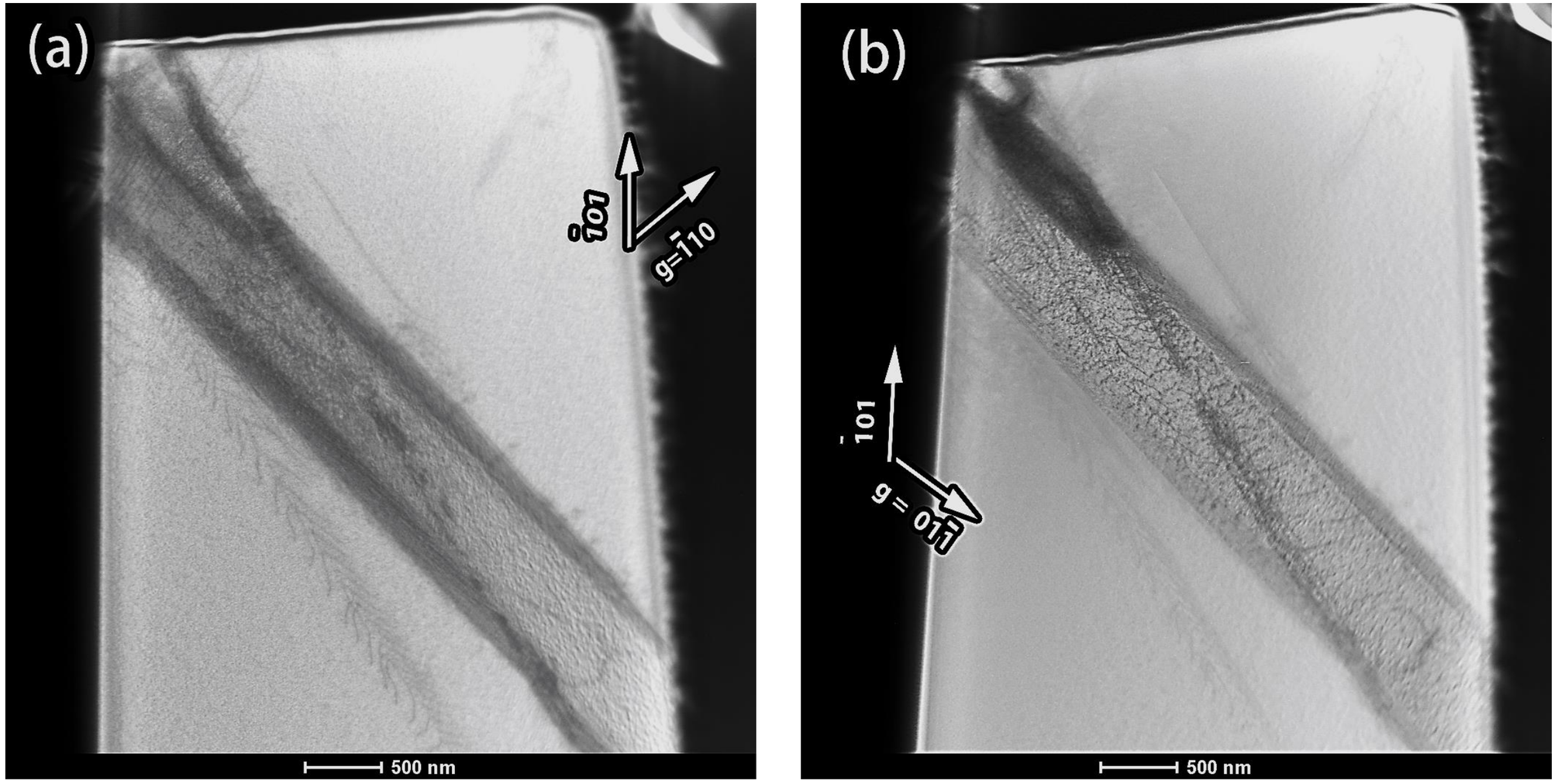

Figure 6-11 STEM bright field image obtained from the α/ β micro-pillar of 3 μm diameter compressed along $[1\bar{1}00]_{\alpha}$ *//* $[10\bar{1}]_{\beta}$ *micro-pillar (a) B.D.~[111],* $\boldsymbol{g} = \bar{1}10$, $\boldsymbol{b}_1$ *is invisible. (b) B.D.~[111],* $\boldsymbol{g} = 01\bar{1}$, $\mathbf{b}_2$ *is invisible.*

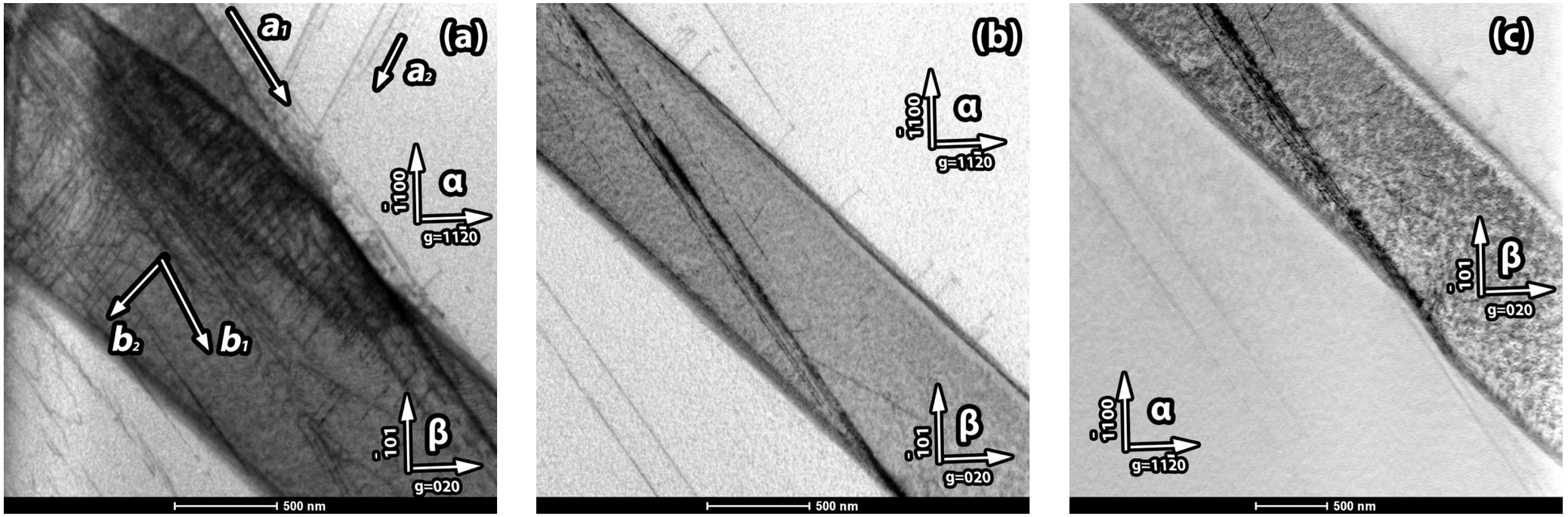

Figure 6-12 Three higher magnification STEM bright field image of Figure 6-10 with same beam condition ([1$\bar{1}$00] α // [10$\bar{1}$] β. B.D.~[0001] α // [101] β, g = 11$\bar{2}$0 α // 0$\bar{2}$0 β). (a) The upper end of the α/β interface. Two sets of dislocations $\mathbf{a_1}$ *and* $\mathbf{a_2}$ *exist in the α phase and two sets of corresponding dislocations* $\mathbf{b_1}$ *and* $\mathbf{b_2}$ *exist in the β phase. (b) The middle of the α/β interface. (c) The bottom end of the α/β interface.*

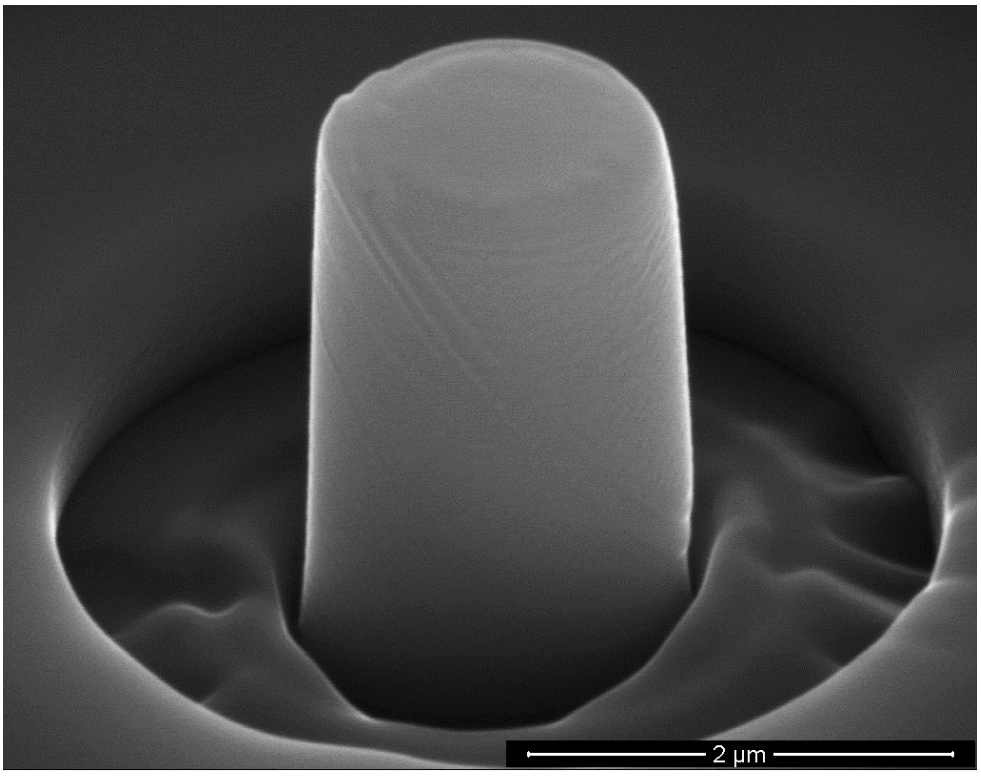

Figure 6-13 The SEM image of the α/β micro-pillar of 1 µm diameter compressed along $[1\bar{1}00]_{\alpha}$ // $[10\bar{1}]_{\beta}$

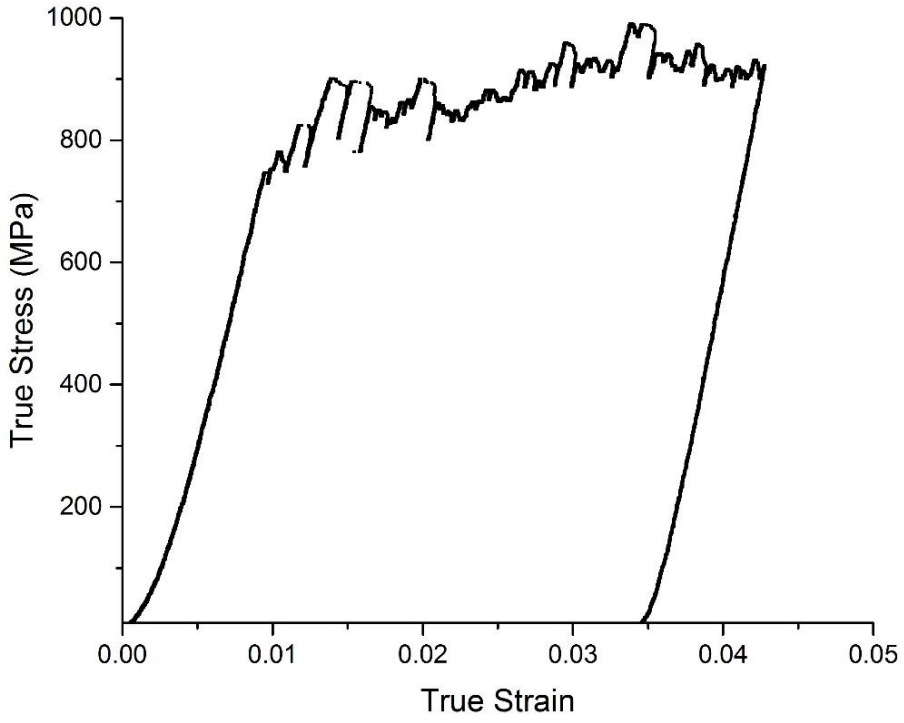

Figure 6-14 The stress-strain curve corresponding to the TEM sample in Figure 6-13

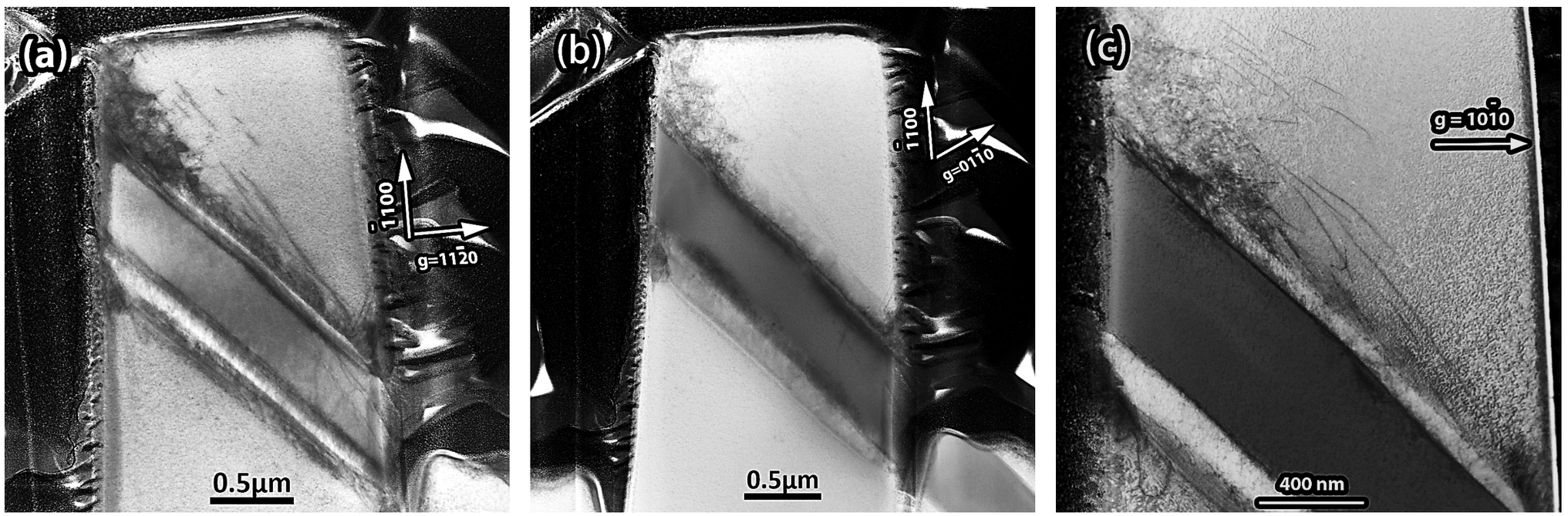

Figure 6-15 The STEM image of the α/β micro-pillar of 1 μm diameter compressed along $[1\bar{1}00]_{\alpha}$ // $[10\bar{1}]_{\beta}$, (a) B.D.~[0001], $\boldsymbol{g}=11\bar{2}0$, $\boldsymbol{a}_1$ prismatic slip plane was edge on. (b) B.D.~[0001], $\boldsymbol{g}=01\bar{1}$, $\boldsymbol{a}_1$ dislocations became invisible.(c)) B.D.~$[1\bar{2}13]$, $\boldsymbol{g}=10\bar{1}0$, $\boldsymbol{a}_1$ dislocations became curved dislocation lines.

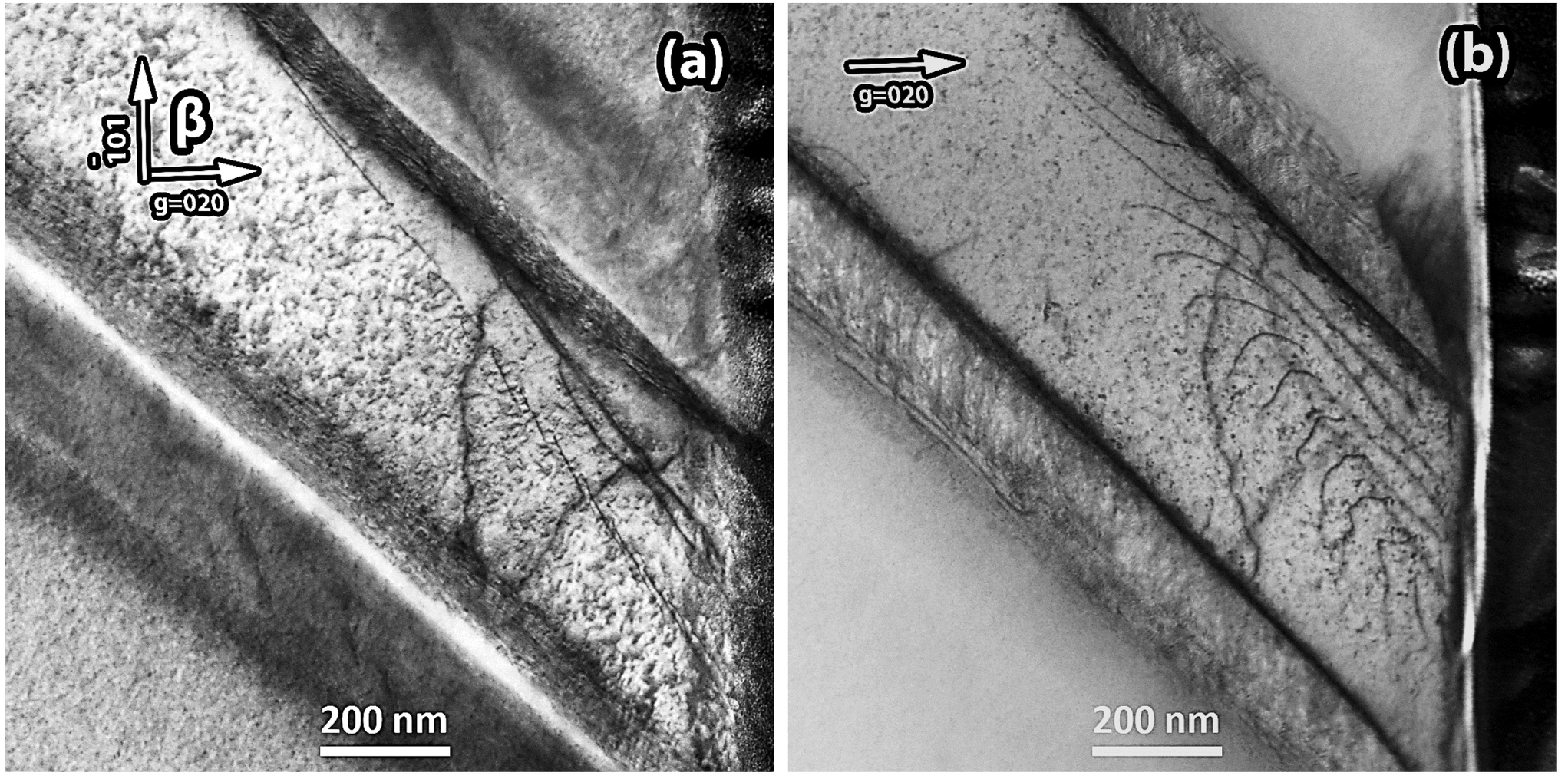

*Figure 6-16 The STEM image of the α/β micro-pillar of 1 μm diameter compressed along $[1\bar{1}00]_{\alpha}$ // $[10\bar{1}]_{\beta}$, (a) B.D.~[101], **g** = 020. The $\mathbf{b}_1$ slip system was edge on. (b) B.D.~[102], **g** = 020. It shows curved dislocation moved from the bottom upwards*

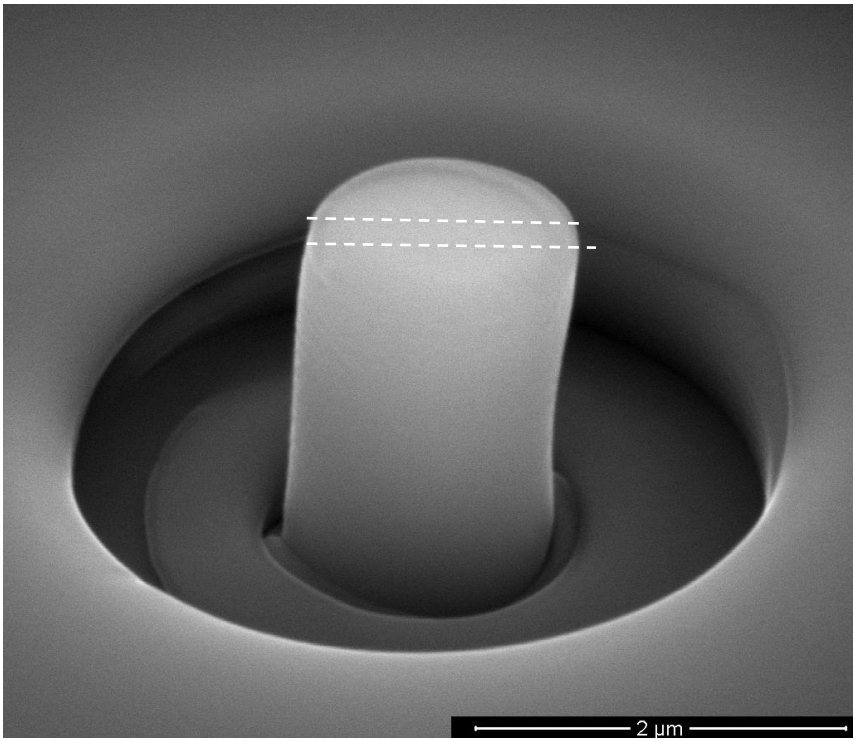

Figure 6-17 The SEM image of the α single phase micro-pillar of 1 μm diameter compressed to 6% strain along [0001] before cutting TEM foil. No slip bands can be observed. The TEM foil was cut along the dashed line.

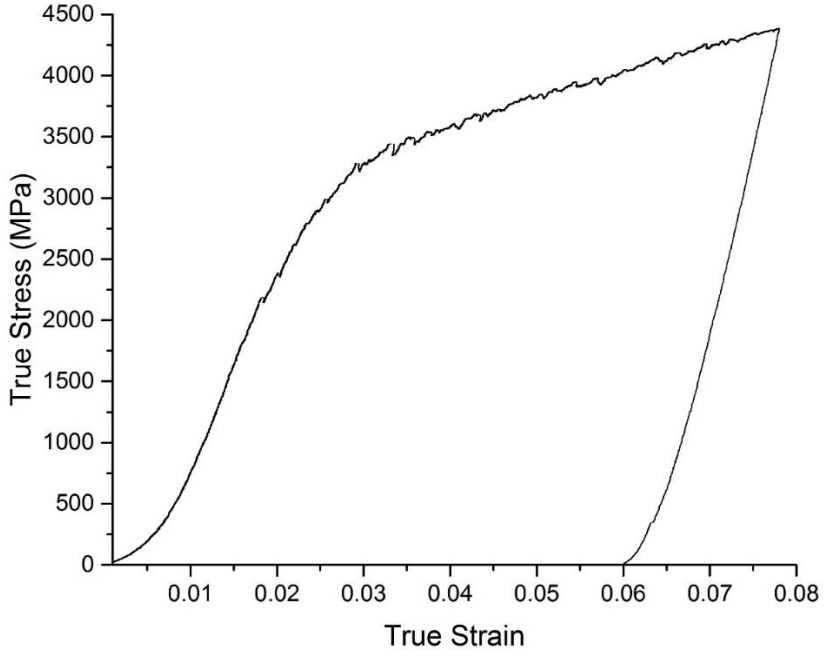

Figure 6-18 The stress-strain curve corresponding to the TEM sample in Figure 6-17

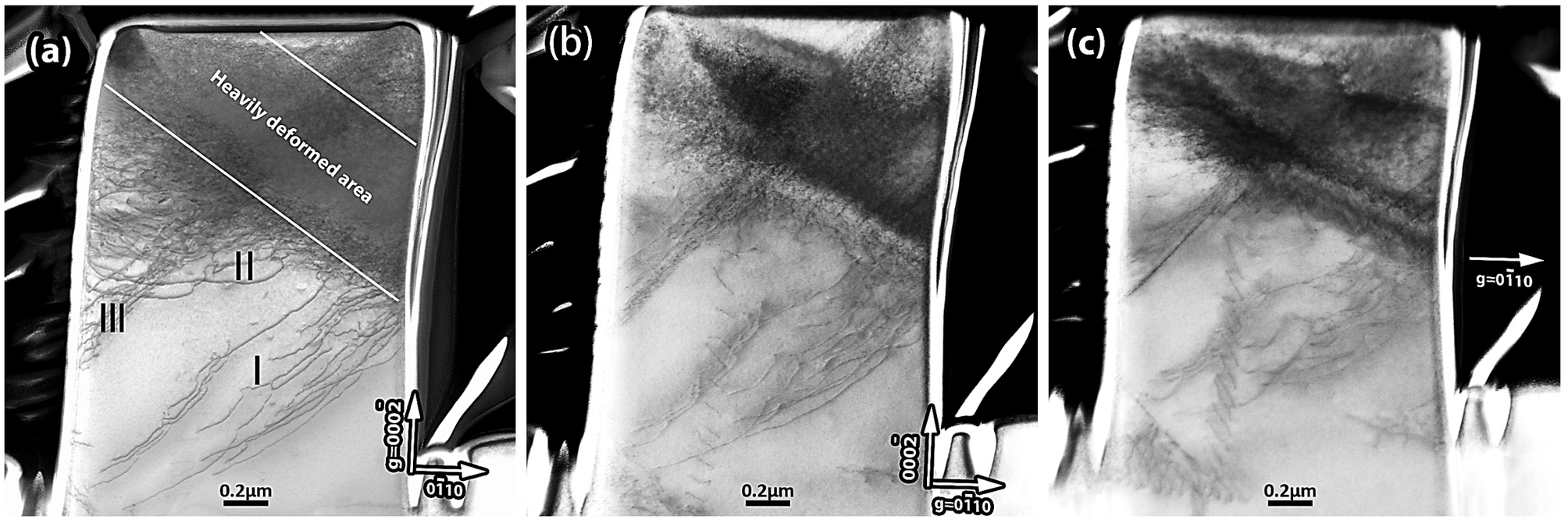

*Figure 6-19 The STEM bright field image of the α single phase micro-pillar of 1 μm diameter compressed to 6% strain along [0001], (a) B.D.~[$2\bar{1}\bar{1}0$], **g** = $000\bar{2}$. Slip system I, II, and III were visible. (b) B.D.~[$2\bar{1}\bar{1}0$], **g** = $0\bar{1}10$, slip system II was invisible, (c) B.D.~[$4\bar{2}\bar{2}\bar{3}$], **g** = $0\bar{1}10$, slip plane of III was edge on. (d) B.D.~ [$1\bar{1}00$], **g**=0002, slip plane of I was edge on (e) B.D.~ [$10\bar{1}0$], **g**=$000\bar{2}$. Slip plane of III was edge on.*

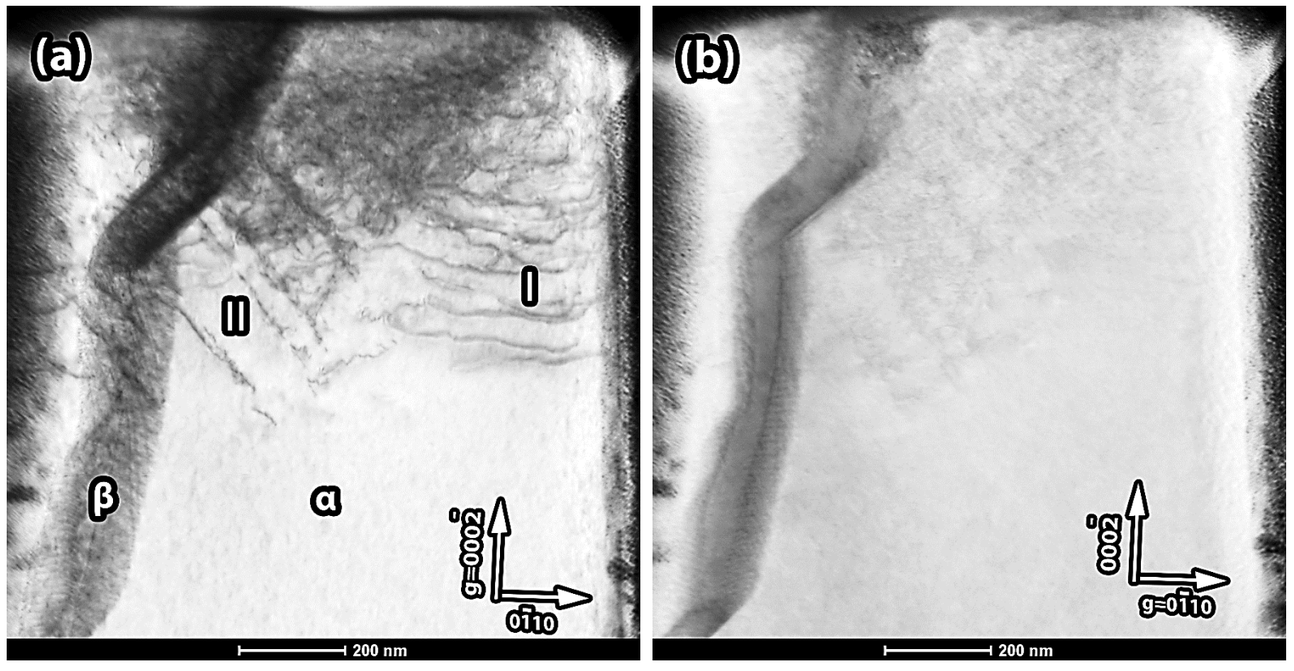

Figure 6-20 The STEM bright field image of the α/β micro-pillar of 1 μm diameter compressed along [0001]$_{\alpha}$ // [101]$_{\beta}$, (a) B.D.~[2$\bar{1}\bar{1}$0], $\boldsymbol{g}$ = 000$\bar{2}$, slip plane of II was edge on (b) B.D.~[2$\bar{1}\bar{1}$0], $\boldsymbol{g}$ = 0$\bar{1}$10, slip plane of I was invisible, (c) B.D.~[$\bar{1}$100], $\boldsymbol{g}$ = 000$\bar{2}$, (d) B.D.~[4$\bar{2}\bar{2}\bar{3}$], $\boldsymbol{g}$ = 1$\bar{1}$02 slip plane of I was edge on.

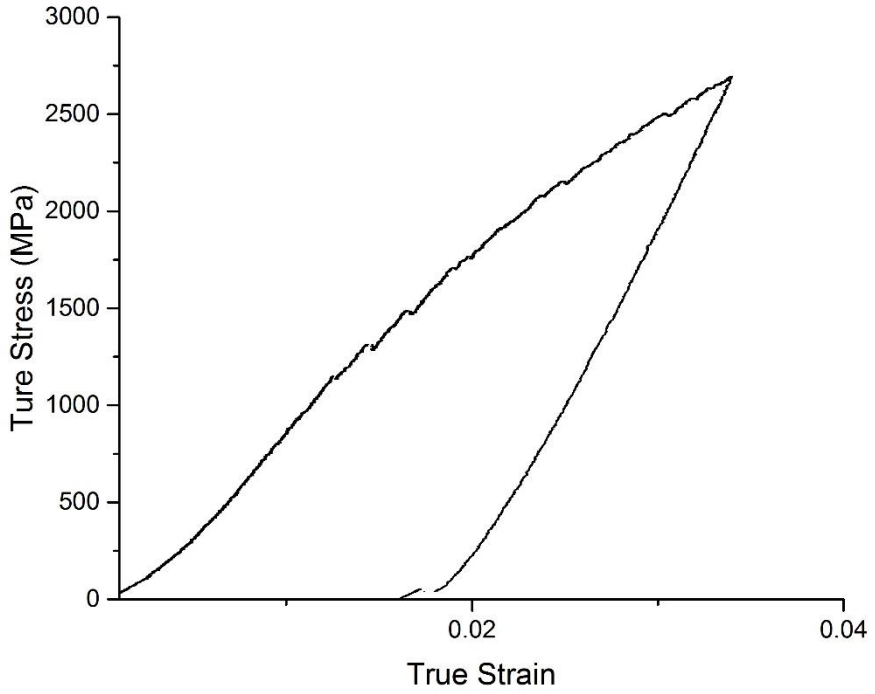

Figure 6-21 The stress-strain curve corresponding to the TEM sample in Figure 6-20

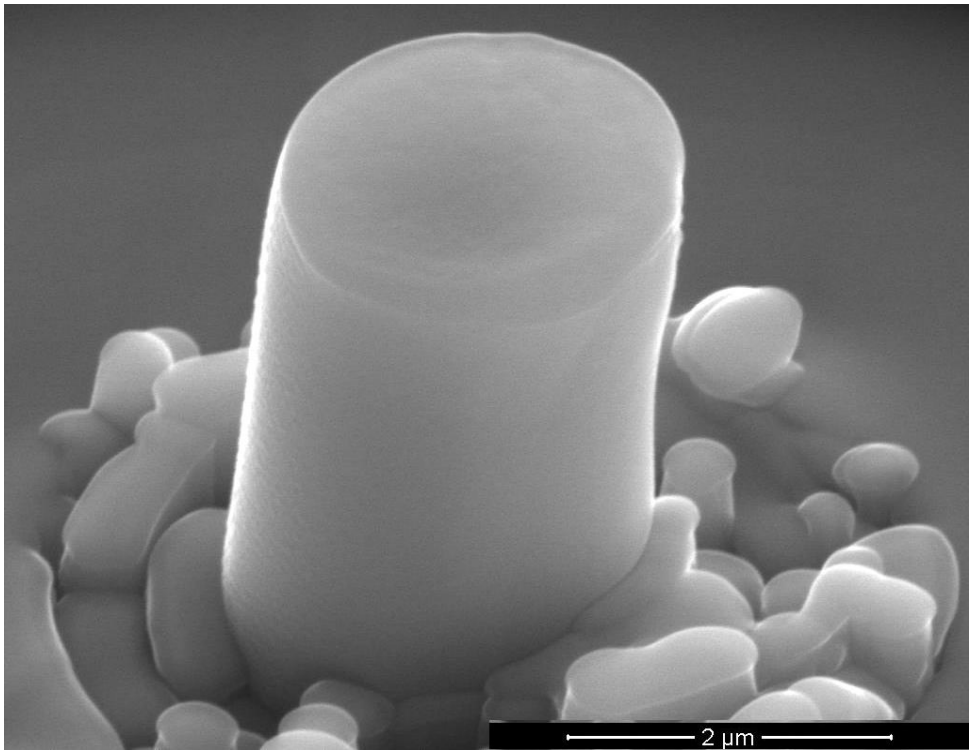

Figure 6-22 The SEM image of the α/β micro-pillar of 2 µm diameter compressed to 6.5% strain along [0001] $_{\alpha}$ *// [101]* $_{\beta}$ *before extracting TEM foil.*

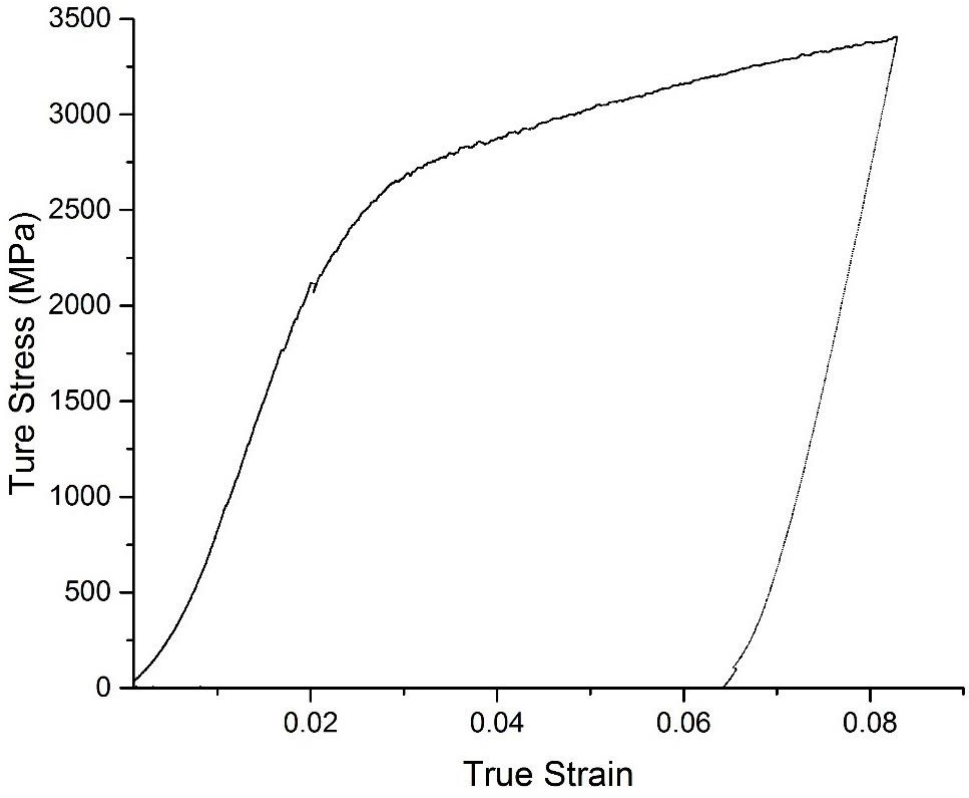

Figure 6-23 The stress-strain curve corresponding to the TEM sample in Figure 6-22

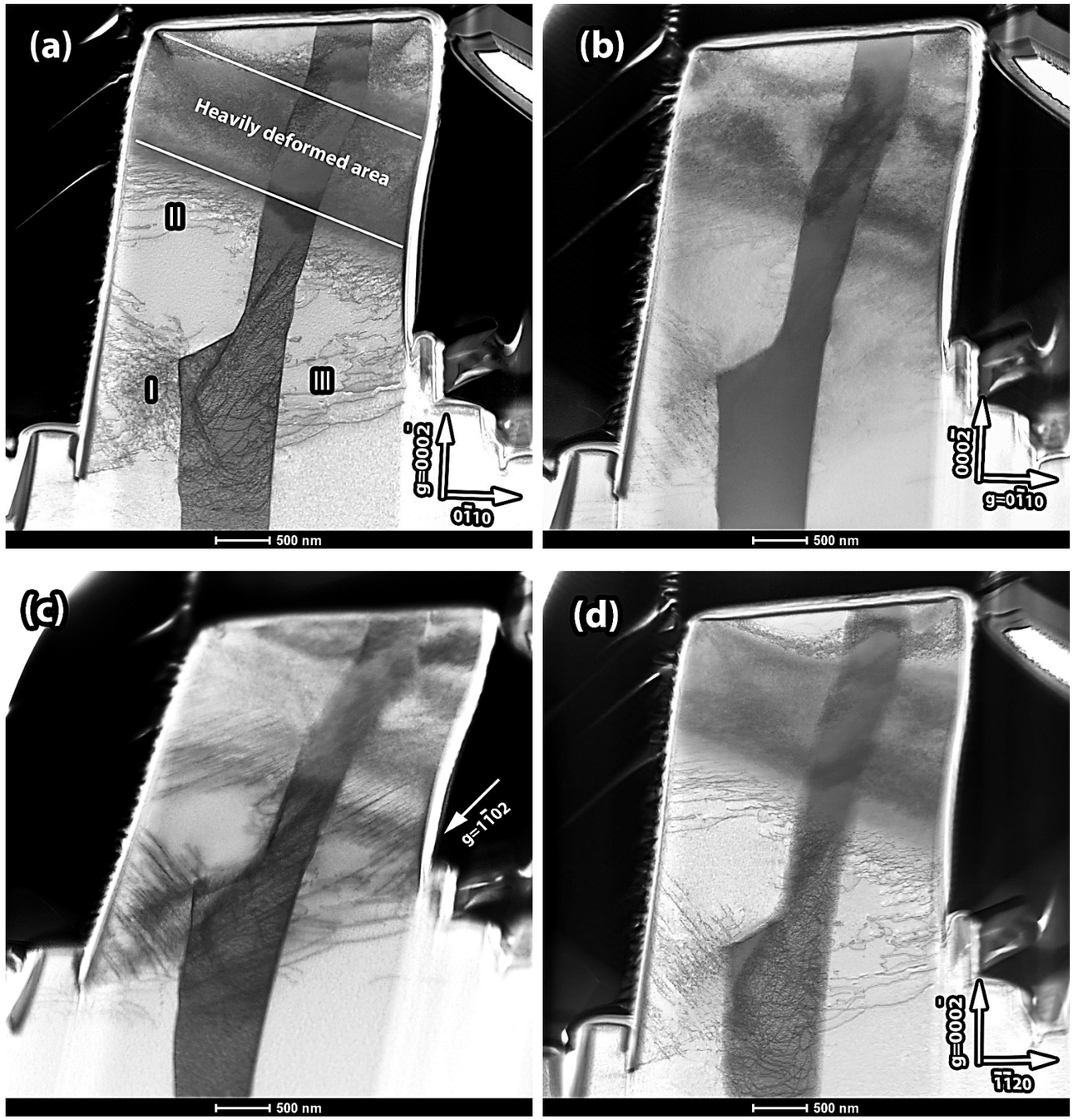

Figure 6-24 The STEM bright field image of the α/β micro-pillar of 2 μm diameter compressed to 6.5% strain along [0001] $_{\alpha}$ *// [101]* $_{\beta}$*, (a) B.D.~[2*$\bar{1}$$\bar{1}$*0], **g** = 000*$\bar{2}$*. Slip system I, II, and III were visible. (b) B.D.~[2*$\bar{1}$$\bar{1}$*0], **g** = 0*$\bar{1}$*10, slip system II was invisible, (c) B.D.~[4*$\bar{2}$$\bar{2}$*3], **g** = 1*$\bar{1}$*02 slip plane of III was edge on. (d) B.D.~ [1*$\bar{1}$*00], **g**=0002, slip plane of I was edge on.*

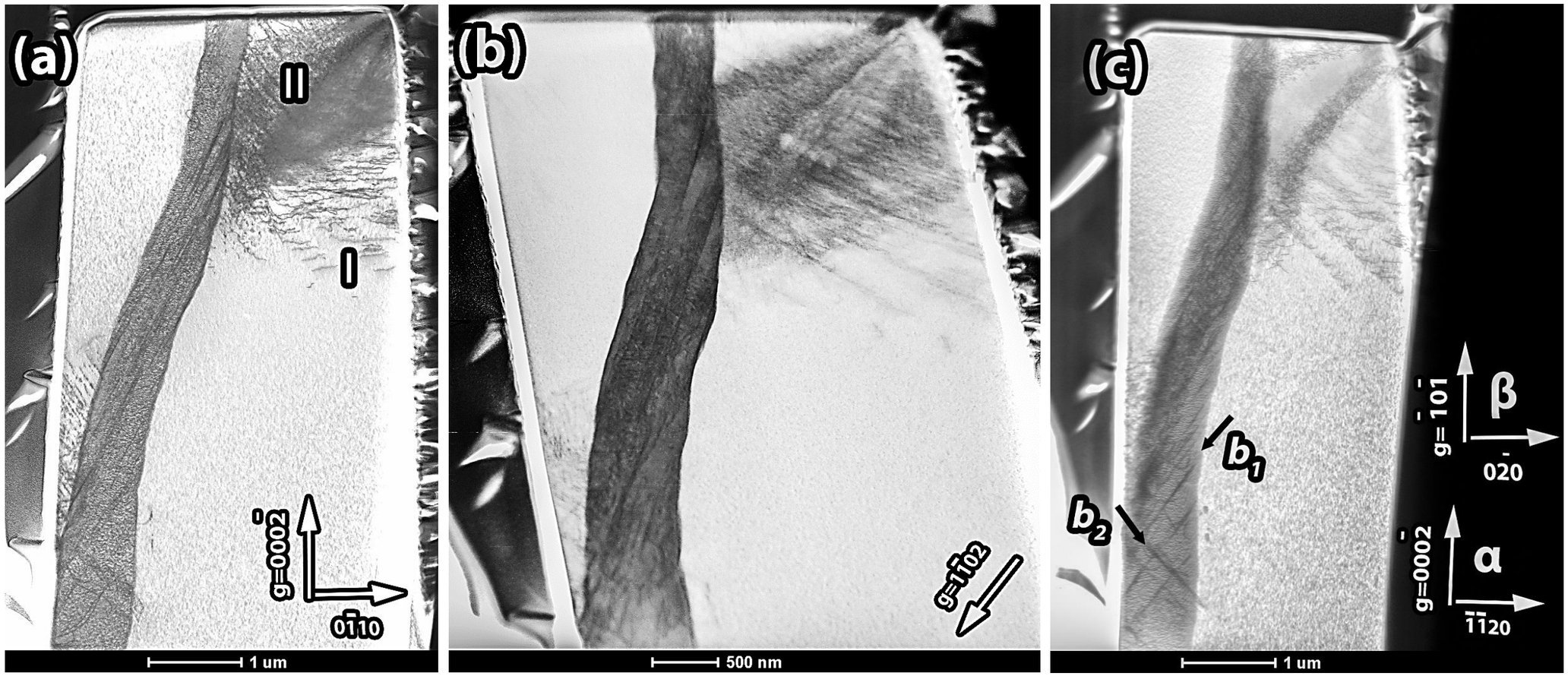

*Figure 6-25 The STEM bright field image of the α/β micro-pillar of 3 μm diameter compressed to 2.5% strain along [0001] α // [101] β, (a) B.D.~ [2$\bar{1}\bar{1}$0] // α // [11$\bar{1}$] β, **g** = 000$\bar{2}$, the dislocations on (01$\bar{1}$1) plane (marked as II) are edge on (b) B.D.~ [4$\bar{2}\bar{2}\bar{3}$], **g** = 1$\bar{1}$02. The dislocations (marked as I) on (11$\bar{2}$2) plane are edge on. (c) B.D.~ [1$\bar{1}$00] α // [10$\bar{1}$] β, **g** = 000$\bar{2}$. Two sets of dislocations in the β phase marked as $\mathbf{b}_1$ and $\mathbf{b}_2$ are edge-on.*

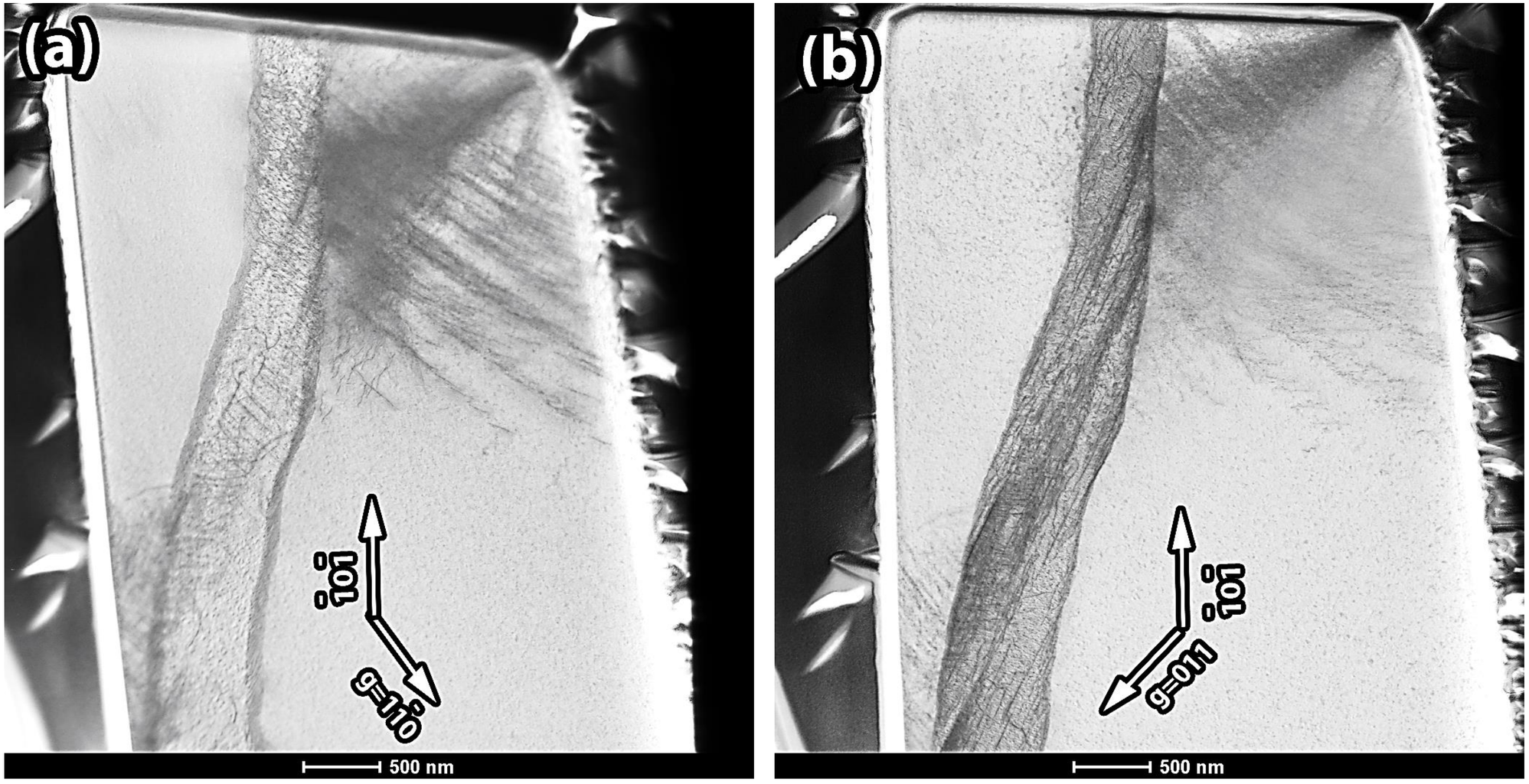

*Figure 6-26 The STEM bright field image of the α/β micro-pillar of 3 μm diameter compressed to 2.5% strain along [0001]$_{\alpha}$// [101]$_{\beta}$, (a) B.D.~ [11$\bar{1}$], **g** = 1$\bar{1}$0. (b) B.D.~ [11$\bar{1}$], **g** =011.*

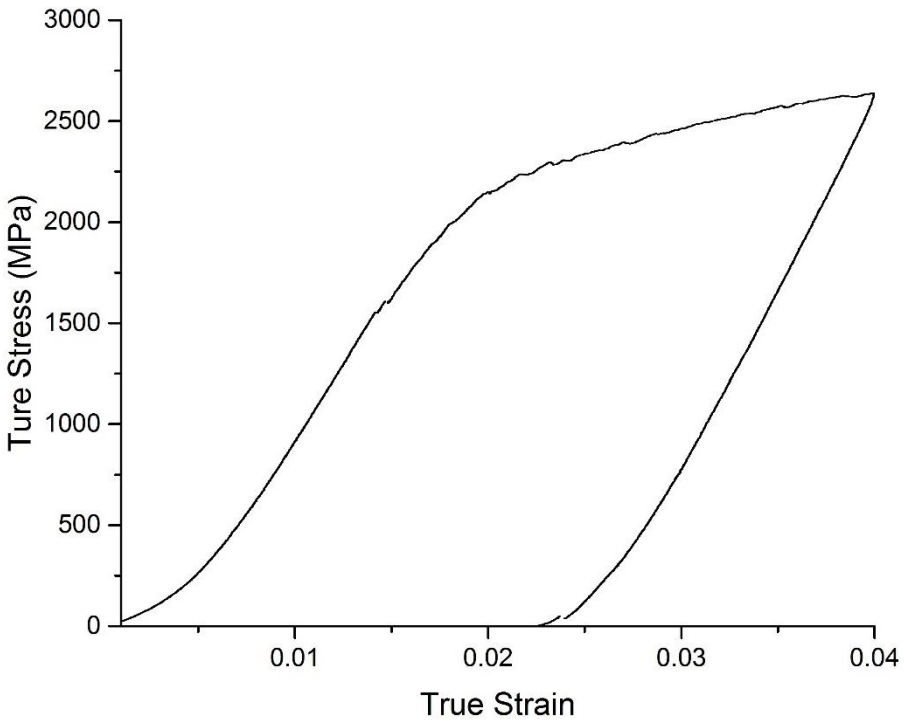

Figure 6-27 The stress-strain curve corresponding to the TEM sample in Section 6.2.4

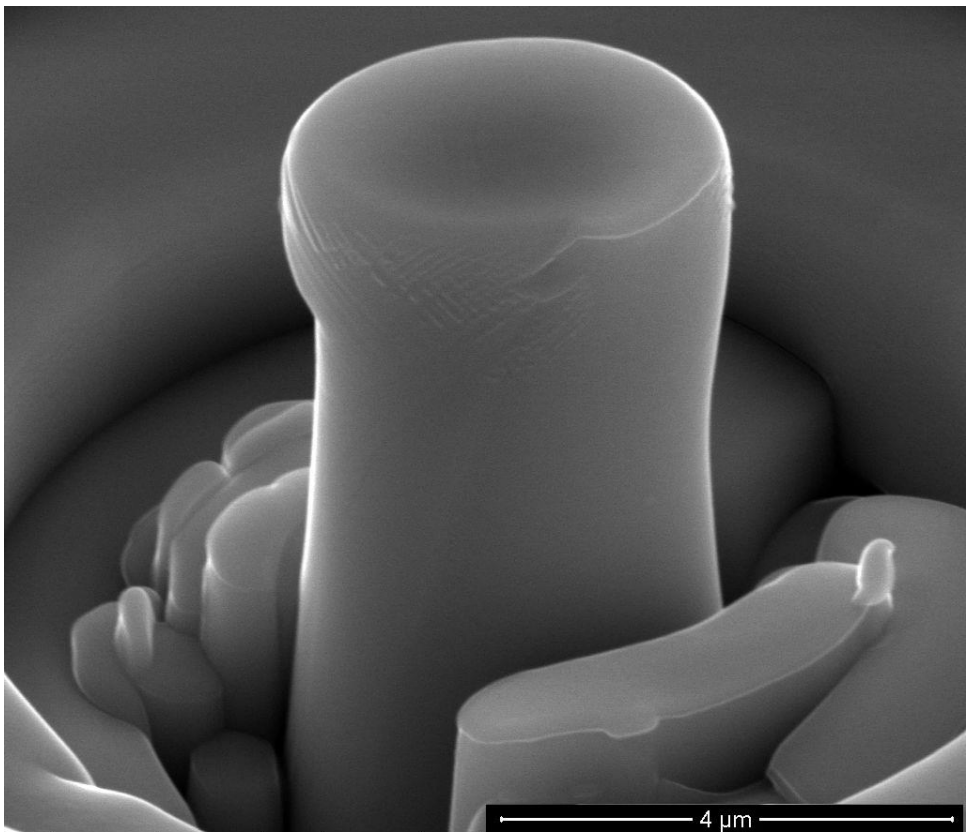

Figure 6-28 The SEM image of micro-pillar containing β phase in the majority of 3 µm diameter compressed to 8% strain along [0001] $_{\alpha}$ *// [101]* $_{\beta}$ *before extracting TEM foil.*

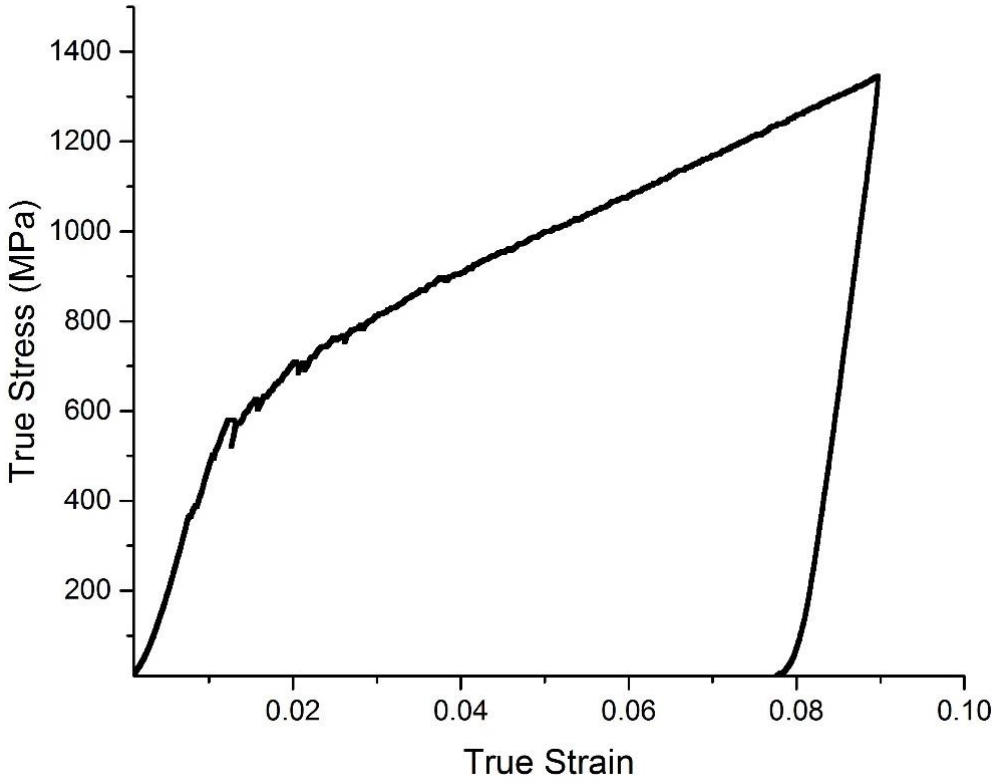

Figure 6-29 The stress-strain curve corresponding to the TEM sample in Figure 6-28

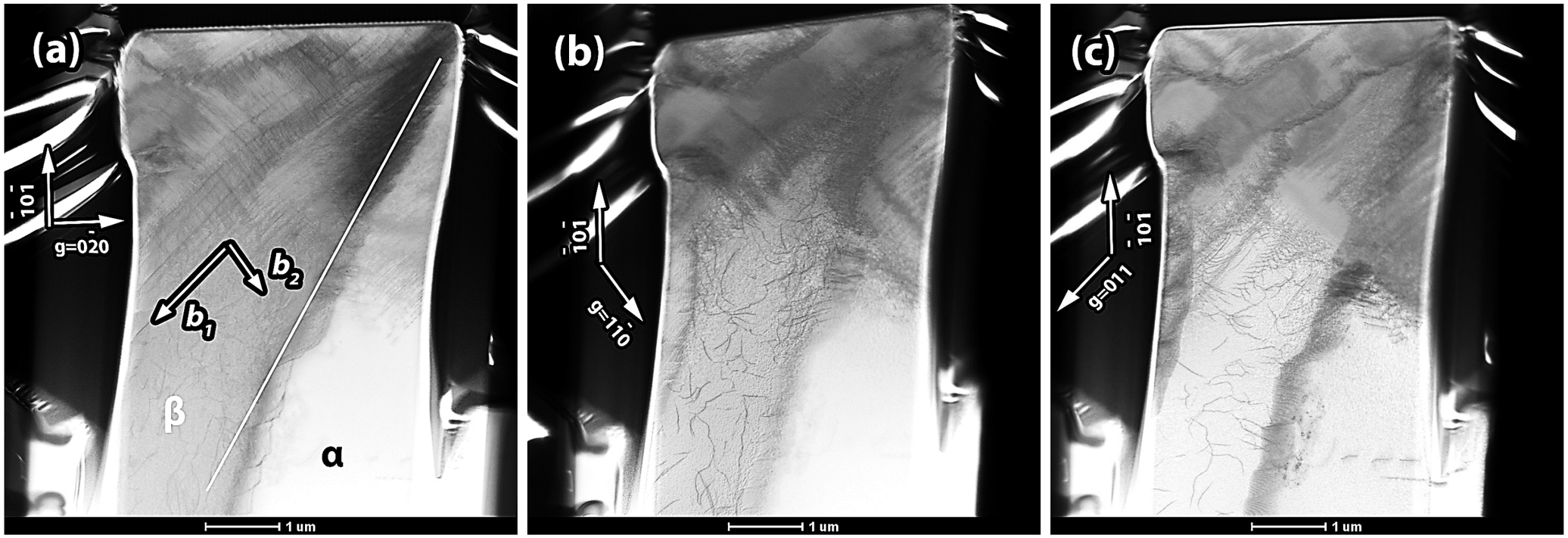

*Figure 6-30 The STEM bright field image of the micro-pillar containing β phase in majority of 3 μm diameter compressed to 8% strain along [0001]$_\alpha$// [101]$_\beta$.. (a) B.D. ~[10$\bar{1}$], **g** = 0$\bar{2}$0. Slip plane of **b**$_1$ and **b**$_2$ were edge on (b) B.D. ~ [11$\bar{1}$], **g** =1$\bar{1}$0. **b**$_1$ dislocations were invisible. (c) B.D. ~[11$\bar{1}$], **g** = 011. **b**$_2$ dislocations were invisible.*

Table 6.1 The diffraction condition of α single phase micro-pillar of 5 μm diameter compressed along [1$\bar{1}$00]

Beam direction	***g***	**prismatic a_1 slip system 1/3[2$\bar{1}\bar{1}$0](0$\bar{1}$10)**	**prismatic a_2 slip system 1/3[1$\bar{2}$10](10$\bar{1}$0)**
[0001]	01$\bar{1}$0	Invisible	Visible (edge-on)
	10$\bar{1}$0	Visible (edge-on)	Invisible
	11$\bar{2}$0	Visible (edge-on)	Visible (edge-on)

Table 6.2 The diffraction and edge on condition of α phase in the α/ β micro-pillar of 3 μm diameter compressed along [1$\bar{1}$00] $_{\alpha}$// [10$\bar{1}$] $_{\beta}$

Beam direction	***g***	**prismatic a_1 slip system 1/3[2$\bar{1}\bar{1}$0](0$\bar{1}$10)**	**prismatic a_2 slip system 1/3[1$\bar{2}$10](10$\bar{1}$0)**
[0001]	11$\bar{2}$0	Visible (edge-on)	Visible (edge-on)
	10$\bar{1}$0	Visible (edge-on)	Invisible

Table 6.3 The diffraction condition of slip systems in β phase in the α/ β micro-pillar of 3 μm diameter compressed along $[1\bar{1}00]_{\alpha}$ // $[10\bar{1}]_{\beta}$

Beam direction	***g***	**1/2 $[11\bar{1}]$ $(\bar{1}21)$**	**1/2 $[1\bar{1}\bar{1}]$ $(12\bar{1})$**
[101]	020	Edge on	Edge on
[111]	$\bar{1}10$	Invisible	Visible
	$01\bar{1}$	Visible	Invisible

Table 6.4 The diffraction condition of slip system in α phase in the α/β micro-pillar of 1 μm diameter compressed along $[1\bar{1}00]_{\alpha}$ // $[10\bar{1}]_{\beta}$

Beam direction	***g***	**prismatic a_1 slip system $1/3[2\bar{1}\bar{1}0](0\bar{1}10)$**
[0001]	$11\bar{2}0$	Visible
	$01\bar{1}0$	Invisible

Table 6.5 The diffraction condition of slip system in β phase in the α/β micro-pillar of 1 μm diameter compressed along $[1\bar{1}00]_{\alpha}$ // $[10\bar{1}]_{\beta}$

Beam direction	***g***	**1/2 $[11\bar{1}]$ $(\bar{1}21)$**
[101]	020	Edge on
[102]	020	Visible

Table 6.6 The diffraction and edge on condition of (partial) slip systems in the α single phase micro-pillar of 1 μm diameter compressed along [0001]

Beam direction	***g***		II		I	III	
		1/3 [$\bar{2}$113] ($2\bar{1}\bar{1}2$)	**1/3 [$2\bar{1}\bar{1}3$] ($\bar{2}$112)**	**1/3 [$\bar{1}\bar{1}23$] ($11\bar{2}2$)**	**1/3 [$11\bar{2}3$] ($\bar{1}\bar{1}22$)**	**1/3 [$\bar{1}2\bar{1}3$] ($1\bar{2}12$)**	**1/3 [$1\bar{2}13$] ($\bar{1}2\bar{1}2$)**
[$2\bar{1}\bar{1}0$]	$000\bar{2}$	Visible	Visible	Visible	Visible	Visible	Visible
	$0\bar{1}10$	**Invisible**	**Invisible**	Visible	Visible	Visible	Visible
[$4\bar{2}\bar{2}3$]	$0\bar{1}10$	**Invisible**	**Invisible**	**Edge on**	Visible	**Edge on**	Visible
[$1\bar{1}00$]	0002	Visible	Visible	**Edge on**	**Edge on**	Visible	Visible
[$10\bar{1}0$]	0002	Visible	Visible	Visible	Visible	**Edge on**	**Edge on**

Table 6.7 The diffraction and edge on condition of slip systems in the α phase in the α/β micro-pillar of 1 μm diameter compressed along [0001] $_{\alpha}$// [101] $_{\beta}$.

Beam direction	***g***	I	II	II
		1/3 [$2\bar{1}\bar{1}3$] ($\bar{2}$112)	**1/3[$1\bar{2}13$] ($01\bar{1}1$)**	**1/3[$\bar{1}\bar{1}23$] ($01\bar{1}1$)**
[$2\bar{1}\bar{1}0$]	$000\bar{2}$	Visible	**Edge on**	**Edge on**
	$0\bar{1}10$	**Invisible**	Visible	Visible
[$4\bar{2}\bar{2}3$]	$1\bar{1}02$	Visible	Visible	Visible
[$\bar{1}100$]	$000\bar{2}$	Visible	Visible	Visible

Table 6.8 The diffraction and edge on condition of slip systems in α phase in the α/β micro-pillar of 2 μm diameter compressed along [0001]$_\alpha$// [101]$_\beta$

Beam direction	***g***	**1/3 [$\bar{2}$113] (2$\bar{1}\bar{1}$2)** III	**1/3 [2$\bar{1}\bar{1}$3] ($\bar{2}$112)**	**1/3 [$\bar{1}\bar{1}$23] (11$\bar{2}$2)** I	**1/3 [11$\bar{2}$3] ($\bar{1}\bar{1}$22)**	**1/3 [$\bar{1}$2$\bar{1}$3] (1$\bar{2}$12)** II	**1/3 [1$\bar{2}$13] ($\bar{1}$2$\bar{1}$2)**
[2$\bar{1}\bar{1}$0]	000$\bar{2}$	Visible	Visible	Visible	Visible	Visible	Visible
	0$\bar{1}$10	**Invisible**	**Invisible**	Visible	Visible	Visible	Visible
[4$\bar{2}\bar{2}\bar{3}$]	1$\bar{1}$02	Visible	Visible	**Edge on**	Visible	**Edge on**	Visible
[1$\bar{1}$00]	0002	Visible	Visible	**Edge on**	**Edge on**	Visible	Visible

Table 6.9 The diffraction and edge on condition of slip systems in the α phase in the α/β micro-pillar of 3 μm diameter compressed along [0001]$_\alpha$// [101]$_\beta$

Beam direction	***g***	I **1/3 [$\bar{1}\bar{1}$23] (11$\bar{2}$2)**	II **1/3[1$\bar{2}$13] (01$\bar{1}$1)**	II **1/3[$\bar{1}\bar{1}$23] (01$\bar{1}$1)**
[2$\bar{1}\bar{1}$0]	000$\bar{2}$	Visible	**Edge on**	**Edge on**
[4$\bar{2}\bar{2}\bar{3}$]	1$\bar{1}$02	**Edge on**	Visible	Visible
[1$\bar{1}$00]	000$\bar{2}$	Visible	Visible	Visible

Table 6.10 The diffraction and edge on condition of slip systems β phase in the α/β micro-pillar of 3 μm diameter compressed along [0001]$_\alpha$ // [101]$_\beta$

Beam direction	***g***	**Slip system 1/2[111](1$\bar{2}$1)**	**Slip system 1/2[1$\bar{1}$1](121)**
[10$\bar{1}$]	$\bar{1}0\bar{1}$	Edge on	Edge on
[11$\bar{1}$]	$1\bar{1}0$	Invisible	Visible
	011	Visible	Invisible

Table 6.11 The diffraction and edge on condition of slip systems in the micro-pillar containing β phase in majority of 3 μm diameter compressed along [0001]$_\alpha$ // [101]$_\beta$

Beam direction	***g***	**Slip system 1/2[111](1$\bar{2}$1)**	**Slip system 1/2[1$\bar{1}$1](121)**
[10$\bar{1}$]	$0\bar{2}0$	Edge on	Edge on
[11$\bar{1}$]	$1\bar{1}0$	Invisible	Visible
	011	Visible	Invisible

Chapter 7 Discussion

For the sake of simplicity of discussion, the micro-pillars are named in the following groups:

- Group 1 (G1): α single phase micro-pillars compressed along $[1\bar{1}00]$ of diameters ranging from 0.5 to 5 μm.
- Group 2 (G2): α/β micro-pillars compressed along $[1\bar{1}00]_{\alpha}$ // $[10\bar{1}]_{\beta}$ of diameters ranging from 1 to 5 μm.
- Group 3 (G3): α single phase micro-pillars compressed along [0001] of diameters ranging from 0.5 to 5 μm.
- Group 4 (G4): α/β micro-pillars compressed along $[0001]_{\alpha}$ // $[101]_{\beta}$ of diameters ranging from 1 to 5 μm.
- Group 5 (G5): α/β micro-pillars containing large volume fraction of β phase compressed along $[0001]_{\alpha}$ // $[101]_{\beta}$ of diameters 3 μm.

7.1 β phase and α/β interfaces effects on the strength

Before the discussion of the strength measured and its relationship with the β phase and α/β interfaces, the morphologies and constitutions of phases in the micro-pillars and the difference induced in these groups of micro-pillars should be clarified first, as these differences are the main reasons for the different strength values measured between this thesis and other literature [10, 52, 84] when β phase and α/β interfaces are introduced.

7.1.1 Micro-pillars compressed along $[1\bar{1}00]_{\alpha}$ // $[10\bar{1}]_{\beta}$

To show the difference, the CRSS values measured in this thesis and literature [84] are plotted in Figure 7-1. In the present work, the $\boldsymbol{a}_1$ prismatic slip is the predominant slip system observed in the α phase in both G1 and G2 micro-pillars. G1 are the single α micro-pillars which are comparable with the Ti-6Al micro-cantilever sample [84]. Because of the symmetry of $\boldsymbol{a}_1$, $\boldsymbol{a}_2$ and $\boldsymbol{a}_3$ in the α phase, the CRSS values for $\boldsymbol{a}_1$ and $\boldsymbol{a}_3$ should be similar, which is proved in Figure 7-1. However, the results of G2 show the difference. G2 are the micro-pillars with the structure that top and bottom are α and a β layer in the middle, which are comparable with the Ti-6Al micro-cantilever sample [84]. As shown in Figure 7-1, the CRSS of $\boldsymbol{a}_3$ prismatic slip in Ti-6Al-4V increased from about 483 MPa to 752 MPa when the cantilever width reduced from 5 μm to 1 μm, which is higher than CRSS measured from Ti-6Al (347 MPa at 5 μm and 612 MPa at 1 μm). On the contrary, the CRSS of $\boldsymbol{a}_1$ prismatic slip in Ti-6Al-4V increased from about 300 MPa to 356 MPa when the cantilever width reduced from 5 μm to 1 μm, which is lower than CRSS measured from Ti-6Al [84]. The literature conclusion that Ti-6Al-4V samples orientated for the for the $\boldsymbol{a}_3$ prismatic slip have much higher CRSS values than the single α phase alloys (both CP-Ti and Ti-6Al) with the sample sizes between 1 μm and 10 μm did not count in the influence of β phase as its volume fraction is low and it could be negligible. They attributed this trend to the interface barrier effect for $\boldsymbol{a}_3$ prismatic slip [51]. However, even though the interface provides hardly any barrier effect for $\boldsymbol{a}_1$ prismatic slip, no literature shows the interfaces lead to lower CRSS values. Compared with the β phase in the bulk samples or micro-samples (e.g. as mentioned in the literature [84]), it is a different situation in this

thesis that the β layer is relatively thick (~30% volume fraction in G2) and its influence cannot be negligible. In [$1\bar{1}00$] loading direction, the single α micro-pillar of 3 μm diameter has an average yield stress of 724 MPa, which is larger than the 595 MPa average yield stress of the micro-pillar containing a β fillet of the same diameter. In G5, as the slip system activated in the β phase belongs to the same family as the slip system activated in G2, and the 615 MPa average yield stress measured in G5 is close to the value measured in G2. Therefore, when a micro-pillar in G2 with such the structure was compressed, the β phase yields first as the β phase is weaker than the α phase. In other words, the yield stress measured in G2 is also the yield stress for the β phase in this orientation. After the yield, as the dislocation analysis in the micro-pillar in Section 6.1.3, the α/β interface limited a certain amount of dislocations within their own original phases. It leads to an increase of dislocation densities and therefore forest hardening in the micro-pillars [80]. However, as shown in Figure 6-8, the interfaces inside the micro-pillar provided additional adequate dislocation sources compared with the micro-pillars without α/β interfaces. A large number of dislocations breeding from the interfaces during plastic flow can weaken the micro-pillar [114]. Therefore, the role of α/β interface cannot be straightforwardly defined as strengthening or weakening as both effects exist for α/β interfaces. However, considering together with the weakening effect of the β phase, they exhibit overall weakening effect in the stress-strain curves of the micro-pillars in this group.

7.1.2 Micro-pillars compressed along [0001]$_\alpha$ // [101]$_\beta$

Unlike numbers of reports on the <***a***> slips, few data [10, 91] have been reported on the <***c+a***> slips in the Ti alloys micro-scale samples and can be used to compare

with G3 and G4. For example, the micro-scale samples in literature [10, 91] are with the 1st order pyramidal <***c+a***> slips activated. G3 are the single α micro-pillars with the 2nd order pyramidal <***c+a***> slips activated. G4 are micro-pillars with both the 1st and the 2nd order pyramidal <***c+a***> slips activated. The micro-pillars in this group have the structure that left and right side are α and a β layer is in the middle. In the micro-pillar with this structure, the α and β share the stress and yield at the same time during compression. However, when the micro-pillars were compressed along [0001], which is a stronger loading direction for h.c.p. crystal structure than the $[1\bar{1}00]$ while the strength of β phase should be the same as slip systems activated in G2 and G4 belong to the same family. Therefore, the weakening effect of β phase is more obvious. In the results in Figure 7-3, the degree of weakening effect from β phase is related with the volume fraction of β in the micro-pillars. The micro-pillars of 3 μm diameter have yield stress around 2394 MPa, while the pillars containing thin β fillet between two α have lower yield stress around 1745 MPa. The micro-pillar containing β majority has yield stress only around 621 MPa. This value is very close to the yield stress of 3 μm diameter α/β micropillars compressed along $[1\bar{1}00]$. As the dislocation analysis in Chapter 6 proved, the β phase slip systems activated in micro-pillars compressed along $[1\bar{1}00]$ and [0001] orientations are from the same family and have the same Schmid factor. Based on the yield stress and calculated Schmid factor in Table 4.3, the CRSS for $1/2[11\bar{1}]$ $(\bar{1}21)$ slip system in the β phase micro-pillar of 3 μm diameter is 280 MPa – 292 MPa. This value is smaller than the CRSS value for <***a***> prismatic 383 MPa and <***c+a***> the 2nd order pyramidal 1026 MPa in the micro-pillar with the same diameter. This coincidence confirmed that β phase is softer than α phase no matter along $[1\bar{1}00]$ or [0001]

loading direction. Therefore, the G4 is expected to have the yield stress values between that for G3 and G5 which is proved by the stress-strain curves in Figure 7-3.

In summary, the micro-pillars show different strength based on the orientation and the morphology of the β phase and α/β interfaces within the micro-pillars. Controlling the β phase and α/β interfaces could be an important factor for controlling the strength of micro-scale samples and therefore improving the material properties in the future.

7.2 Sample size effect on the strength

After clarifying the influence of the β phase and α/β interfaces, the sample size effect and be discussed without influence by other factors. To describe the sample size effects on strength of G1, G2, G3 and G4 pillars, the relationship between their yield strength and diameters are plotted using the values based on the Equation 3.6, and their bulk sample yield strength was taken from literature listed in Table 3.1. The size effects on strength are summarized and shown in Figure 7-2 which is a log-log plot of the diameter of micro-pillars and the yield stresses. In Figure 7-2, the exponent of the power law fitting n is 0.61and 0.55 for G1 and G2 pillars, respectively. These values are close to the n = 0.5 reported in micro-cantilevers oriented for prismatic <***a***> slip in titanium micro-pillars [92] and these values also agree with the report [14] that size effect between CRSS and micro-cantilever width in polycrystalline samples have smaller n value than single phase samples (0.29 for single α and 0.21 for α+β micro-cantilever). For G3 and G4 pillars, the sample size effects are much less significant with the n values 0.12 and 0.11 respectively. Several points of interesting between these groups of results will be discussed

below.

7.2.1 Orientation perspective

From a perspective, the reason for different sample size effect could be discussed based on the orientations, as the effect of orientation on the yield strength measured in single α phase micro-pillars is mainly due to the activation of the difference of slip systems, similar to that reported in the bulk sample [24]. In Figure 7-2, the scaling exponents *n* show G1 has a more prominent sample size effect than G3. Similar results have been obtained when beta phase was included in the sample (i.e. G2 and G4). G2 has a larger scaling exponent than G4. This trend can be explained by the different dislocation densities in a different orientation. In micro-pillars in G1 and G2, the dislocations densities are much lower than micro-pillars in G3 and G3 at the same strain level. This is caused by the fewer slip systems (dominant $\boldsymbol{a_1}$ prismatic slip system with few $\boldsymbol{a_2}$ prismatic slip system) activated in the micro-pillars in G1 and G2 than the number of slip systems (usually more than 3 sets of <***c+a***> slip systems) in micro-pillars in G3 and G4. Therefore, based on the explanation of sample size effect exponent *n* as mentioned in literature [94], the mechanism of dislocation source activation was dominant in G1 and G2 compared with the mechanism of dislocation forest hardening or dislocation multiplication in G3 and G4. According to Equation 3-7, micro-pillars controlled by dislocation forest hardening usually reveal the weaker sample size effect than the dislocation source activation [94], due to the low effective dislocations nucleation rate α. As the STEM images indicated in section 6.1, in G1, or G2, when sample diameters decreased, the dislocation density left in the micro-pillars clearly decreased. There

are not many barriers on their way to escape. To continue the plastic deformation, multiple slip bands generated from new sources which increased the stress needed. However, in the STEM images of G3 and G4 in Section 6.2, even though there is also a trend of dislocation density decrease with micro-pillar diameter, the dislocations were still intertwined in the micro-pillar and it may not stop them sliding to sample surface. There is also no evidence showing the new dislocations sources. Therefore, the micro-pillars with <***c+a***> type slips activated has a lower scale of size effect.

7.2.2 The β phase and α/β interface perspective

The influence of the β phase and α/β interface has been observed in literature [84] but without any explanation. Generally, it can be described as the β phase and α/β interface can reduce the size effect exponent *n*. Similar difference of sample size effect caused by the effects of β phase and α/β interface between G1/G2 or G3/G4 were observed in the current work. Combining the TEM observation, the reason was explained as follow. When micro-pillar size decreased, the effect of β phase weakening effect is not changed as its volume percentage was controlled relatively constant in G2/G4. The strengthening effect of the α/β interface is not changed as it still blocked the way of dislocations slide along some orientations. However, the weakening effect of α/β interface was reduced in G2 as the length of interfaces decreased with the sample size decreased, which means the interfaces provide dislocation sources than that in the micro-pillars of larger diameter. This change can be seen that in Figure 6-16 the dislocations generated in β phase was from the micro-pillar side surface instead of α/β interface, and in Figure 6-20 there is no evidence

shown dislocations originated from α/β interface. Because the weakening effect was reduced, the G2 showed smaller size effect scale than G1. However, this situation does not exist between G3 and G4. That is explained why not much difference on the size effect scales between these two groups of micro-pillars.

7.3 Work hardening

In the literature, there is not a clear definition on the "strength" researchers used when they studied the sample size effect on the strength. CRSS [84] or flow stress at a large strain level such as 7.5% strain [85] were used in different researches. Theoretically, the latter results should be affected by the different work-hardening rates and then shown different conclusions from the former. When discussing size effect, choosing the flow stress at different strain can get different scales of size effect.

For example, the different changes in work hardening rates with sample sizes between G1 and G2 as Figure 7-4 shows. In Figure 7-4 (a), the work hardening rate decreased from 5.33 GPa to -4.65 GPa when micro-pillar diameters reduced from 5 μm to 0.5 μm. Although the size effect strengthened the yield stress at the beginning, the work-hardening rates decreased to negative with the micro-pillar diameter decreased. Inversely in Figure 7-4 (b), the work hardening rate increased from -5.33 GPa to 10.24 GPa when micro-pillar diameters reduced from 5 μm to 0.5 μm. Similar trends can be found in the literature on the sample size effect in CP-Ti micro-pillars [92] and Ti-6Al-4V micro-cantilevers [84] but not much words mentioned the work-hardening difference between the stress-strain curves. Based on the TEM analysis in section 6.1.1 and 6.1.2, the difference can be explained by

that the dislocations can escape to the free surface easily in the smaller pillars (e.g. 1 μm). There is less chance for $\boldsymbol{a_1}$ and $\boldsymbol{a_2}$ prismatic slips to block each other, and therefore weaker hardening effect which happened in larger pillars. When the α/β interfaces exist, they have the chance to interact with some of the dislocations during their escape to the surface. With the sample size decreasing (comparing Figure 6-8 (a) and Figure 6-15(c)), the possibility of dislocations interacting with the interface increased. As mentioned earlier, the interaction between dislocations and interfaces can lead to strengthening. Therefore, smaller sample size leads to the higher the work-hardening rate.

However, G3 in Figure 5-5 and G4 in Figure 5-7 shows the situation is different. The micro-pillars compressed along [0001] loading directions always show a constant work-hardening rate. Similar results can be found in literature about Ti-6Al-4V micro-cantilever bending tests [10], and again no words mentioned the work-hardening difference with that in $[1\bar{1}00]$ loading direction. Based on the TEM observation, the dislocations in G3 cannot escape the micro-pillars as easily as in G1 because of the dislocations forest when sample sizes decrease, and therefore there is an increase of work-hardening rates. In G4, there is almost no change of work-hardening rate with micro-pillar size. It may be the counteraction result of the strengthening of the dislocation interaction in the orientation and weakening from the β phase. The post-mortem TEM results are inadequate to reveal the interaction of the dislocations during the plastic deformation and further detailed studies are needed.

7.4 Strain bursts

The “strain burst” is the phenomenon that strain of micro-pillar increases suddenly during the plastic deformation. It is the reflection of a surface slip step was produced by large numbers of dislocations reached the micro-pillar side wall [80]. The more dislocations glide in the slip band, the larger strain burst it has. In this project, the micro-pillars were compressed in “displacement-control” mode which inhibits the strain change dramatically. However, this equivalent phenomenon still exists and it is displayed in another way as the “stress drop” in the stress-strain curves plotted. The surface step was produced to generate a strain burst which is faster than the set strain rate, while at the same time the micro-compression test machine keeps the set strain rate will generate an instant decrease of load and therefore the drop of stress. After the dislocations moved out of the micro-pillar, the micro-pillar changed into a relatively fewer defects condition. To accommodate the following plastic deformation, it requires higher stress to nucleate and move new dislocations [1, 56], and this causes a following stress increase after the strain burst. Therefore, the stress-strain curves usually show the serration of stress when strain burst to happen. Different strain bursts are shown in the different groups of micro-pillars. The three main differences are discussed below.

Firstly, the sample with smaller size expressed the larger strain burst in the stress-strain curves. Taking the stress-strain curves of G1 as an example, the smaller micro-pillar shows more obvious strain bursts. This is because, on the one hand, the dislocations can escape to the sample surface and cause a strain burst more easily in the smaller pillars than the larger ones. On the other hand, even the same size slip

step in the smaller micro-pillars are relatively larger and more obvious than in the larger sized micro-pillars.

Secondly, the orientation influences the number and magnitude of strain bursts. Comparing with G1, the stress-strain curves of G3 show much smaller strain bursts at an early stage of plastic deformation. At the same strain percentage, the <***c***+***a***> pyramidal slips activated in G3 have fewer slip bands move through the micro-pillars to their surface than the <***a***> prismatic slip activated in G1. On the one hand, the <***c***+***a***> dislocations in G3 were intertwined and hindered each other moving towards sample surface to generate a slip step and a strain burst in the stress-strain curve, which did not happen in G1. On the other hand, as the measured CRSS for micro-pillar of 3 um diameter in G1 is 724 MPa and for micro-pillar of 3 um diameter in G3 is 2114 MPa, the localized stress in G3 is much higher than G1. Because the number of slip bands produced in a crystal depends on the applied stress [115], dislocations move concentrating on one shear band in G3 instead of separating in several shear bands in G1. This also explained why there is a large strain burst strain in 3 μm micro-pillar but no strain burst in the 1 μm micro-pillars in Figure 5-5. As the 1 μm micro-pillars has higher strength, it required larger strain than the 3 μm micro-pillars to generate a higher local localized stress to shear the micro-pillar.

Thirdly, the α/β interface suppressed the strain burst happening. In the stress-strain curves in Figure 7-3, the stress-strain curves of single α micro-pillars or major β micro-pillars shown more serrations (at the first 2% strain after yielding) than the micro-pillars containing β fillet between two α. It is similar in the micro-pillars with

the [$1\bar{1}00$] orientation as well. The serration in the stress-strain curves of micro-pillars indicates dislocations activated and glided through these micro-pillars and produced strain bursts, but it is difficult to have such strain bursts in the micro-pillars containing a β fillet between two α. It was proved in the SEM images in Figure 5-6 and Figure 5-8 at same strain percentage, there are more observable slip traces on the side face of single α micro-pillars than micro-pillars containing a β fillet between two α. This phenomenon could be explained by the TEM samples analysis. As Figure 6-25 (a) shown, the α/β interface limited most of the dislocations within their own original phases because of no well-aligned slip systems on both sides of the α/β interface at the low strain (~2%). These limited dislocations cannot reach the free surface of the micro-pillars to generated a strain burst. When the flow stress is large enough to allow a slip band to penetrate both the interface and the dislocation forest through the whole micro-pillar, a large stress drop like the drop from 3000 MPa to 2250 MPa in the black curve in Figure 7-3 will appear. However, the dislocations in the micro-pillar without interface only need to penetrate the block of dislocation forest, and the micro-pillar without interface has no decreasing stress introduced by the β phase. Therefore, the green curves (micro-pillar with the interface) shows no stress drop at ~5% plastic strain compared with the black curve (micro-pillar without interface) in Figure 7-3.

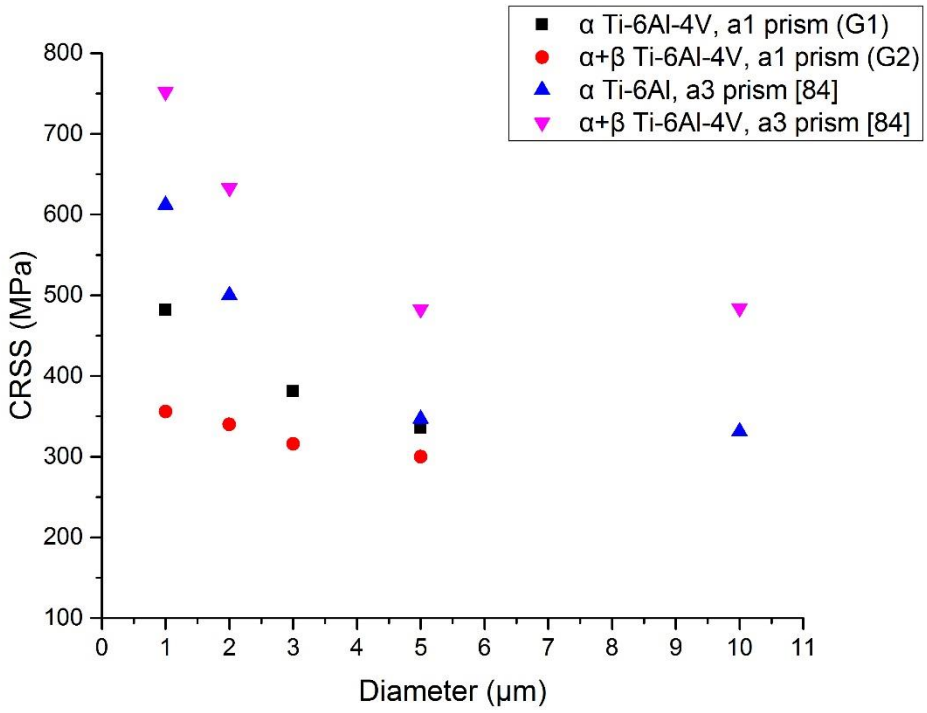

Figure 7-1 The CRSS values of G1/G2 and Ti-6Al/Ti-6Al-4V [84] in the micro-scale samples When the β phase and α/β interfaces are introduced into the sample, samples in G2 with $\boldsymbol{a_1}$ *dislocations show lower CRSS than samples in G1 with* $\boldsymbol{a_1}$ *dislocations. On the contrary, samples with* $\boldsymbol{a_3}$ *dislocations (α+β Ti-6Al-4V [84]) show higher CRSS than α Ti-6Al samples with* $\boldsymbol{a_3}$ *dislocations.*

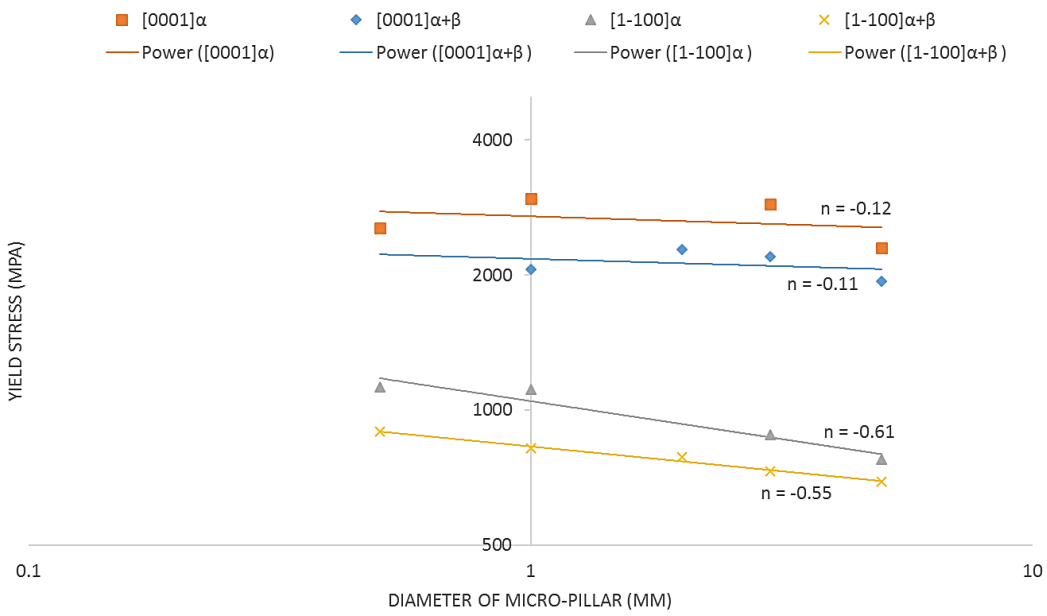

Figure 7-2 Log-log plot of yield stress vs. diameter (the line is the linear fit of calculated data) of the compressed micro-pillars different loading direction. Micro-pillars with [1$\bar{1}$00] loading direction show stronger sample size effect.

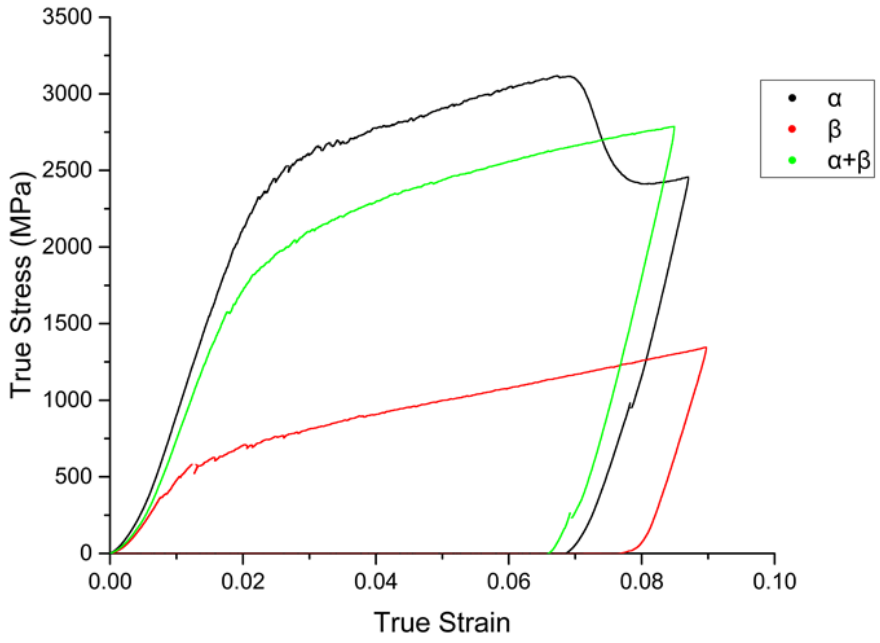

Figure 7-3 Stress-strain curves of the compressed 3 μm micro-pillars containing only α (black curve) and β fillet between two α phases (green curve) and β phase in the majority (red curve) compressed along [0001] // [101]. Their strength of micro-pillar is related to the volume fraction of β phase in them.

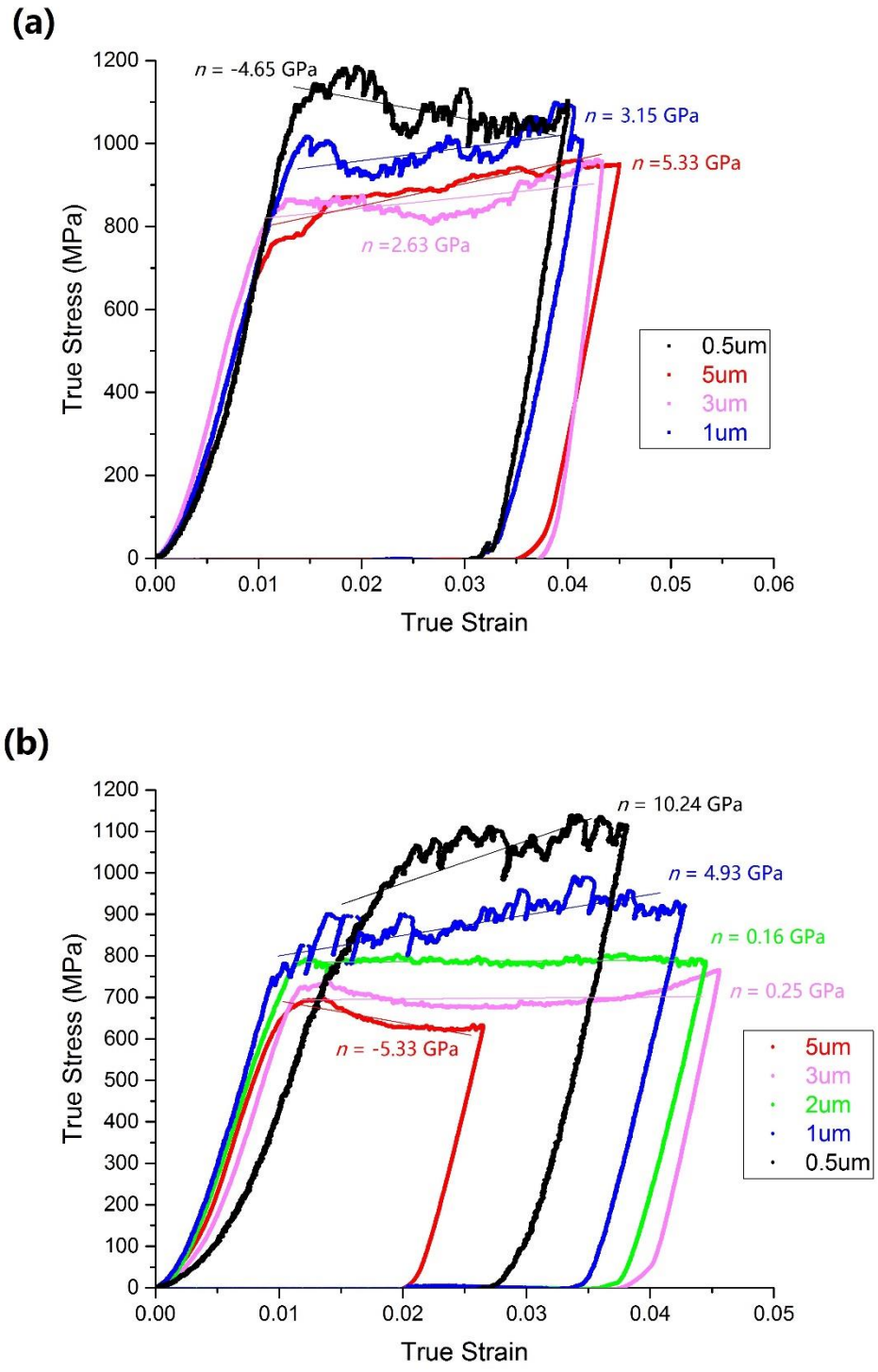

*Figure 7-4 The work hardening rate in different sizes of micro-pillars with **a** prismatic slip. (a) The α single phase micro-pillars. The work hardening rate decreased from 5.33 GPa to -4.65 GPa when micro-pillar diameters reduced from 5 μm to 0.5 μm. (b) The α/β micro-pillar. The work hardening rate increased from -5.33 GPa to 10.24 GPa when micro-pillar diameters reduced from 5 μm to 0.5 μm.*

Chapter 8 Conclusion and future work

8.1 Conclusions

Based on the micro-compression test and TEM analysis of the plastically deformed micro-pillars, the following conclusions can be drawn:

1. The β phase and the α/β interfaces within the micro-pillars are factors that have an influence on the strength of micro-scale samples. Because the β phase is weaker than the α phase and the α/β interfaces behaviour as both the barriers and sources of dislocations, the magnitude of influence depending on the volume fraction, orientation and morphology of the β phase and the α/β interfaces.
2. Both the single α phase and α/β two phases Ti-6Al-4V micro-pillars revealed size effect on strength. The orientation, volume fraction of β phase and the α/β interface have effects on the strength of micro-pillars and the scaling exponents of the sample size effect.
3. The work-hardening rate is related to the orientation of micro-pillars and the α/β interfaces in the micro-pillars.
4. The strain bursts can be suppressed by the α/β interface and smaller sample size. The sample with smaller size expressed the larger strain burst in the stress-strain curves. The orientation influences the number and magnitude of strain bursts.

8.2 Future work

Based on the limitations of the current work, suggestions for future work are summarized as follows.

- Although micro-pillars compressed to different strain level is helpful for understanding the dislocations movement in the micro-pillars, it is still difficult to observe the dislocations from the beginning of their generation. An in-situ TEM compression test may give more detailed and straightforward evidence of the α/β interface behaviour in the dislocation generation and transmission, especially for the <***c+a***> type slips which are complicated to be analyzed in the post-mortem TEM.
- A more accurate micro-pillar fabrication method should be applied to minimize the dimension difference between micro-pillars with the same conditions. For example, using lathe milling can reduce the taper angle of the side wall of micro-pillars or the unevenness of the top surface [116]. This is a method for getting accurate and comparable mechanical tests results, which means a more accurate analysis of the strength and then their sample size effect.
- Crystal plasticity modelling predictions of elastic-plastic response, slip activation, stress relaxation, and strain localization in the micro-pillars would be another path to validate the observation of the mechanical properties, the effect of β morphologies, the effect of orientations and the interfaces behaviours.

Appendix Lattice Invariant Line Calculation

Following Damen's method [34], the Burgers OR lattice correspondence is set to the coordinate (X, Y, Z) = ($[0001]_\alpha$// $[101]_\beta$, $[\bar{1}100]_\alpha$ // $[\bar{1}01]_\beta$, $[11\bar{2}0]_\alpha$ // $[001]_\beta$). Transformation matrix $\boldsymbol{A}$ is linear homogeneous transformation and can be decomposed into a rigid body rotation $\boldsymbol{R}$ through angle θ around X axis $[0001]_\alpha$ // $[110]_\beta$ and a pure deformation $\boldsymbol{D}$, in which a, b, c are relatively the X, Y, Z components of transformation strain. $\boldsymbol{u}$ is lattice invariant line.

In the new coordinate system, the pure deformation can be described as

$$\boldsymbol{D} = \begin{pmatrix} \frac{c_\alpha}{\sqrt{2}a_\beta} & 0 & 0 \\ 0 & \sqrt{\frac{3}{2}}\frac{a_\alpha}{a_\beta} & 0 \\ 0 & 0 & \frac{a_\alpha}{a_\beta} \end{pmatrix}$$

$$= \begin{pmatrix} a & 0 & 0 \\ 0 & b & 0 \\ 0 & 0 & c \end{pmatrix} \quad (1)$$

$\boldsymbol{A}$ can be described as

$$\boldsymbol{A} = \boldsymbol{RD} = \begin{pmatrix} 1 & 0 & 0 \\ 0 & cos\theta & sin\theta \\ 0 & -sin\theta & cos\theta \end{pmatrix}\begin{pmatrix} a & 0 & 0 \\ 0 & b & 0 \\ 0 & 0 & c \end{pmatrix} \quad (2)$$

$$= \begin{pmatrix} a & 0 & 0 \\ 0 & b\,cos\theta & c\,sin\theta \\ 0 & -b\,sin\theta & c\,cos\theta \end{pmatrix}$$

From the definition of lattice invariant line,

$$\boldsymbol{Au} = \boldsymbol{u} \quad (3)$$

$$\Rightarrow \boldsymbol{(A-1)u} = 0$$

$$\Rightarrow \Delta \begin{vmatrix} bcos\theta - 1 & csin\theta \\ -bsin\theta & ccos\theta - 1 \end{vmatrix} = 0$$

$$\Rightarrow cos\theta = \frac{1+bc}{b+c} \quad (4)$$

a_α = 0.2925 nm, c_α = 0.4670 nm, a_β = 0.319 nm for slowly furnance cooled Ti-6Al-4V [13]

$\Rightarrow \theta = 5.74°$ (5.78° for Ti-Cr alloy in literature [37])

Substituting the value of θ into equition (3)

$$\Rightarrow \boldsymbol{u} = \begin{matrix} 0 \\ -1.2806 \\ 1 \end{matrix}$$

Converting it to the vector in crystallographic coordinate of β phase,

$$\boldsymbol{u} = \begin{matrix} -1 \\ -1.2806\sqrt{2} \\ 1 \end{matrix} \approx [\bar{3}\bar{5}3]_{\beta} // [\bar{7}250]_{\alpha}$$

Reference

[1] J.R. Greer, W.C. Oliver, W.D. Nix, Size dependence of mechanical properties of gold at the micron scale in the absence of strain gradients, Acta Materialia 53(6) (2005) 1821-1830.

[2] Z.P. Bažant, Size effect, International Journal of Solids and Structures 37(1–2) (2000) 69-80.

[3] R. Maaß, S. Van Petegem, D. Ma, J. Zimmermann, D. Grolimund, F. Roters, H. Van Swygenhoven, D. Raabe, Smaller is stronger: The effect of strain hardening, Acta Materialia 57(20) (2009) 5996-6005.

[4] K.J. Hemker, W.N. Sharpe, Microscale Characterization of Mechanical Properties, Annual Review of Materials Research 37(1) (2007) 93-126.

[5] A. Pandey, In Situ Mechanical Testing in Electron Microscopes: Current Progress and Future Opportunities in Small-Scale Experimentation, JOM 67(8) (2015) 1682-1683.

[6] Z. Huichen, G. Yuzhou, Z. Rixue, Cavitation Erosion Characteristics of Titanium Alloy Thin Film Prepared by Ion Beam Enhanced Deposition, in: J. Luo, Y. Meng, T. Shao, Q. Zhao (Eds.), Advanced Tribology, Springer Berlin Heidelberg2010, pp. 536-539.

[7] M.D. Uchic, P.A. Shade, D.M. Dimiduk, Plasticity of Micrometer-Scale Single Crystals in Compression, Annual Review of Materials Research 39(1) (2009) 361-386.

[8] M.D. Uchic, D.M. Dimiduk, A methodology to investigate size scale effects in crystalline plasticity using uniaxial compression testing, Materials Science and Engineering: A 400–401(0) (2005) 268-278.

[9] M.F. Aimi, M.P. Rao, N.C. MacDonald, A.S. Zuruzi, D.P. Bothman, High-aspect-ratio bulk micromachining of titanium, Nat Mater 3(2) (2004) 103-5.

[10] R. Ding, J. Gong, A.J. Wilkinson, I.P. Jones, 〈c+a〉 Dislocations in deformed Ti－6Al－4V micro-cantilevers, Acta Materialia 76 (2014) 127-134.

[11] M.D. Uchic, D.M. Dimiduk, J.N. Florando, W.D. Nix, Sample Dimensions Influence Strength and Crystal Plasticity, Science 305(5686) (2004) 986-989.

[12] W.Y. Li, T. Ma, Y. Zhang, Q. Xu, J. Li, S. Yang, H. Liao, Microstructure Characterization and Mechanical Properties of Linear Friction Welded Ti-6Al-4V Alloy, Advanced Engineering Materials 10(1-2) (2008) 89-92.

[13] R. Boyer, G. Welsch, E.W. Collings, Materials properties handbook [electronic resource]: titanium alloys, ASM International, Materials Park, OH, 1994.

[14] M.F. Aimi, Bulk Titanium Microelectromechanical Systems, UNIVERSITY OF CALIFORNIA, 2005.

[15] V.A. Joshi, Titanium Alloys: An Atlas of Structures and Fracture Features, Taylor & Francis2006.

[16] G. Lütjering, J.J.C. Williams, Titanium, Springer London, Limited2007.

[17] G. Welsch, R. Boyer, E.W. Collings, Materials properties handbook: titanium alloys, ASM International1994.

[18] P. Wanjara, M. Jahazi, Linear friction welding of Ti-6Al-4V: Processing, microstructure, and mechanical-property inter-relationships, Metallurgical and Materials Transactions A 36(8) (2005) 2149-2164.

[19] W.D. Callister, D.G. Rethwisch, Materials Science and Engineering: An Introduction, Eigth Edition Binder Ready Version, John Wiley & Sons2010.

[20] A.S.M.I.H. Committee, ASM Handbook, Volume 04 - Heat Treating, ASM International, 1991.

[21] E. Lee, Microstructure evolution and microstructure/mechanical properties relationships in alpha+ beta titanium alloys, 2004.

[22] F. Bridier, P. Villechaise, J. Mendez, Analysis of the different slip systems activated by tension in a α/β titanium alloy in relation with local crystallographic orientation, Acta Materialia 53(3) (2005) 555-567.

[23] A. Lewis, S. Qidwai, A. Geltmacher, Slip Systems and Initiation of Plasticity in a Body-Centered-Cubic Titanium Alloy, MMTA 41(10) (2010) 2522-2531.

[24] I. Jones, W. Hutchinson, Stress-state dependence of slip in Titanium-6Al-4V and other HCP metals, Acta Metallurgica 29(6) (1981) 951-968.

[25] M.F. Savage, J. Tatalovich, M.J. Mills, Anisotropy in the room-temperature deformation of α–β colonies in titanium alloys: role of the α–β interface, Philosophical Magazine 84(11) (2004) 1127-1154.

[26] P.G. Partridge, The crystallography and deformation modes of hexagonal close-packed metals, Metallurgical Reviews 12(1) (1967) 169-194.

[27] H. Numakura, Y. Minonishi, M. Koiwa, 〈1123〉{1011} slip in titanium polycrystals at room temperature, Scripta Metallurgica 20(11) (1986) 1581-1586.

[28] M.H. Yoo, J.R. Morris, K.M. Ho, S.R. Agnew, Nonbasal deformation modes of HCP metals and alloys: Role of dislocation source and mobility, MMTA 33(3) (2002) 813-822.

[29] Q. Yu, J. Sun, J.W. Morris Jr, A.M. Minor, Source mechanism of non-basal 〈c + a〉 slip in Ti alloy, Scripta Materialia 69(1) (2013) 57-60.

[30] Y. Minonishi, S. Morozumi, H. Yoshinaga, {1122} <1123> slip in titanium, Scripta Metallurgica 16(4) (1982) 427-430.

[31] W. Burgers, On the process of transition of the cubic-body-centered modification into the hexagonal-close-packed modification of zirconium, Physica 1(7) (1934) 561-586.

[32] M. Mills, D. Hou, S. Suri, G. Viswanathan, Boundaries and interfaces in Materials, TMS, Warrendale, PA 295 (1998).

[33] T. Furuhara, T. Ogawa, T. Maki, Atomic structure of interphase boundary of an α precipitate plate in a β Ti-Cr alloy, Philosophical Magazine Letters 72(3) (1995) 175-183.

[34] U. Dahmen, Orientation relationships in precipitation systems, Acta Metallurgica 30(1) (1982) 63-73.

[35] T. Furuhara, S. Takagi, H. Watanabe, T. Maki, Crystallography of grain boundary α precipitates in a β titanium alloy, MMTA 27(6) (1996) 1635-1646.

[36] T. Furuhara, J.M. Howe, H.I. Aaronson, Interphase boundary structures of intragranular proeutectoid α plates in a hypoeutectoid Ti Cr alloy, Acta Metallurgica et Materialia 39(11) (1991) 2873-2886.

[37] T. Furuhara, H.I. Aaronson, Computer modeling of partially coherent B.C.C.:H.C.P. boundaries, Acta Metallurgica et Materialia 39(11) (1991) 2857-2872.

[38] U. Dahmen, The role of the invariant line in the search for an optimum interphase boundary by O-lattice theory, Scripta Metallurgica 15(1) (1981) 77-81.

[39] A.P. Sutton, R.W. Balluffi, Interfaces in crystalline materials, Clarendon Press1995.

[40] F.R.N. Nabarro, M.S. Duesbery, J.P. Hirth, Dislocations in solids, North-Holland Pub. Co., Amsterdam; New York, 1979.

[41] A. Romanov, T. Wagner, M. Rühle, Coherent to incoherent transition in mismatched interfaces, Scripta Materialia 38(6) (1998) 869-875.

[42] S. Zherebtsov, G. Salishchev, S. Lee Semiatin, Loss of coherency of the alpha/beta interface boundary in titanium alloys during deformation, Philosophical Magazine Letters 90(12) (2010) 903-914.

[43] R. Ding, J. Gong, A.J. Wilkinson, I.P. Jones, A study of dislocation transmission through a grain boundary in hcp Ti–6Al using micro-cantilevers, Acta Materialia 103 (2016) 416-423.

[44] J. Kacher, B.P. Eftink, B. Cui, I.M. Robertson, Dislocation interactions with grain boundaries, Current Opinion in Solid State and Materials Science 18(4) (2014) 227-243.

[45] Z. Zhang, T.-S. Jun, T.B. Britton, F.P. Dunne, Determination of Ti-6242 α and β slip properties using micro-pillar test and computational crystal plasticity, Journal of the Mechanics and Physics of Solids 95 (2016) 393-410.

[46] P.M. Anderson, J.P. Hirth, J. Lothe, Theory of Dislocations, Cambridge University Press2017.

[47] Z. Shen, R.H. Wagoner, W.A.T. Clark, Dislocation pile-up and grain boundary interactions in 304 stainless steel, Scripta Metallurgica 20(6) (1986) 921-926.

[48] A.A. Salem, S.L. Semiatin, Anisotropy of the hot plastic deformation of Ti–6Al–4V single-colony samples, Materials Science and Engineering: A 508(1–2) (2009) 114-120.

[49] M.F. Savage, J. Tatalovich, M. Zupan, K.J. Hemker, M.J. Mills, Deformation mechanisms and microtensile behavior of single colony Ti–6242Si, Materials Science and Engineering: A 319–321(0) (2001) 398-403.

[50] T. Neeraj †, M.F. Savage, J. Tatalovich, L. Kovarik, R.W. Hayes, M.J. Mills, Observation of tension–compression asymmetry in α and titanium alloys, Philosophical Magazine 85(2-3) (2005) 279-295.

[51] S. Suri, G.B. Viswanathan, T. Neeraj, D.H. Hou, M.J. Mills, Room temperature deformation and mechanisms of slip transmission in oriented single-colony crystals of an α/β titanium alloy, Acta Materialia 47(3) (1999) 1019-1034.

[52] R. Ding, J. Gong, A.J. Wilkinson, I.P. Jones, Transmission electron microscopy of deformed Ti–6Al–4 V micro-cantilevers, Philosophical Magazine 92(25-27) (2012) 3290-3314.

[53] R. Ding, Y. Chiu, I.P. Jones, N. Escalé, F. Pettinari-Sturmel, J. Douin, Application of a novel EBSD-FIB method to the transmission of c + a dislocations through α/β interfaces Ti–6Al–4V for producing in situ tension transmission electron microscopy specimens, Journal of Electron Microscopy 61(1) (2012) 31-36.

[54] A. Zhecheva, W. Sha, S. Malinov, A. Long, Enhancing the microstructure and properties of titanium alloys through nitriding and other surface engineering methods, Surface and Coatings Technology 200(7) (2005) 2192-2207.

[55] G. Venkatramani, S. Ghosh, M. Mills, A size-dependent crystal plasticity finite-element model for creep and load shedding in polycrystalline titanium alloys, Acta Materialia 55(11) (2007) 3971-3986.

[56] J.R. Greer, J.T.M. De Hosson, Plasticity in small-sized metallic systems: Intrinsic versus extrinsic size effect, Progress in Materials Science 56(6) (2011) 654-724.

[57] E.O. Hall, The Deformation and Ageing of Mild Steel: III Discussion of Results, Proceedings of the Physical Society. Section B 64(9) (1951) 747.

[58] N.J. Petch, The Cleavage Strength of Polycrystals, J. Iron Steel Inst. London 173 (1953) 25-28.

[59] P.M. Derlet, R. Maaß, Universal power-law strengthening in metals?, Scripta Materialia 109 (2015) 19-22.

[60] N. Hansen, Hall–Petch relation and boundary strengthening, Scripta Materialia 51(8) (2004) 801-806.

[61] R. Armstrong, I. Codd, R.M. Douthwaite, N.J. Petch, The plastic deformation of polycrystalline aggregates, Philosophical Magazine 7(73) (1962) 45-58.

[62] H. Van Swygenhoven, P.M. Derlet, Grain-boundary sliding in nanocrystalline fcc metals, Physical Review B 64(22) (2001) 224105.

[63] J. Gong, A.J. Wilkinson, Sample size effects on grain boundary sliding, Scripta Materialia 114 (2016) 17-20.

[64] W.D. Nix, H. Gao, Indentation size effects in crystalline materials: A law for strain gradient plasticity, Journal of the Mechanics and Physics of Solids 46(3) (1998) 411-425.

[65] H. Gao, Y. Huang, Geometrically necessary dislocation and size-dependent plasticity, Scripta Materialia 48(2) (2003) 113-118.

[66] E. Demir, D. Raabe, F. Roters, The mechanical size effect as a mean-field breakdown phenomenon: Example of microscale single crystal beam bending, Acta Materialia 58(5) (2010) 1876-1886.

[67] Y. Huang, F. Zhang, K. Hwang, W. Nix, G. Pharr, G. Feng, A model of size effects in nano-indentation, Journal of the Mechanics and Physics of Solids 54(8) (2006) 1668-1686.

[68] J.R. Greer, W.D. Nix, Nanoscale gold pillars strengthened through dislocation starvation, Physical Review B 73(24) (2006).

[69] W.D. Nix, J.R. Greer, G. Feng, E.T. Lilleodden, Deformation at the nanometer and micrometer length scales: Effects of strain gradients and dislocation starvation, Thin Solid Films 515(6) (2007) 3152-3157.

[70] T.A. Parthasarathy, S.I. Rao, D.M. Dimiduk, M.D. Uchic, D.R. Trinkle, Contribution to size effect of yield strength from the stochastics of dislocation source lengths in finite samples, Scripta Materialia 56(4) (2007) 313-316.

[71] S.I. Rao, D.M. Dimiduk, T.A. Parthasarathy, M.D. Uchic, M. Tang, C. Woodward, Athermal mechanisms of size-dependent crystal flow gleaned from three-dimensional discrete dislocation simulations, Acta Materialia 56(13) (2008) 3245-3259.

[72] S.-W. Lee, W.D. Nix, Size dependence of the yield strength of fcc and bcc metallic micropillars with diameters of a few micrometers, Philosophical Magazine 92(10) (2012) 1238-1260.

[73] D. Kiener, A.M. Minor, Source truncation and exhaustion: insights from quantitative in situ TEM tensile testing, Nano Lett 11(9) (2011) 3816-20.

[74] H. Gao, Y. Huang, W.D. Nix, J.W. Hutchinson, Mechanism-based strain gradient plasticity— I. Theory, Journal of the Mechanics and Physics of Solids 47(6) (1999) 1239-1263.

[75] Z.-J. Wang, Q.-J. Li, Z.-W. Shan, J. Li, J. Sun, E. Ma, Sample size effects on the large strain bursts in submicron aluminum pillars, Applied Physics Letters 100(7) (2012) 071906.

[76] D.M. Dimiduk, M.D. Uchic, T.A. Parthasarathy, Size-affected single-slip behavior of pure nickel microcrystals, Acta Materialia 53(15) (2005) 4065-4077.

[77] C.R. Weinberger, W. Cai, Surface-controlled dislocation multiplication in metal micropillars, Proc Natl Acad Sci U S A 105(38) (2008) 14304-7.

[78] J. Gil Sevillano, I. Ocaña Arizcorreta, L.P. Kubin, Intrinsic size effects in plasticity by dislocation glide, Materials Science and Engineering: A 309–310 (2001) 393-405.

[79] F.C. Frank, W.T. Read, Multiplication Processes for Slow Moving Dislocations, Physical Review 79(4) (1950) 722-723.

[80] D. Hull, D.J. Bacon, Introduction to Dislocations, Elsevier Science2001.

[81] G.I. Taylor, The Mechanism of Plastic Deformation of Crystals. Part I. Theoretical, Proceedings of the Royal Society of London A: Mathematical, Physical and Engineering Sciences 145(855) (1934) 362-387.

[82] T.B. Britton, F.P.E. Dunne, A.J. Wilkinson, On the mechanistic basis of deformation at the microscale in hexagonal close-packed metals, Proceedings of the Royal Society A: Mathematical, Physical and Engineering Science 471(2178) (2015) 20140881.

[83] D.J. Dunstan, A.J. Bushby, The scaling exponent in the size effect of small scale plastic deformation, International Journal of Plasticity 40 (2013) 152-162.

[84] J. Gong, A.J. Wilkinson, A microcantilever investigation of size effect, solid-solution strengthening and second-phase strengthening for 〈a〉 prism slip in alpha-Ti, Acta Materialia 59(15) (2011) 5970-5981.

[85] A. Kunz, S. Pathak, J.R. Greer, Size effects in Al nanopillars: Single crystalline vs. bicrystalline, Acta Materialia 59(11) (2011) 4416-4424.

[86] A.S. Schneider, C.P. Frick, B.G. Clark, P.A. Gruber, E. Arzt, Influence of orientation on the size effect in bcc pillars with different critical temperatures, Materials Science and Engineering: A 528(3) (2011) 1540-1547.

[87] H. Bei, S. Shim, E.P. George, M.K. Miller, E.G. Herbert, G.M. Pharr, Compressive strengths of molybdenum alloy micro-pillars prepared using a new technique, Scripta Materialia 57(5) (2007) 397-400.

[88] H. Bei, S. Shim, G.M. Pharr, E.P. George, Effects of pre-strain on the compressive stress–strain response of Mo-alloy single-crystal micropillars, Acta Materialia 56(17) (2008) 4762-4770.

[89] D. Kaufmann, R. Mönig, C.A. Volkert, O. Kraft, Size dependent mechanical behaviour of tantalum, International Journal of Plasticity 27(3) (2011) 470-478.

[90] X. Zhao, Fabrication and plastic deformation of copper at small scales, University of Birmingham, 2014.

[91] J. Gong, A.J. Wilkinson, Anisotropy in the plastic flow properties of single-crystal α titanium determined from micro-cantilever beams, Acta Materialia 57(19) (2009) 5693-5705.

[92] Q. Sun, Q. Guo, X. Yao, L. Xiao, J.R. Greer, J. Sun, Size effects in strength and plasticity of single-crystalline titanium micropillars with prismatic slip orientation, Scripta Materialia 65(6) (2011) 473-476.

[93] C.M. Byer, K.T. Ramesh, Effects of the initial dislocation density on size effects in single-crystal magnesium, Acta Materialia 61(10) (2013) 3808-3818.

[94] G.R. Huang, J.C. Huang, W.Y. Tsai, Origin of sample size effect: Stochastic dislocation formation in crystalline metals at small scales, Sci Rep 6 (2016) 39242.

[95] F.F. Csikor, C. Motz, D. Weygand, M. Zaiser, S. Zapperi, Dislocation avalanches, strain bursts, and the problem of plastic forming at the micrometer scale, Science 318(5848) (2007) 251-254.

[96] T.-S. Jun, G. Sernicola, F.P.E. Dunne, T.B. Britton, Local deformation mechanisms of two-phase Ti alloy, Materials Science and Engineering: A 649 (2016) 39-47.

[97] T.-S. Jun, Z. Zhang, G. Sernicola, F.P.E. Dunne, T.B. Britton, Local strain rate sensitivity of single α phase within a dual-phase Ti alloy, Acta Materialia 107 (2016) 298-309.

[98] J. Yang, J. Xu, G.-P. Zhang, Deformation and damage behavior of colonies in a small-sized α/β Ti alloy, Scripta Materialia 68(9) (2013) 715-718.

[99] G.S. Kim, Kim, Small volume investigation of slip and twinning in magnesium single crystals, Université de Grenoble, 2011.

[100] H. Zhang, B.E. Schuster, Q. Wei, K.T. Ramesh, The design of accurate micro-compression experiments, Scripta Materialia 54(2) (2006) 181-186.

[101] H. Fei, A. Abraham, N. Chawla, H. Jiang, Evaluation of Micro-Pillar Compression Tests for Accurate Determination of Elastic-Plastic Constitutive Relations, (2012).

[102] D. Tromans, Elastic anisotropy of HCP metal crystals and polycrystals, Int. J. Res. Rev. Appl. Sci 6(4) (2011) 462-483.

[103] G.B. Viswanathan, E. Lee, D.M. Maher, S. Banerjee, H.L. Fraser, Direct observations and analyses of dislocation substructures in the α phase of an α/β Ti-alloy formed by nanoindentation, Acta Materialia 53(19) (2005) 5101-5115.

[104] J.A. El-Awady, C. Woodward, D.M. Dimiduk, N.M. Ghoniem, Effects of focused ion beam induced damage on the plasticity of micropillars, Physical Review B 80(10) (2009) 104104.

[105] N.I. Kato, Reducing focused ion beam damage to transmission electron microscopy samples, Journal of Electron Microscopy 53(5) (2004) 451-458.

[106] J. Mayer, L.A. Giannuzzi, T. Kamino, J. Michael, TEM sample preparation and FIB-induced damage, Mrs Bulletin 32(05) (2007) 400-407.

[107] Y. Hai-Yan, Y. Guo-Hong, F. Wen-Liang, Size effect of the elastic modulus of rectangular nanobeams: Surface elasticity effect, Chinese Physics B 22(10) (2013) 106201.

[108] B. Hähnlein, P. Schaaf, J. Pezoldt, Size effect of Young's modulus in AlN thin layers, Journal of Applied Physics 116(12) (2014) 124306.

[109] Y. Zhu, Q. Qin, F. Xu, F. Fan, Y. Ding, T. Zhang, B.J. Wiley, Z.L. Wang, Size effects on elasticity, yielding, and fracture of silver nanowires: In situ experiments, Physical Review B 85(4) (2012) 045443.

[110] H. Liang, M. Upmanyu, H. Huang, Size-dependent elasticity of nanowires: Nonlinear effects, Physical Review B 71(24) (2005) 241403.

[111] M.T. Mohammed, Z.A. Khan, A.N. Siddiquee, Beta Titanium Alloys: The Lowest Elastic Modulus for Biomedical Applications: A Review.

[112] T. Butler, On the determination of dislocation densities, NAVAL ACADEMY ANNAPOLIS MD DEPT OF ENGINEERING, 1969.

[113] R.K. Ham, The determination of dislocation densities in thin films, Philosophical Magazine 6(69) (1961) 1183-1184.

[114] S.-W. Lee, S.M. Han, W.D. Nix, Uniaxial compression of fcc Au nanopillars on an MgO substrate: The effects of prestraining and annealing, Acta Materialia 57(15) (2009) 4404-4415.

[115] J.C. Fisher, E.W. Hart, R.H. Pry, Theory of Slip-Band Formation, Physical Review 87(6) (1952) 958-961.

[116] C.M. Byer, B. Li, B. Cao, K.T. Ramesh, Microcompression of single-crystal magnesium, Scripta Materialia 62(8) (2010) 536-539.